Scalable Surfaces for Electromagnetic Energy Harvesting and Wireless Power Transfer

by

Faruk Erkmen

A thesis
presented to the University of Waterloo
in fulfillment of the
thesis requirement for the degree of
Doctoral of Philosophy
in
Electrical and Computer Engineering

Waterloo, Ontario, Canada, 2019

Examining Committee Membership

The following served on the Examining Committee for this thesis. The decision of the Examining Committee is by majority vote.

External Examiner:	Tayeb A. Denidni Professor Centre Énergie Matériaux Télécommunications, Institut National de la Recherche Scientifique
Supervisor:	Omar M. Ramahi Professor Dept. of Electrical and Computer Engineering, University of Waterloo
Internal Member:	Karim S. Karim Professor, Associate Dean Outreach Dept. of Electrical and Computer Engineering, University of Waterloo
Internal Member:	Raafat R. Mansour Professor Dept. of Electrical and Computer Engineering, University of Waterloo
Internal-External Member:	Kevin Musselman Assistant Professor Dept. of Mechanical and Mechatronics Engineering, University of Waterloo

Author's Declaration

I hereby declare that I am the sole author of this thesis. This is a true copy of the thesis, including any required final revisions, as accepted by my examiners.

I understand that my thesis may be made electronically available to the public.

Abstract

The idea of collecting electromagnetic (EM) energy and converting it into various forms of useful power dates back to the early 20th century. Nikola Tesla's wireless power transfer experiments demonstrated the concept first, which was followed by researchers in Japan and the USA in subsequent decades. In terms of a working prototype, the first rectenna for efficient reception and rectification of microwave power was developed in the early 1960s. Later, the introduction of semiconductor diodes and the invention of Schottky diodes were significant developments towards the realization of practical rectennas. Since then, owing to the numerous applications in different technology domains (i.e. consumer electronics, renewable energy, transportation, internet of things, artificial intelligence, telecommunications, defense & space, biomedical engineering), wireless power transfer and EM energy harvesting have attracted significant interest.

Harvesting the ambient EM energy has emerged more recently as a promising application with potential for commercial success and contribution to a sustainable future with renewable energy. Many studies have reported the available ambient power densities measured in several parts of the world demonstrating the potentials and limitations of the concept. Traditional single rectenna structures have found very little use due to their inherent limitations at low power densities. Large rectenna arrays or periodic structures covering larger surface areas have become particularly important in order to efficiently harvest and convert the energy.

A rectenna consists of two main functional building blocks: the rectifier and the EM collector. The work in this thesis first focuses on improving these functional blocks individually. Regarding the rectifier function; a balanced full-wave rectifier is proposed where the circuit is differentially fed by two separate antennas. This configuration allows the received power to be rectified and transferred into a load between two antennas, making it convenient to channel the harvested power in rectenna arrays. The proposed concept is demonstrated using an array of T-matched dipole antennas at 2.45 GHz. It is also compared with half-wave rectennas that occupy the same footprint with an identical array layout. Measurement results show that, under the same circumstances, the proposed

full-wave rectification performs better than the traditional half-wave rectification and it is indeed suitable for energy harvesting rectenna arrays.

Regarding the EM collector; a novel Frequency Selective Surface (FSS) is developed as an absorber surface that accepts 98.5% of the available power and collects 97% of it exclusively on its resistive load (only 1.5% is dissipated as dielectric and metallic losses). To demonstrate its performance, a proof of concept FSS absorber is fabricated and its resistive load is replaced with a matched full-wave rectifier. Measurement results show that the overall Radiation-to-dc conversion efficiency of the complete rectenna system reaches 61%, which is considerably higher than the previously reported FSS based rectennas.

Subsequent sections in this thesis expand the energy harvesting surface by adding dual-band and dual-polarization capabilities. Design details and simulation results are provided together with measurement results. Fabricated prototypes are tested and their overall performance is evaluated based on the rectified dc power at the system load as percentage of the available EM power on the physical surface area of the rectenna (i.e. radiation-to-dc conversion efficiency).

A key contribution of this thesis is the introduction of the scalability concept for energy harvesting. The periodic absorber surfaces presented in this thesis have built-in channelling features that allow multi-cell configurations to feed a single rectifier. This is demonstrated to be an efficient means to increase the EM collector area per rectifier by effortlessly scaling the surface area while efficiently channelling the collected power. As a result, the number of diodes and diode losses are minimized in the system, leading to higher overall rectenna efficiencies. Real life ambient power densities can be on the order of $n\mathrm{W/cm}^2$ and the work in this thesis show that larger EM collectors can significantly mitigate the limitations posed by such low power levels. As an example; when integrated with a multi-cell configuration, an ordinary rectifier made with Schottky diodes was efficiently used at a power density that is less than $1/12^{th}$ of that would be required if the same rectifier were to be used with a traditional single unit cell approach.

Acknowledgments

First and foremost, I would like to express my sincere gratitude to Prof. Omar M. Ramahi for his excellent supervision. Prof. Ramahi genuinely cares about his students and I cannot thank him enough for his guidance, encouragement and support throughout this academic endeavor.

I would like to thank my committee members; Prof. Karim S. Karim, Prof. Rafaat R. Mansour, Prof. Kevin Musselman and Prof. Tayeb A. Denidni for reviewing my work and providing guidance.

I would like to thank the members of Prof. Ramahi's research group for productive debates and inspiring discussions. Among those, my special thanks go to Dr. Thamer Almoneef for his friendship and always uplifting spirit.

I would like to express my deepest gratitude to my dear wife Dr. Ayse Kuspinar for her unconditional love, support and wisdom throughout my graduate studies.

Table of Contents

List of Tables

List of Figures

Chapter 1

Introduction

1.1 Wireless Power Transfer and Electromagnetic Energy Harvesting

The idea of wireless power transfer dates back to Nikola Tesla's experiments in the early 20^{th} century [1]. Tesla built a large coil resonating at 150 kHz, and excited it with a 300 kW power source. Wireless power transferred from Tesla's coil reportedly turned on 200 light bulbs at a distance of 42 km [2]. Tesla's work was followed by researchers in Japan and the U.S.A. in subsequent decades [3, 4]. In 1963, Brown et. al. demonstrated the first complete and efficient wireless power transfer system by using high power microwave tubes [5]. A horn antenna was used to transmit 400 W microwave energy at 2.45 GHz. On the receiving end, also a horn antenna was used to collect the energy. Vacuum tube diodes were used to convert the collected energy into dc with 50% conversion efficiency [6]. The successful demonstrations of wireless power transfer encouraged Peter Glaser in 1968 to propose the Space Solar Power concept [7]. In his concept, Glaser proposed solar panels to be placed in the orbit of the earth, 22,300 miles above the equator, in order to harvest solar energy. The collected energy would be then converted into microwaves and transmitted to the earth using highly directive antennas as transmitters and receivers.

Brown's experiments in 1963 clearly showed that the efficiency of the wireless power transfer depends on the antenna gain and the rectification mechanism used in the receiving system. To advance his work further, Brown reportedly developed a receiver that reached 90.6% conversion efficiency in 1977. A dipole antenna with transmission lines made out of aluminum bars were used in this system. GaAs-Pt Schottky barrier diodes were used to rectify the received microwave power into dc [8]. Brown and Triner then developed a much lighter receiver using printed thin film technology in 1985, reportedly achieving 85% conversion efficiency [9]. Brown's work was pioneering in many aspects, however, he did not provide details in his publications on how the conversion efficiency was calculated.

The receiving system that consists of the rectifier and the antenna has been commonly referred to as the rectenna. Brown's rectennas were developed for sub 3 GHz frequencies. Arco Power Technologies developed 35 GHz and 94 GHz rectennas in 1991, and achieved 72% conversion efficiency [10]. The relatively high frequency of operation had advantages in terms of low atmospheric losses but also had disadvantages such as expensive and less efficient components [11]. In 1992, the first C-band rectenna array was developed by Bharj et. al. to operate at 5.87 GHz. The rectenna array comprised of 1000 dipoles together with custom-packaged Si Schottky diodes with a high reverse breakdown voltage and high power handling capability. The design achieved 80% RF-to-dc conversion efficiency [12].

Wireless power transfer inspired the idea of harvesting electromagnetic (EM) energy through the use of rectennas. The introduction of semiconductor diodes and the invention of Schottky diodes were significant developments towards the realization of low cost and practical energy harvesting systems [5, 8–10, 12, 13]. More recently, recycling the ambient RF energy has emerged as a promising application. Several recent studies investigated and reported the available RF power densities around the world [14–16]. These power levels clearly indicated the limitations of individual rectennas in terms of the amount of power they can collect. Antenna arrays, periodic structures and meta-surfaces covering larger areas have been proposed to overcome these limitations [17, 18].

1.2 Rectennas and Principles of Rectenna Design

The basic operation of EM energy harvesting relies on two key elements: the EM collector (i.e. receiving antenna), and the rectifier circuit. As illustrated in Fig.1.1, the antenna collects the available EM energy and converts it into RF power at its terminals. The RF power at the antenna terminals can also be conceived as high frequency ac power. The collected ac power is then fed into the rectifier to be converted to dc at the load. Since RF power is being transferred, impedance matching at the antenna-rectifier interface directly affects the harvesting efficiency.

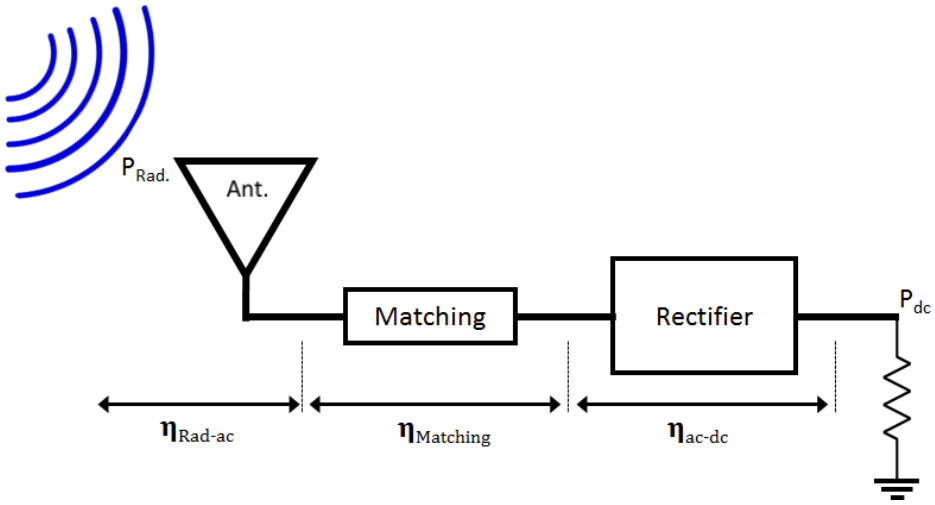

Figure 1.1: Simplified block diagram illustrating the operation of a rectenna.

Overall radiation-to-dc conversion efficiency of a rectenna can be expressed in terms of three sub-efficiencies as follows:

$$\eta_{Rad-dc} = \eta_{Rad-ac} \times \eta_{Matching} \times \eta_{ac-dc} \tag{1.1}$$

where η_{Rad-ac} represents the radiation-to-ac conversion efficiency and it indicates the percentage of the available radiated power that is captured by the receiving antenna, $\eta_{Matching}$ is the matching efficiency which indicates the percentage of the ac power that is delivered to the rectifier, η_{ac-dc} represents the ac-to-dc conversion efficiency and it indicates the percentage of the available input RF power of the rectifier that is converted to dc power at the load. Maximizing the overall efficiency is only possible by individually optimizing all three sub-efficiencies of the system given in Eqn. (1.1). It should be noted that in some cases, the matching efficiency can be included in the efficiency of the antenna or the rectifier depending on the rectenna construction.

1.3 Rectifier Topologies Used in Rectennas

Rectifier topologies can be grouped into two main categories depending on their configurations; half-wave rectifiers and full-wave rectifiers. The half-wave rectifier is the simplest and the most common configuration [19–25]. In its basic form, a half-wave rectifier needs a diode, a load resistor, and a storage element to smoothen the output voltage or current. The storage element can be either a capacitor in shunt or an inductor in series with the load. Diode configuration can be a single-series mounted diode or a single-shunt mounted diode. A half-wave rectifier is a simple and low-cost construction which requires very few components. Its main limitation is the fact that it can utilize only one half-cycle of the ac signal. It requires proper storage elements and filtering mechanisms to smoothen the output current or voltage. Half-wave rectifiers are also generally more suited for lower power applications [26, 27].

A full-wave rectifier, on the other hand, can take advantage of both half cycles of the ac signal, which can lead to improved efficiencies [27]. The main drawback of the full-wave rectification is that it requires two diodes to be turned on compared to only one in the case

of half-wave rectification. As a result, it is more prone to diode losses and traditionally more suitable for higher power applications. There are very few examples of full-wave rectifiers in RF or microwave literature despite their common use in power electronics [28–31]. Some of the reported examples focused on the matching and conversion efficiency of the full-wave rectifier but did not report the overall performance of the rectenna as an integrated system [28, 30, 31]. Others evaluated the performance of single full-wave rectennas but did not comment on the applicability of their concepts to rectenna arrays where combining the rectified dc current from array elements can be challenging [29].

Real life ambient power densities are reported to be on the order of $n\mathrm{W/cm^2}$ which indicates the limitations of individual rectennas in terms of the amount of power they can collect [15, 16]. Therefore, converting the ambient RF energy into practical dc power can only be possible by using large EM collectors such as rectenna arrays, periodic structures or metasurfaces [14, 27]. In terms of the rectification mechanisms, most of the reported rectenna arrays used half-wave rectification. Some designs enhanced the half-wave rectification by using voltage doubler circuits and stacked differential structures in order to increase the dc output voltage [32, 33]. Only a few examples implemented full-wave rectification in rectenna arrays with very limited details provided on the rectenna efficiency as an integrated system [12].

1.4 EM Collectors Used in Rectennas

1.4.1 Antennas

Several traditional antenna types have been proposed to be used in EM energy harvesting rectennas; dipoles, bow-ties, patches, loops, rings, vivaldis, and spiral antennas can be given as examples [23, 24, 32, 34–38]. Some of these antennas were only compatible with linearly polarized incoming waves, and they were subject to polarization losses with circularly polarized incident waves. These limitations have been addressed by studies that reported circularly polarized antennas for energy harvesting [32, 36, 39]. Operational bandwidth has

been another common limitation of rectennas, especially when they were optimized for a specific target frequency. Several bandwidth enhancement techniques have been proposed to overcome these issues and to obtain wide band performance [40–42].

In addition to single rectennas that consist of one antenna and one rectifier, more recently, there has been an increased focus on rectenna arrays in the context of ambient RF energy harvesting [19,33,43,44]. One important challenge for rectenna arrays has been the effective channelling of the collected power. There are mainly two approaches to combine the collected power from antenna elements; RF combiner approach, and dc combiner approach [45]. In the RF combiner approach, a feed network of matched transmission lines connect the antenna elements to a single feed point. The power from multiple antennas is collected at this reference point and is delivered to the rectifier to be converted to dc. The main advantage of the RF combiner approach is the relatively large RF power accumulated at the rectifier input terminal which results in a high RF-to-dc conversion efficiency. The disadvantage of this approach is the need for a complex feed network, which is usually not scalable and lossy due to dielectric substrate properties. On the other hand, the dc combiner approach integrates each antenna element with a rectifier, and combines the rectified dc current at the system load via dc bus traces. This approach eliminates the RF losses at the transmission lines but it requires each antenna element to collect enough power to operate the rectifier at a reasonable efficiency. Therefore, the dc combiner approach is more suitable for high power applications [45].

1.4.2 Meta-surfaces and Periodic Structures

In addition to antenna arrays, metamaterials and periodic structures have been recently proposed for energy harvesting purposes due to their excellent absorption characteristics [46–48]. Previous studies have demonstrated several features of metamaterials such as polarization independence, wide operating bandwidth, and ultra low profile [47, 49–54]. However, in most of the previously reported work, lossy dielectric substrate was an essential part of the design where the absorbed power was mainly dissipated in the dielectric [47, 55]. In order for metamaterials to be used in energy harvesting, the absorbed power

needs to be delivered to a load, or a rectifier. Lumped resistors have been employed in periodic structures before but they weren't used as a system load; the main focus has been maximizing the absorption and the bandwidth even if the absorbed power was dissipated in dielectric losses [56–60]. More recently, near unity absorption at lumped resistors has been achieved by metasurfaces [17, 18]. However, these designs only demonstrated how the EM energy was captured by the periodic surface; they did not study how the captured energy can be efficiently transferred to a rectifier. The conceivable next step for the earlier designs is to replace the resistors and employ rectifiers in each unit cell. Given the size of the unit cells and available ambient RF power densities, the collected power would be very low, resulting in very low conversion efficiencies in the rectifiers [14–16, 61, 62]. Furthermore, a dc combiner circuit would be needed to collect the power from each unit cell, adding further losses [45].

Only very recently, Frequency Selective Surfaces (FSSs) have been used for energy harvesting, and have been integrated with rectifiers [63, 64]. However, these designs also implemented rectifiers in every unit cell which meant a considerable part of the collected power was dissipated at the diodes. Hence, the overall efficiencies of previous works could not exceed 50% [63, 64].

1.5 Research Problem and Thesis Outline

The efficiency of a rectenna is predominantly determined by the radiation-to-ac conversion efficiency of its EM collector (i.e. receiving antenna), and the ac-to-dc conversion efficiency of its rectifier, assuming matching is included in one of these sub-efficiencies. In the case of rectenna arrays, channelling the collected power to a single load also introduces efficiency constraints. The work presented in this thesis provides contributions to improve the overall performance of rectenna systems, particularly in the context of EM energy harvesting applications. The thesis first focuses on improving the rectification efficiency of rectenna arrays through the use of full-wave rectification. Then, the EM collection is studied in detail and periodic absorber surfaces are proposed to address several common limitations

of the existing rectenna structures. The chapters of the thesis are organized as follows:

Chapter 1 provides an introduction to wireless power transfer and EM energy harvesting by reviewing the major milestones and the relevant literature. Rectenna building blocks are discussed; an overview of the traditional implementations for rectifiers and EM collectors are provided. This chapter also provides the motivation and the research objectives of the thesis.

Chapter 2 investigates the current rectification topologies used in rectennas and provides a thorough review of the advantages and disadvantages of full-wave rectification compared to half-wave rectification. This chapter also provides an overview of rectenna arrays and their suitability for ambient RF energy harvesting at low power applications since they can collect energy from larger areas than single rectennas. A novel full-wave rectification mechanism is then proposed as a solution specifically tailored for rectenna arrays that potentially addresses an important limitation of the current array implementations without compromising the efficiency.

Chapter 3 presents a brief overview of FSSs in the context of EM energy harvesting and proposes a novel absorber surface that achieves near unity absorption on its resistive load. Theoretical framework is provided for the proposed FSS unit cell that explains the absorption mechanism in the form of an equivalent transmission line circuit model. This chapter also presents the design and construction of a full-wave rectifier that is matched to the impedance of the FSS based absorber surface. The integrated rectenna is then fabricated as a proof-of concept for experimental verifications. Measurements agree with the simulations proving the viability of the proposed concept. This chapter also discusses the scalability of the proposed concept with its potentials and limitations.

Chapter 4 builds on the proposed periodic absorber surface in Chapter 3 and presents a dual-band EM energy harvesting surface that is designed for absorbing the EM energy in the GSM-1800 and Wi-Fi bands. The unit cell of the periodic structure incorporates two bow-tie dipoles and a resistive load demonstrating excellent absorption characteristics with minimal dielectric losses. The unit cell geometry also incorporates channelling traces making it possible to combine multiple cells together and increase the collected power per

load. The dual-band absorber integrated with a full-wave rectifier is fabricated as a complete rectenna prototype. Measurements results agree with simulations and demonstrate the feasibility of the concept.

Chapter 5 presents a dual-polarized EM energy harvesting system that consists of a periodic absorber surface and a full-wave rectifier. The unit cell of the absorber is constructed using concentric bow-tie dipoles and channelling features making it possible to efficiently combine and transfer the collected power from multiple unit cells. Simulation results are provided together with experimental verification demonstrating the excellent absorption characteristics of the proposed energy harvesting surface. The efficiency of the structure was evaluated in various polarization angles and the results demonstrate that the proposed concept can be used to construct a scalable and polarization insensitive energy harvesting system.

Chapter 6 provides the main conclusions and contributions of this work. This chapter also provides discussions and recommendations for future work.

Chapter 2

Electromagnetic Energy Harvesting Using Full-wave Rectification

2.1 Introduction

This chapter focuses on developing a rectenna array that utilizes full-wave rectification to maximize ac to dc power conversion efficiency, and ultimately the efficiency of the overall energy harvesting system. A new concept is proposed where a full-wave rectifier circuit is differentially fed by two separate antennas. This structure allows the received power to be rectified and transferred to a dc load between two antennas. The concept is first designed and fabricated in a rectenna array that consists of T-matched dipole antennas and the proposed full-wave rectifiers. Experimental results are provided for the radiation-to-dc conversion efficiency of the fabricated rectenna. The proposed full-wave rectenna panel is then compared to half-wave rectenna panels operating at the same frequency and occupying the same physical footprint. Finally, the dc channelling feature of the proposed topology is demonstrated in an array of full-wave rectennas where the harvested dc power is channeled into a single resistive load for the entire panel.

2.2 Theory of Operation

Rectennas can be implemented using single or multiple diodes together with matching circuits and filters [26]. In its most simple form, a rectifier needs a diode, a load resistor and a storage element to smoothen the output voltage or current. The storage element can be either a capacitor in shunt or an inductor in series with the load.

A half-wave rectifier is a simple and low cost construction which requires very few components. Its main limitation is the fact that it can utilize only one half cycle of the ac signal. On the other hand, full-wave rectifiers can take advantage of both half cycles of the ac signal which can lead to improved efficiencies. However, full-wave rectification requires two diodes to be turned on compared to only one in the case of half-wave rectification. The proposed full-wave rectenna concept is illustrated using the schematic shown in Fig.2.1 where a full-wave bridge is implemented between two dipole antennas. Diode pairs are connected to the antenna terminals and a resistive load is connected between them. Here, dipole antennas are chosen for simplicity but the concept can be applied to other types of antennas. The ends of the dipoles are tied together through ac isolating inductors to provide a dc path.

When EM radiation is received by the antennas, ac voltage is generated across their terminals with a sinusoidal waveform. The generated voltage depends on the antenna parameters as well as the properties of the incident wave such as frequency, polarization and angle of incidence. Antenna parameters such as radiation efficiency and directivity determine how well the antenna captures the EM radiation and generates the ac voltage at its terminals. The impedance matching between the antenna and the rectifier determines how much of the generated ac power can be transferred to the rectifier and how much will be reflected. The rectifier's RF-to-dc conversion efficiency determines how much of the input power can be converted to dc power at its load. The antennas in Fig.2.1 can be modeled as dependent ac sources and the proposed full-wave rectenna system becomes equivalent to a bridge rectifier connected to two dependent ac sources on both sides as shown in Fig.2.2. During the positive half cycle, diodes $D2$ and $D3$ would turn on with inductor $L2$ providing the dc current return path. Similarly, during the negative half cycle,

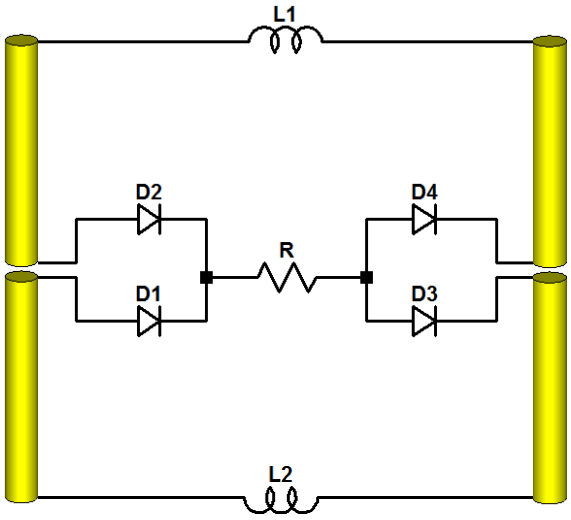

Figure 2.1: Schematic illustrating the concept of full-wave rectification using two identical dipole antennas. The distance between the two antennas is electrically small and not shown to scale.

diodes $D1$ and $D4$ would turn on with inductor $L1$ providing the dc current return path. The inductors $L1$ and $L2$ act as dc short and RF open between the two antennas thus completing the closed circuit for dc operation while isolating the antennas from each other for RF operation. $L1$ and $L2$ also serve as smoothing filters to minimize the ripples of the rectified dc current. The working principle of the proposed configuration is very similar to the traditional full-wave bridge rectifier. The main difference is that the proposed rectenna utilizes two separate antennas differentially feeding the full-wave rectifier, which allows the received RF power by the antennas to be rectified and transferred to a dc load between the antennas. This feature can be utilized for alternative dc channelling schemes in planar and stacked rectenna arrays. If the two antennas were replaced with a single antenna, V1 and V2 in Fig.2.2 would merge to become one dependent ac voltage source and the whole configuration would become a traditional full-wave rectenna.

For ideal full-wave rectification, $V1$ and $V2$, the dependent ac voltages replacing the antennas in the equivalent model, should be identical to each other. However, this condition

is only possible if identical antennas are exposed to the same incident wave properties. If the incoming wave has an off-normal angle with respect to the plane of the two antennas, there would be a phase difference between the generated voltage sources due to the distance between the two antennas even if the antennas were identical. In such cases, the phase difference can be minimized by maintaining an electrically small distance between the antennas. Moreover, if the antennas were not identical, the generated voltages could be different in both amplitude and phase. At any given time, the generated voltages can turn on only two of the diodes while the other two are in reverse bias. The full-wave rectification mechanism is possible as long as there is enough potential difference to turn on the two diodes during both half cycles. Overall, the power conversion efficiency can be expected to degrade for off normal incidence or for non identical antenna configurations.

2.3 Full-wave Rectenna Design

The rectifier and antenna are the two primary functional blocks of a rectenna system. These two blocks are generally designed separately and integrated through a matching network. In this chapter, the rectenna is conceived as an integral system and thus the rectification circuitry was not only matched to the antenna (as if they were two isolated stages) to ensure optimal power transfer but the dc channelling was also integrated as part of the entire system rather than only a receiving stage. Schottky diodes from Avago HSMS-286x family were used because of their low turn on voltage and high detection sensitivity [65]. Dual diodes in SOT-23 packages of HSMS-2863 and HSMS-2864 were chosen for ease of fabrication. For the inductor selection, the inductance and the self resonant frequency (SRF) were the two main selection criteria. High inductance value is desired for better smoothing function, and better RF isolation between the antennas. High SRF is also desired to avoid parasitic effects of the inductor package. However, the inductance is inversely proportional with the SRF and these two criteria narrows down the inductor selection. Murata's 0603 size LQW18AN47NG00D was chosen for having 47 nH inductance, 0.29 Ω dc resistance, and 2.6 GHz SRF [66] (47 nH was the highest inductance available in the high quality factor LQW series that has an SRF higher than the intended

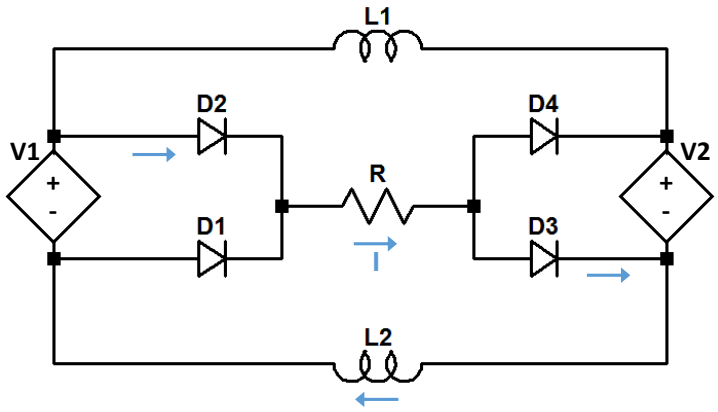

(a)

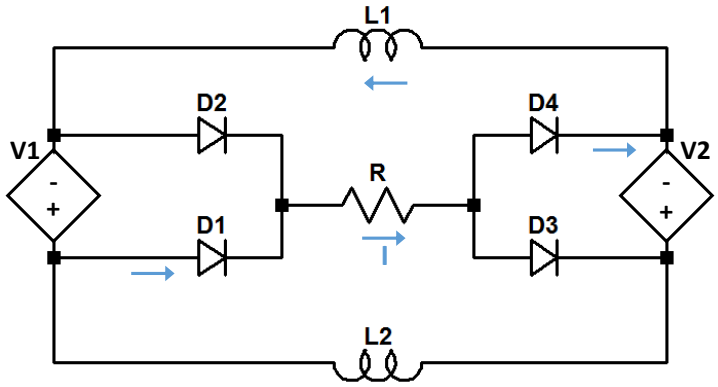

(b)

Figure 2.2: Equivalent schematic of the proposed full wave rectenna showing the direction of dc current. (a) During the positive half cycle. (b) During the negative half cycle.

operating frequency of 2.45 GHz). As explained in Fig.2.2, the proposed full-wave rectenna concept requires the two antennas to be connected to each other through inductors at each end. Using a single inductor would require physical traces to be connected to the antennas affecting their radiated performance. To avoid this effect, the connection was achieved using two inductors at the antenna ends and a PCB trace between them. Inductors have

high impedance at the frequency of operation and act as an open circuit. Hence, both antennas were essentially disconnected from the PCB trace and from each other during the RF operation, making it possible to design and optimize their antenna characteristics individually.

The full-wave rectifier was built on Rogers RO4003 board and its input impedance was measured using an Agilent E-5071C Vector Network Analyzer. The impedance behavior is dependent on the rectifier load and input power. Therefore, the rectifier impedance was characterized over a range of input power and load resistance by adjusting the VNA port power settings and the load resistance. The impedance curve at 5 dBm input power and 1 kΩ load resistance was determined to be most suitable to be matched by the antenna impedance, and was selected to be used for antenna optimization. This selections was revisited later where the radiated measurement results are discussed.

Rectenna designs often require a matching circuit because in most cases the antennas and rectifiers are optimized separately and most antennas cannot be matched to the rectifier impedance easily [29]. In this work, the T-matched dipole antenna was adopted since it provides excellent control over its input impedance by optimization of its dimensions [67–70].

The full-wave rectenna array was designed using CST MICROWAVE STUDIO (CST MWS) [71]. The dipole antenna dimensions and the spacing between array elements were optimized to maximize the received power from an incident plane wave with linear polarization and with a normal angle of incidence to the array panel. It should be noted that the implementation of the full-wave rectifier did not affect the spacing between antennas, and did not increase the optimum size of the rectenna structure. The distance between array elements was mainly determined by the mutual coupling effects between antennas. The T-sections of the dipoles were optimized through parametric simulations in order to achieve the desired impedance characteristics that conjugate matches the measured rectifier input impedance. Fig.2.3 shows the optimized antenna dimensions. This approach minimized the mismatch losses while eliminating the need for a matching network.

The rectenna array was fabricated on a Rogers RO4003 substrate with 1.52 mm thick-

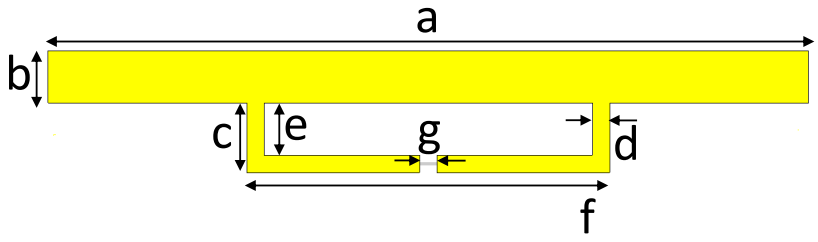

Figure 2.3: Optimized antenna dimensions of the T-matched dipole for full-wave rectification at 2.45 GHz (all in mm): a=44, b=3, c=4, d=1, e=3, f=21, g=1.

ness and 35 μm copper cladding as shown in Fig. 2.4. The full-wave rectifier was implemented between each antenna pair. In the array configuration, the vertical and horizontal spacing between the antenna elements (see Fig. 2.4) were 20 mm and 5 mm, respectively. The antenna terminals were connected to the rectifier leads through plated vias. The central antenna pair and the load in between was used for the measurements.

In order to verify the conjugate match condition, the input impedance of the central antenna was measured using the differential probe method with a custom built calibration kit. For balanced antennas, such as dipoles, impedance measurements require special techniques where equal and opposite feed currents are needed from the test equipment [72,73]. There are several techniques that can be used to avoid this issue but the differential probe method was found most suitable for this work due to its practicality [72–75]. This technique places the calibration reference plane directly at the measured port which eliminates the need for post-processing such as de-embedding or conversion calculations [76,77]. The custom built calibration kit was fabricated on Rogers RO4003 substrate as shown in Fig. 2.5 (a). The substrate thickness was 1.524 mm. The calibration kit included Open, Short, 50 Ω Load and Through. Traces in the calibration kit were kept very short and designed as short co-planar waveguides without ground plane. Two 100 Ω resistors were used to achieve a differential 50 Ω matched load, and negligible impedance jumpers were used to achieve short termination. Keysight E5071C was used as the Vector Network Analyzer (i.e. VNA). Two ports of the VNA were combined to compose a logical differential port. Hirose

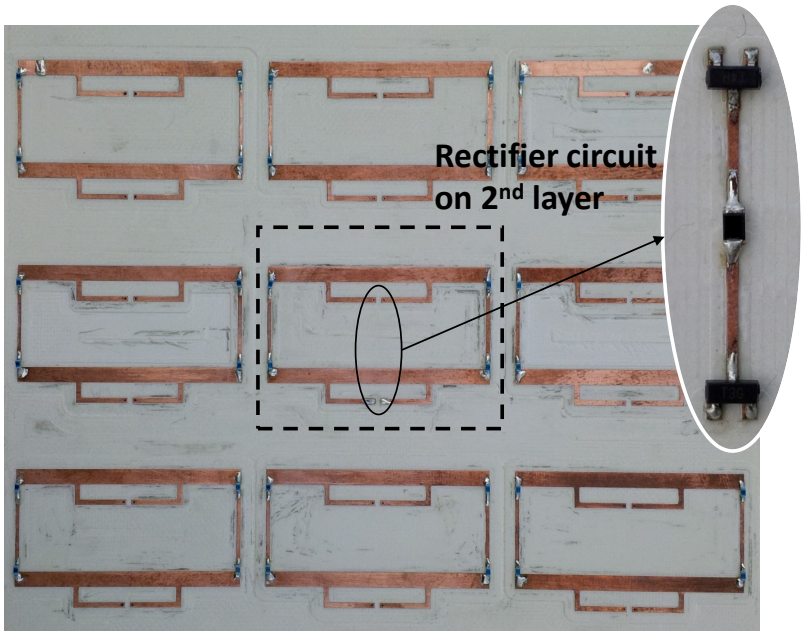

Figure 2.4: Fabricated panel of full-wave rectenna array (FWR-Panel). The rectifier circuit placed at the bottom layer is shown in the inset.

W.FL series miniature coaxial cables were used as extension to regular semi-rigid coaxial cables. W.FL series offer very low profile mated height, small footprint, and extreme light weight which makes it an ideal choice for delicate antenna measurements [78]. Fig. 2.5 (b) and Fig. 2.5 (c) show the final differential probe used for the impedance measurements. The input impedance of the central antenna was measured using the differential port setup as illustrated in Fig.2.5 (d). Measured antenna impedance together with the full-wave rectifier input impedance are presented in Fig.2.6. Measured impedances and the return loss between the antenna and the rectifier are tabulated in Table 2.1. As can be seen, very good matching was obtained around 2.45 GHz.

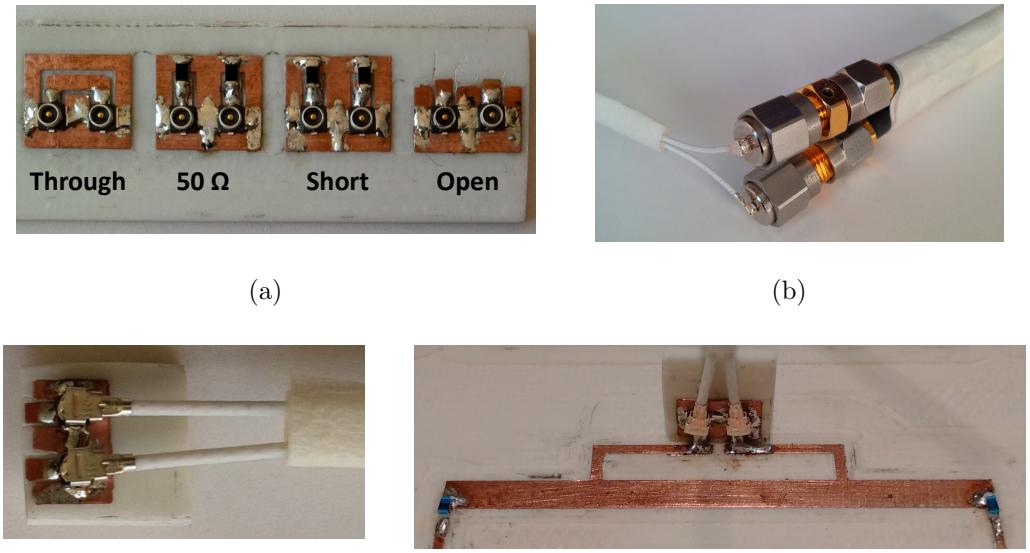

(a) (b)

(c) (d)

Figure 2.5: Differential input impedance measurement setup (a) Custom calibration kit (b) W.FL to SMA adaptor (c) Calibrated reference plane of the logical differential port (d) Input impedance measurement of the T-matched dipole antenna.

2.4 Radiated Measurements

The rectenna performance was evaluated using the radiation-to-dc power conversion efficiency η_{Rad-dc} defined as:

$$\eta_{Rad-dc} = \frac{P_{dc,col.}}{P_{Rad.,av.}} \tag{2.1}$$

where $P_{dc,col.}$ is the dc power collected at the load, and $P_{Rad.,av.}$ is the total incident radiated power available at the physical area of the antenna [29, 36, 79]. η_{Rad-dc} can be written as

$$\eta_{Rad-dc} = \eta_{Rad-ac} \times \eta_{Matching} \times \eta_{ac-dc} \tag{2.2}$$

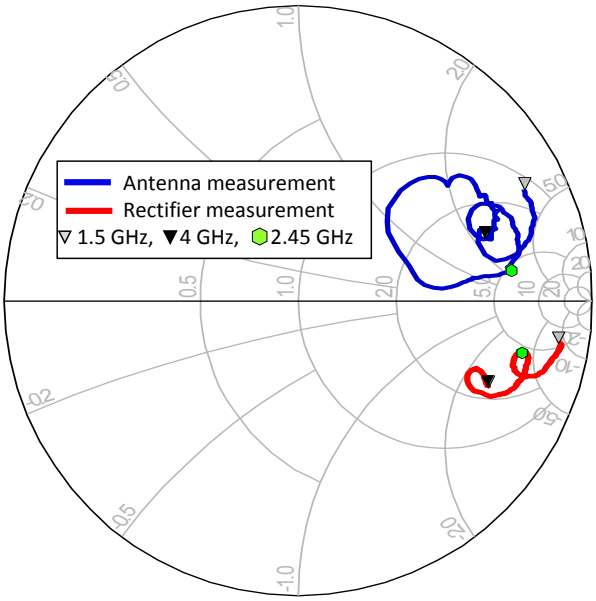

Figure 2.6: Measured impedance plots of the full wave rectifier and the antenna. Frequency range is 1.5 GHz to 4 GHz. Good conjugate match is obtained without a matching network.

where η_{Rad-ac} is the radiation-to-ac conversion efficiency representing the effectiveness of the antennas to capture EM radiation and η_{ac-dc} represents the conversion efficiency of the rectification circuitry. $\eta_{Matching}$ is the matching efficiency which indicates the percentage of the ac power that is delivered to the rectifier.

The efficiency of the full-wave rectenna was evaluated in an array implementation rather than a single stand-alone structure because antennas perform differently when positioned in close proximity to adjacent antennas. Mutual coupling between them plays a significant role in determining the individual antenna parameters [79–81]. This effect was taken into account by using an array configuration and evaluating the dc power converted through a single central element. Measured results represent the per-unit-cell performance of the array. A good estimate of the total dc power collected by the array is the product of the dc power collected by the central element and the number of cells in the array, assuming

Table 2.1: Impedance matching of the full-wave rectenna.

Freq. (GHz)	Measured Rectifier Impedance	Measured Antenna Impedance	Return Loss (dB)
2.0	$166 - j314$	$151 + j202$	9.5 dB
2.1	$143 - j264$	$172 + j247$	19.4 dB
2.2	$144 - j213$	$223 + j281$	11.1 dB
2.3	$182 - j180$	$315 + j285$	9.6 dB
2.4	$224 - j193$	$363 + j181$	12.5 dB
2.5	$217 - j225$	$333 + j105$	10.6 dB
2.6	$187 - j228$	$259 + j48$	7.9 dB
2.7	$158 - j219$	$140 + j54$	6.2 dB
2.8	$134 - j202$	$99 + j137$	10.4 dB
2.9	$118 - j185$	$111 + j185$	36.4 dB
3.0	$108 - j163$	$138 + j207$	13.5 dB

an efficient dc channelling mechanism. Of course, the larger the array, the more accurate this estimate becomes.

The radiated measurement setup is illustrated in Fig. 2.7. A photograph of the measurements setup inside an anechoic chamber is shown in Fig. 2.8. A signal generator was used as the source. Output of the signal generator was amplified and fed into a standard gain horn antenna in such a way that the electric field of the incident wave was parallel to the dipole arms. The full-wave rectenna panel was placed 1 m away from the horn antenna. Considering the design frequency of 2.45 GHz and the largest antenna dimension of 44 mm, the Fraunhofer distance was calculated as 0.032 m and the measurement distance of 1 m satisfied the far field conditions. Measurements were carried out with varying load resistance, incident power, and frequency. The rectified dc voltage across the load was recorded using a digital multimeter and the collected dc power, $P_{dc,col.}$ was calculated for all test cases.

Physically measuring the received power at the antenna terminals was not feasible be-

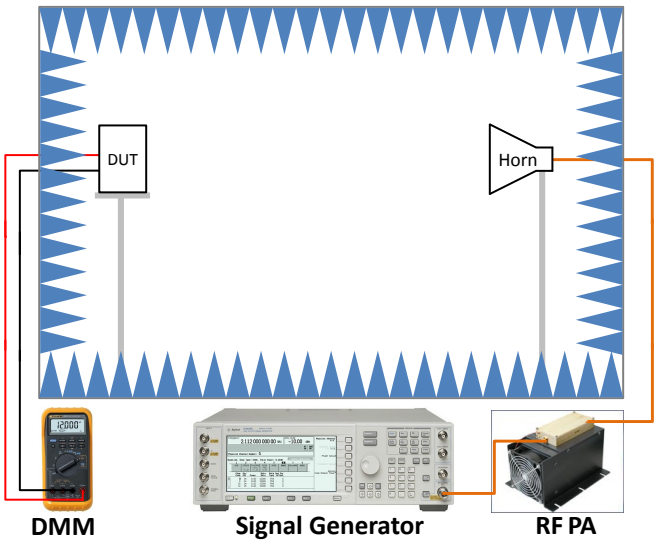

Figure 2.7: Schematic showing the measurement setup for the radiation-to-dc conversion efficiency.

cause this would require the antenna to be matched to the test equipment's 50 Ω port and that would contradict one of the key objectives of the proposed concept in this chapter: to eliminate the matching network by directly matching the antenna to the rectifier. Therefore, to obtain the efficiency in (2.1), the available incident power $P_{Rad.,av.}$ was determined by applying the link budget calculations [29]:

$$P_{Rad.,av.} = S_{Rad.,av.}\ A_p \tag{2.3}$$

$$S_{Rad.,av.} = EIRP\ \frac{1}{4\pi d^2} \tag{2.4}$$

$$EIRP = P_s - L_c + G_a + G_h \tag{2.5}$$

where $EIRP$ is the effective isotropic radiated power of the transmitter, $L_{fs} = 1/4\pi d^2$ is the distance dependency, or the free space path loss of the EM energy expressed with

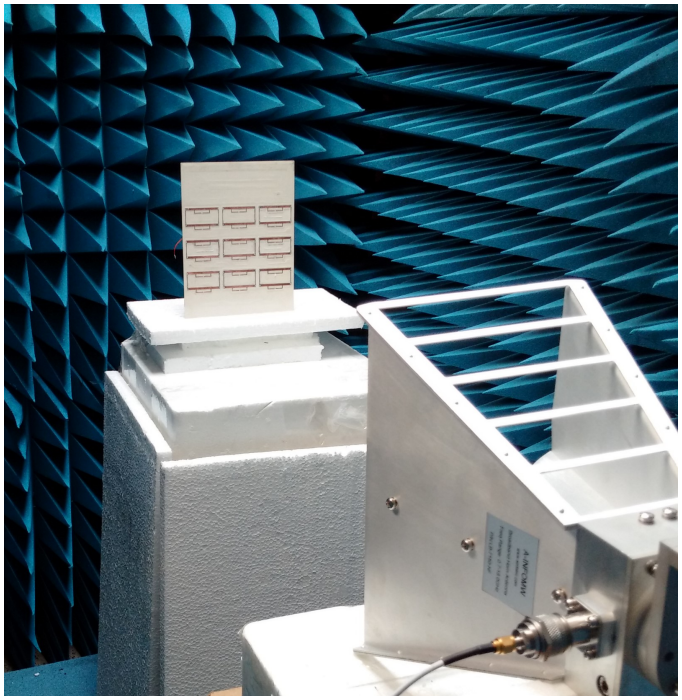

Figure 2.8: Measurement setup inside an anechoic chamber.

inverse square law. The source power P_s was known from the signal generator. The losses of the coaxial cables were measured using the VNA. The amplifier gain G_a was measured with a power-meter and the horn antenna gain G_h was obtained from its datasheet. The source power and the frequency were varied during the measurements to find the peak efficiency. The transmitter horn antenna gain was also frequency dependent. Table 2.2 provides the definitions of the link budget parameters and their values at 2.45 GHz.

Fig. 2.9 (a) shows the rectenna efficiency versus load resistance. The peak occured at 1 kΩ load which is consistent with the rectifier design provided above. A full-wave rectifier with load resistance 1 kΩ was taken as a reference while the antenna was optimized to match this impedance.

Fig. 2.9 (b) shows the rectenna efficiency versus incident power. The peak occured when the incident power density $S_{Rad.,av.}$ was 0.23 mW/cm^2. By multiplying this value with the rectenna physical area A_p used for the efficiency calculation, the available power

Table 2.2: Link budget parameters at 2.45 GHz.

Transmitter Parameters	
Frequency (f)	2.45 GHz
Source output power (P_s)	0 dBm
Measured cable loss (L_c)	1.8 dB
Amplifier gain (G_a)	37.8 dB
Tx antenna (i.e. Horn) gain at 2.45 GHz (G_h)	9.4 dB
EIRP (P_s-L_c+G_a+G_h)	45.4 dBm
Propagation Parameters	
Distance (d)	1 m
Free space path loss (L_{fs})	11 dB
RF power density at panel surface ($S_{Rad.,av.}$)	34.4 dBm/m^2
RF power density at panel surface ($S_{Rad.,av.}$)	0.2754 mW/cm^2
Panel Parameters	
Rectenna physical area (A_p)	19.6 cm^2

for the rectenna can be obtained as $P_{Rad.,av} = 4.5$ mW (6.5 dBm). This was also consistent with the rectifier design because the reference impedance used for the antenna optimization was obtained by measuring the full-wave rectifier with 5 dBm input power.

Fig. 2.9 (c) shows the rectenna efficiency versus frequency while keeping the load resistance and the incident power at their optimum values. A peak radiation-to-dc conversion efficiency of 74% was recorded at 2.55 GHz. Considering the rectenna array was originally optimized for 2.45 GHz with good impedance matching with the rectifier, the frequency dependency of the rectenna efficiency was found to be in good agreement with design objectives. The T-matched dipoles were found to be highly sensitive to fabrication tolerances and even small deviations in the trace widths could be responsible for the frequency shift observed in Fig. 2.9 (c).

It should be noted that the measured 74% efficiency is different and more comprehensive than the widely reported RF-to-dc conversion efficiencies in literature [30, 32, 35, 38, 82, 83].

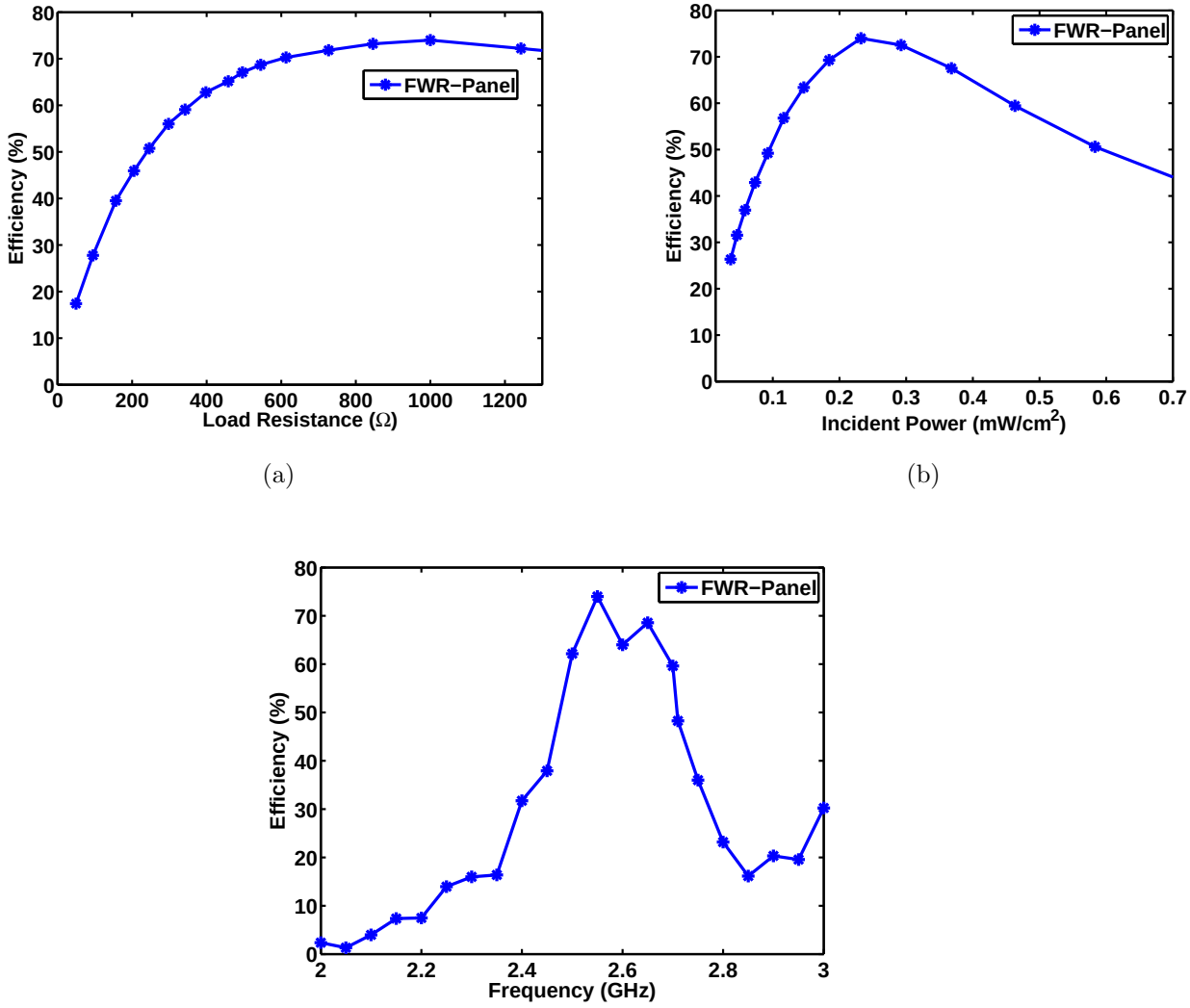

(a)

(b)

(c)

Figure 2.9: The measured radiation-to-dc conversion efficiency η_{Rad-dc} of the full-wave rectenna system. (a) As a function of the load resistance. (b) As a function of the incident power. (c) As a function of the frequency.

The RF-to-dc conversion efficiency is a measure of the rectifier circuit alone, where the RF power is fed into the rectifier terminal (generally via an SMA connection) and the rectified dc power is measured at the output load resistor. The rectenna presented in this chapter, however, was designed as a whole system that integrates a matched antenna integrated with a novel rectifier circuit. The system was then measured for the radiation-to-dc conversion efficiency which includes receiving the incident EM radiation, transferring the captured power to the rectifier, and converting it into dc power at the load. Radiation-to-dc conversion efficiency is a metric for the rectenna as a system, indicating the percentage of the available EM power (radiated) on a given surface area that can be collected and converted into dc power at the system load. Unlike the RF-to-dc conversion efficiency, radiation-to-dc conversion efficiency takes the antenna performance and the physical area into account when determining the overall performance.

Efficiencies involving the physical areas of rectennas have been previously reported. For instance, 53% efficiency with an array of split ring resonators was reported in [37], while, in [84], a near-unity efficiency was reported employing a ground plane backed metasurface. However, both of these studies measured the collected power in terms of time average power (ac) and they did not include rectifiers. In [44], a large rectenna array was presented but its overall efficiency was measured using the transmitted power instead of available power on the array surface. In [19], [33] and [85], similar radiation-to-dc conversion efficiency definitions were used reporting 38%, 38% and 44.1% overall efficiencies for power densities as low as $33\mu W/cm^2$, $0.030W/m^2$ and $0.041W/m^2$, respectively.

2.5 Comparison with Half-wave Rectennas

Although the experimental results demonstrated that the new rectenna topology is highly efficient, it is imperative to compare it with the half-wave rectenna array to demonstrate the value added by the additional complexity involved with the full-wave rectification. Therefore, for meaningful comparison, two panels of rectenna arrays were designed using a simple half-wave rectifier circuit which includes a diode, a load resistor and an inductor,

all in series. The same components from the full-wave rectification design were used. The first panel was designed to reflect the traditional $\lambda/2$ spacing between the antenna elements (HWR-Panel1), and the second was identical to the full-wave rectenna array in terms of distances between the antenna elements (HWR-Panel2). Both rectenna arrays used T-matched dipole antennas. Only the T-sections were optimized for each panel keeping the main antenna length and width constant for a fair comparison.

Following the design steps described above, the half-wave rectifier was built on Rogers RO4003 board and its input impedance was measured. T-matched dipole antennas were then optimized to match the rectifier impedance. Both panels were fabricated on Rogers RO4003 boards. Fig. 2.10 (a) shows the HWR-Panel1 and Fig. 2.10 (b) shows the HWR-Panel2. Excellent matching was obtained with return loss greater than 10 dB for both panels over the frequency range of interest.

The half-wave rectenna panels were tested following the steps described above. The optimum load resistance for each panel was determined where peak efficiency was recorded. Using these values, both panels were tested with respect to incident power and frequency. Voltage readings were recorded from the central rectennas and the efficiencies were calculated using the physical areas shown with dashed lines in Fig. 2.10 which represent unit cells.

Measured efficiencies of the half-wave rectennas compared to the previously measured full-wave rectenna are provided in Fig.2.11. Several observations can be made based on these results. HWR-Panel1 and HWR-Panel2 have identical half-wave rectifiers and essentially the same antenna elements, but HWR-Panel2 demonstrates much higher efficiency. Since the main difference is the panel layout, this efficiency improvement can be attributed to the denser array configuration in HWR-Panel2. This is expected because the rectenna in HWR-Panel1 has twice the physical footprint but harvests only 22% more power. This comparison experimentally verifies that utilizing denser arrays can increase the rectenna efficiency significantly. Comparing HWR-Panel2 and FWR-Panel, it should be noted that the array layouts were identical and both structures used essentially the same antenna elements. The HWR-Panel2 array used half-wave rectifier while the FWR-Panel array

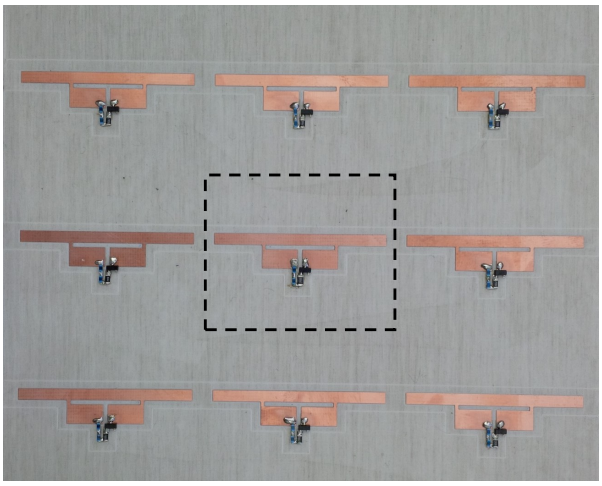

(a)

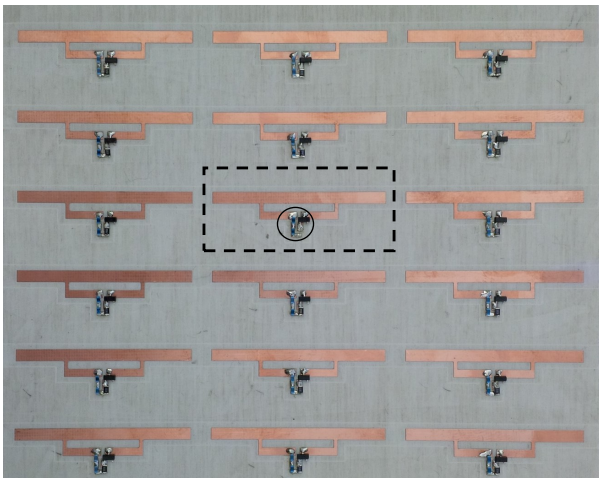

(b)

Figure 2.10: The fabricated half-wave rectenna panels with the designated unit cell area shown using dashed lines. (a) HWR-Panel1: 3x3 layout with $\lambda/2$ spacing. (b) HWR-Panel2: 3x6 layout similar to full-wave rectenna panel in FWR-Panel.

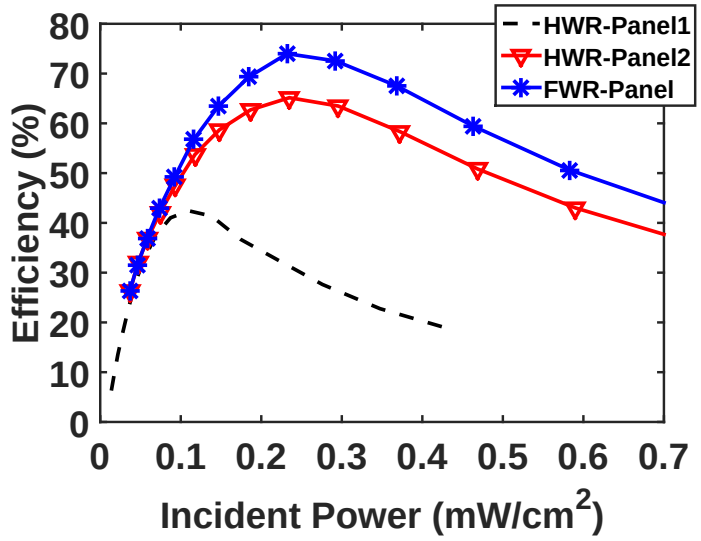

(a)

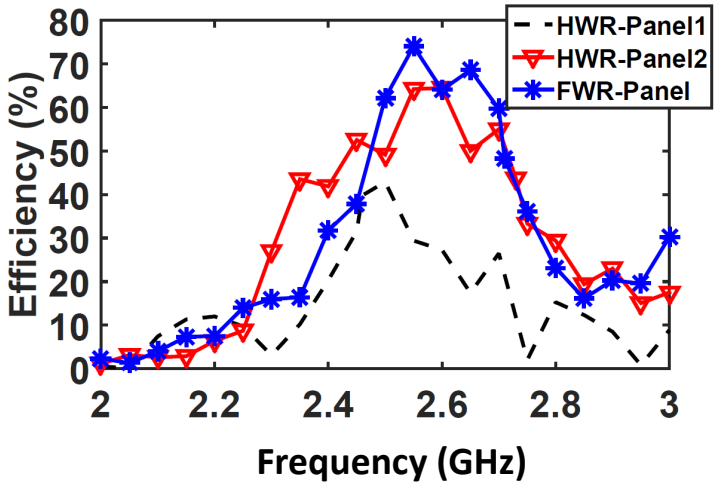

(b)

Figure 2.11: The measured radiation-to-dc conversion efficiency, η_{Rad-dc} of the fabricated rectennas. (a) As a function of the incident power. (b) As a function of frequency.

used the proposed full-wave rectifier. The measurements shown in Fig. 2.11 verify that the full-wave rectification indeed performs better than the half-wave rectification with an increase in the peak η_{Rad-dc} of more than 10%.

As a limitation, the rectennas in this chapter generally required higher power densities than the reported available ambient levels to reach their peak efficiencies [15]. However, there are still many applications where the power densities are well within the measured levels in this chapter. Outdoor locations closer to mobile network towers or indoor locations closer to Wi-Fi routers can be given as examples.

2.6 Channelling the DC Power in Full-wave Rectenna Array

All the measurements so far were performed at the central element of the arrays to obtain a unit cell characteristics. In this section, a full-wave rectenna array was designed and fabricated to to demonstrate the ease of dc channelling with the proposed rectenna topology. Similar to the FWR-Panel and HWR-Panel2, 18 T-matched dipole elements were used in a 3x6 configuration. Instead of using a load resistor for every rectifier, the dc current was channelled to flow through a single load for the entire panel. A two-layer RO4003 substrate was used for fabrication where the rectifier circuits and the dc channelling traces were routed at the bottom layer while the antennas were at the top layer directly facing the incoming radiation. Fig. 2.12 shows the fabricated full-wave rectenna array.

As shown in Fig. 2.13, radiated measurements showed that peak η_{Rad-dc} of 52% was obtained at 66 Ω load resistance and 0.14 mW/cm^2 incident power at the panel surface. The total panel area used for efficiency calculations was 170.4 cm^2 which encompasses all of the 18 rectennas.

The panel in Fig. 2.12 demonstrates the actual array implementation of the proposed rectenna. The antenna dimensions were optimized for the unit cell, which is fairly accurate for the central antennas but not for the ones on the periphery of the panel. Thus, for the

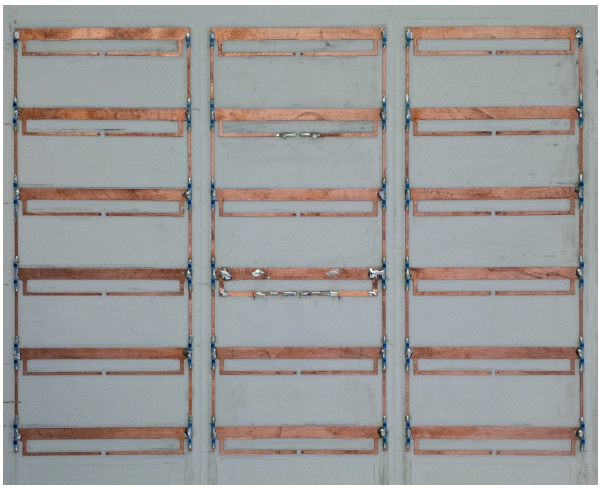

(a)

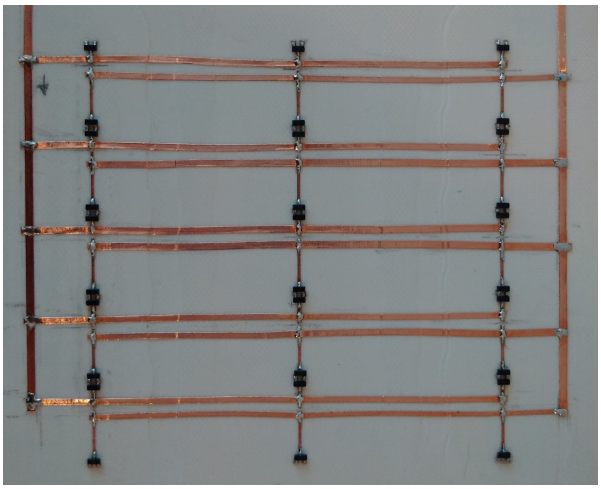

(b)

Figure 2.12: Full-wave rectenna array where all the harvested dc power is collected to a single load. (a) Top surface showing the antennas (directly facing the incoming radiation). (b) Bottom surface showing the rectifiers and the dc channelling traces.

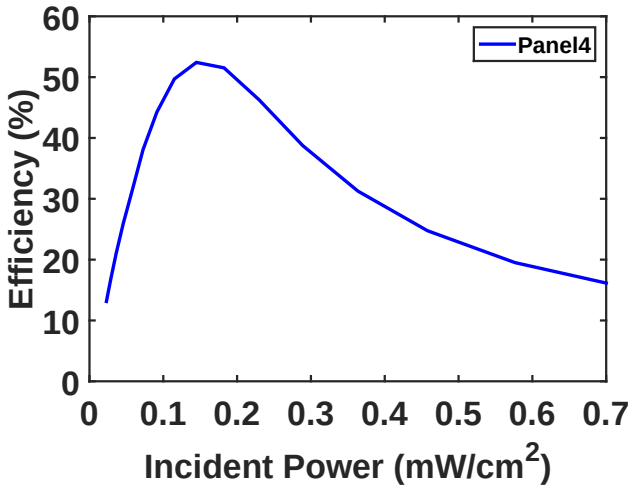

(a)

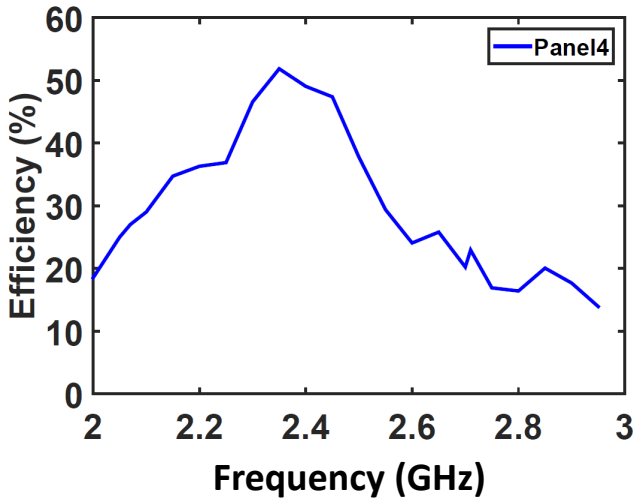

(b)

Figure 2.13: The measured radiation-to-dc conversion efficiency (η_{Rad-dc}) of the full-wave rectenna array with dc power channelled to a single load. (a) As a function of the incident power. (b) As a function of the frequency.

peripheral rectennas, larger mismatch losses would be expected between the antennas and the rectifiers. This is the main reason for the efficiency of the panel to be lower than the previously measured unit cell rectenna. The rectified dc power from each rectenna element was combined in parallel, which resulted in a relatively low load resistance of 66 Ω. For practical applications, the load impedance of the rectenna array can be treated as a design parameter and can be optimized to match a desired value. This can be achieved by either a series or parallel combination of the dc current, or by optimizing the individual rectenna parameters.

2.7 Conclusion

A novel EM radiation to dc power conversion system is proposed realizing full-wave rectification. This balanced configuration allows the received power to be rectified and transferred to a dc load between two antennas. The concept is demonstrated at 2.45 GHz by using T-matched dipole antennas. The rectifier was built first, and the antenna dimensions were optimized to match the measured rectifier impedance, eliminating the need for a matching network.

Radiated measurements showed that the proposed full-wave rectenna achieved 74% radiation-to-dc conversion efficiency, which was higher than similarly constructed half-wave rectennas. In addition to its high efficiency, the proposed topology allowed the rectified dc current to flow from one antenna to another through a resistive load. This feature was utilized in a rectenna array to demonstrate the ease of dc channelling to a single load.

Chapter 3

Scalable Electromagnetic Energy Harvesting Using Frequency Selective Surfaces

3.1 Introduction

Periodic structures and electromagnetic (EM) absorbers have been widely used in various applications such as radar cross section reductions, EM compatibility (EMC) / EM interference (EMI) suppression and anechoic chamber design [56, 86, 87]. The common goal across all the applications is to absorb the incident EM waves and minimize the reflections. Salisbury screens were the first radar absorber design with resistive sheets placed a quarter wavelength above a ground plane [88]. Later, Jaumann absorbers were introduced expanding the absorption bandwidth using dielectrics and additional resistive sheets [89]. In subsequent years, other materials such as ferrite tiles, lossy dielectrics, pyramidal absorbers and carbon nano-tubes have been used in absorber designs [90–94]. Introduction of frequency selective surfaces (FSSs) and circuit analog absorbers (CAAs) made it possible to produce complex impedance surfaces through the use of periodic structures, which resulted in enhanced bandwidth and lower profile absorbers [86, 95–97]. CAAs consist

of specially designed periodic structures backed by a conductive surface. They can be modeled as transmission lines seen by the incident plane wave [17, 57, 58, 98, 99]. The CAAs use patterned periodic structures that can be modeled with lumped elements such as resistors, capacitors and inductors. The lumped elements are defined in relation to the physical structure and the conductive ground plane is modeled as a short termination of the transmission line [89, 100, 101].

Absorbing the incident EM wave is the first step to a successful rectenna operation. In this regard, CAAs have very much in common with EM energy harvesting systems. However, energy harvesting also requires the absorbed energy to be transferred to a rectifier and converted into dc at the resistive load. Most of the previously published FSS works focused on the absorption characteristics only [56–58]. Dielectric losses were reported to be the key factor in absorbing and dissipating the energy in most cases [17, 102, 103]. Since power absorbed in the dielectric cannot be transferred to the rectifier, such FSS designs are not suitable for energy harvesting. Even though some designs used lumped resistors in periodic structures, the main focus has always been the absorption characteristics and bandwidth enhancement [56–58]. More recently, near unity absorption at lumped resistors has been achieved by metasurfaces [17, 18]. However, these designs only demonstrated how the EM energy was captured by the periodic surface; they did not study how the captured energy can be efficiently transferred to a rectifier. The conceivable next step for the earlier designs is to replace the resistors and employ rectifiers in each unit cell. However, given the size of the unit cells and available ambient RF power densities, the collected power would be very low, resulting in very low conversion efficiencies in the rectifiers [14–16, 61, 62]. Furthermore, a dc combiner circuit is needed to collect the power from each unit cell, adding further losses [45]. Antenna arrays have been used for wireless power transfer (WPT) applications before but these were not periodic absorbing surfaces; they were designed for retrodirective antenna solutions with improved bandwidth and scanning capabilities [104, 105].

Only very recently, FSSs have been used for energy harvesting, and have been integrated with rectifiers [63, 64]. However, these designs also implemented rectifiers in every unit cell which meant a considerable part of the collected power was dissipated at the diodes. Hence,

the overall efficiency of the previous work was 25% and 50% at -6 dBm and -10 dBm input power to the rectifiers, respectively [63,64]. In this chapter, an FSS based design is utilized to address the channelling problem and to increase the overall rectenna efficiency. First, the design of a planar and low profile absorber surface is presented based on the principles of FSSs. The surface consists of periodic structures with built-in channelling features. Then a full-wave bridge rectifier is designed and integrated to the absorber surface with an input impedance matched to the load required by the FSS. Eliminating the matching network in WPT systems has been demonstrated before by directly matching the rectifier to the antenna [27,106]. Overall efficiency of the structure reaches 61% which was obtained at 15 dBm input power at the rectifier. However, it should be noted that relatively high input power of the rectifier is remedied by combining multiple unit cells of the FSS structure, resulting in a viable solution for RF energy harvesting in very low ambient power densities. Simulation results are validated by experimental data, demonstrating the highly efficient radiation-to-dc conversion characteristics of the overall structure. The chapter is concluded by discussing the results and limitations of the proposed absorber surface.

3.2 Absorber FSS Design

EM fields in uniform regions and waveguides have been modeled using uniform transmission lines [100]. These models provide very useful physical insight while offering clues to designing better and simpler FSS geometries [89]. For EM energy harvesting, the goal in this chapter was to design a planar FSS that collects almost all of the available energy and channels it to a resistive load. Therefore, traditional FSS design steps are used but the structure is further optimized for this specific goal. Although FSSs can be modeled as various configurations, a series RLC network was shown to be the best topology in terms of absorption and bandwidth, thus, this network topology was adopted in this chapter [101].

In transmission line models, metallic strips perpendicular to the E-field of the incident plane wave were modeled as capacitance, whereas metallic strips parallel to the E-field of the incident plane wave have been modeled as inductance [100]. Therefore, two patch

structures facing each other in a unit cell can compose a shunt LC equivalent circuit [57, 58, 86, 97, 107, 108]. With the addition of a lumped resistor in between, the resulting dipole like structure can be modeled as an RLC network in the transmission line model. CST Microwave Studio (CST MWS) was used to perform parametric EM simulations of the dipole structure. Rogers RO4003C was used as the PCB substrate, and the unit cell geometry was optimized at the design frequency of 2.45 GHz. channelling traces were added as a design feature extending from one periodic boundary to the other, so that any number of unit cells in a row could be continuously connected to each other. The lumped resistor was strategically connected between the channelling traces, enabling parallel connection of the unit cells. A 3D model of the optimized FSS unit cell is shown in Fig. 3.1 (a), and the detailed dimensions of the unit cell geometry are provided in Fig. 3.1 (b). Using 1.524 mm substrate and 5 mm air spacer, the overall height of the optimized structure was only 6.524 mm, which is less than $1/18^{th}$ of the wavelength at the design frequency.

The absorption characteristics of the proposed design was simulated using periodic boundary conditions and Floquet ports in CST. The FSS structure was optimized for a linearly polarized plane wave incidence as depicted in Fig. 3.1 (c). Accordingly, the simulation and measurement results in this chapter assumes linearly polarized incident waves with properly aligned E-field vectors. Since the objective is energy harvesting rather than communication, there is no cross polarization concerns in this particular rectenna system. However, polarization losses can be expected if the incident wave is not linearly polarized, or if the E-field vector is not aligned with the FSS structure. As can be seen from the power flow diagram in Fig. 3.2 (a), the accepted power by the unit cell is evidently concentrated on the channelling traces and almost entirely collected on the lumped resistor. The percentage of the incident power that is accepted by the FSS is provided in Fig. 3.2 (b), and the distribution of the accepted power is provided in Fig. 3.2 (c). Simulation results of the periodic structure in CST revealed that 98.5% of the incident power is absorbed by the FSS at 2.45 GHz, 97% is absorbed by the lumped resistor, 1.1% is absorbed by the dielectric substrate, and 0.4% is dissipated as metallic loss. Fig. 3.2 (d) demonstrates the impact of resistor location to the overall FSS performance. Various offset positions of the resistor from the proposed location were simulated, and the results indicate that the FSS

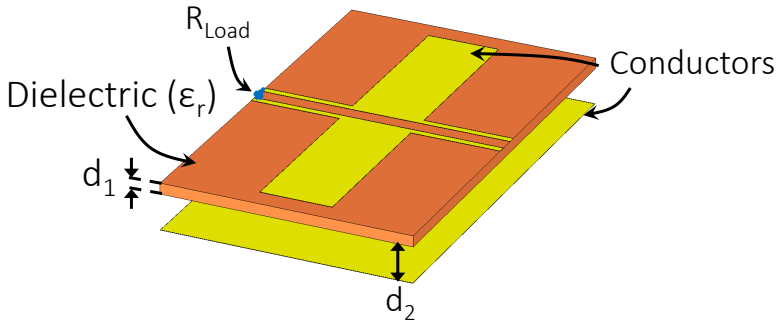

(a)

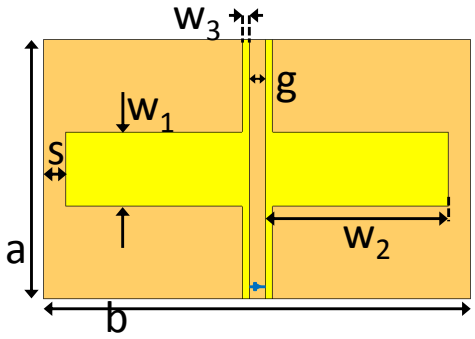

(b)

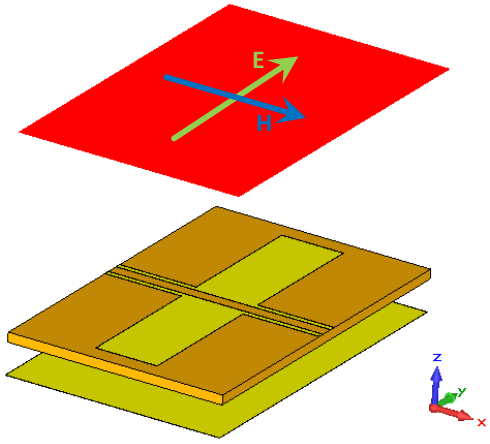

(c)

Figure 3.1: Unit cell of the absorber FSS (a) 3D view; dielectric substrate: RO4003C with 35 μm copper cladding, ϵ_r=3.55, d_1=1.524 mm, d_2=5 mm, R_{Load}=370 Ω (b) Dimensions in mm; a=34.9, b=57.5, s=3, w_1=10, w_2=24.7, w_3=1, g=2.1 (c) Polarization of the incident plane wave.

unit cell is not overly sensitive to the exact load location as long as the load is between the channelling traces.

A plane wave impinging on the FSS absorber was modeled with a transmission line

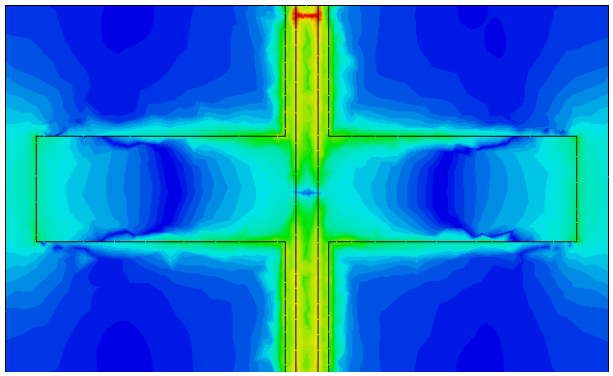

(a)

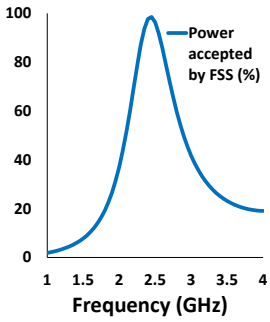

(b)

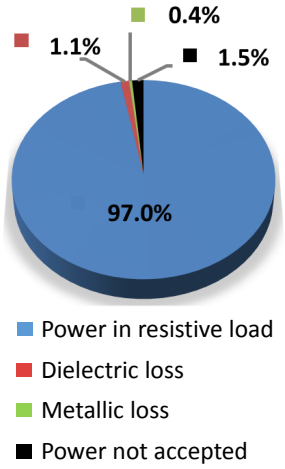

(c)

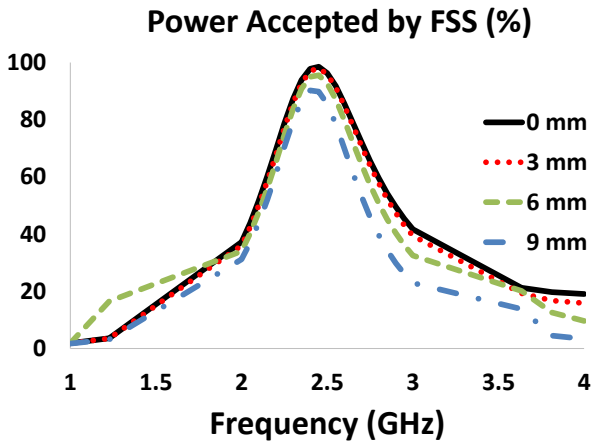

(d)

Figure 3.2: Absorption characteristics of the FSS: (a) Power flow diagram of the unit cell. The highest red intensity (color version) corresponds to 1.6×10^6 W/m^2 and the highest blue intensity corresponds to 0 W/m^2. (b) Absorption characteristics vs. frequency. (c) Distribution of the accepted power. (d) Impact of the resistor location on the overall FSS performance.

equivalent circuit. Fig. 3.3 (a) depicts two adjacent unit cells and indicates the key physical features of the periodic structure as they correspond to the equivalent circuit components in Fig. 3.3 (b). The interaction between the two unit cells is also represented in the circuit model. Y_0 denotes the free space admittance of 1/377 S, Y_1 denotes the characteristic admittance of the transmission line equivalent of the RO4003C substrate, and Y_2 denotes the characteristic admittance of the transmission line equivalent of the air spacer between the substrate and the conductive backing. The equivalent circuit of the proposed FSS unit cell was modeled with lumped elements. L and C1 represent the dipole arms, R represents the lumped resistor between the channelling traces, C2 represents the capacitance introduced by the two channelling traces within the unit cell, and C3 accounts for the capacitance introduced by the channelling traces between adjacent cells. RO4003C substrate with d_1=1.524 mm and ϵ_r=3.55 was modeled as a transmission line with electrical length of 8.6 degrees and characteristic admittance of $\sqrt{\epsilon_r}/377$=1/200 S. Air spacer with d_2=5 mm was also modeled as a transmission line with electrical length of 15 degrees and characteristic admittance of 1/377 S. The reflection coefficient of the equivalent transmission line circuit model in Fig. 3.3 (b) can be written as [101]:

$$\Gamma = \frac{Y_0 - (Y_S + Y_A)}{Y_0 + (Y_S + Y_A)} \tag{3.1}$$

where Y_0, Y_A, and Y_S are admittances of free space, the equivalent circuit of the FSS, and the short circuited transmission line, respectively. Γ is the reflection coefficient.

In its simplest form, a CAA requires a resistive sheet of 377 Ω to match the free space impedance for ideal absorption. In practice, however, applications may demand different absorption levels which in turn determines the equivalent resistance required from the CAA [101]. To obtain near unity absorption, a 370 Ω load resistor was used in this design. The lumped element values in the equivalent circuit were first estimated by using the relations given in [100], and then optimized using Advanced Design System (ADS) optimization tools. Fig. 3.4 provides a comparison of the FSS simulation in CST and its equivalent circuit simulation in ADS. Very good agreement was obtained between the absorption characteristics of the two models, validating the physical interpretation of the

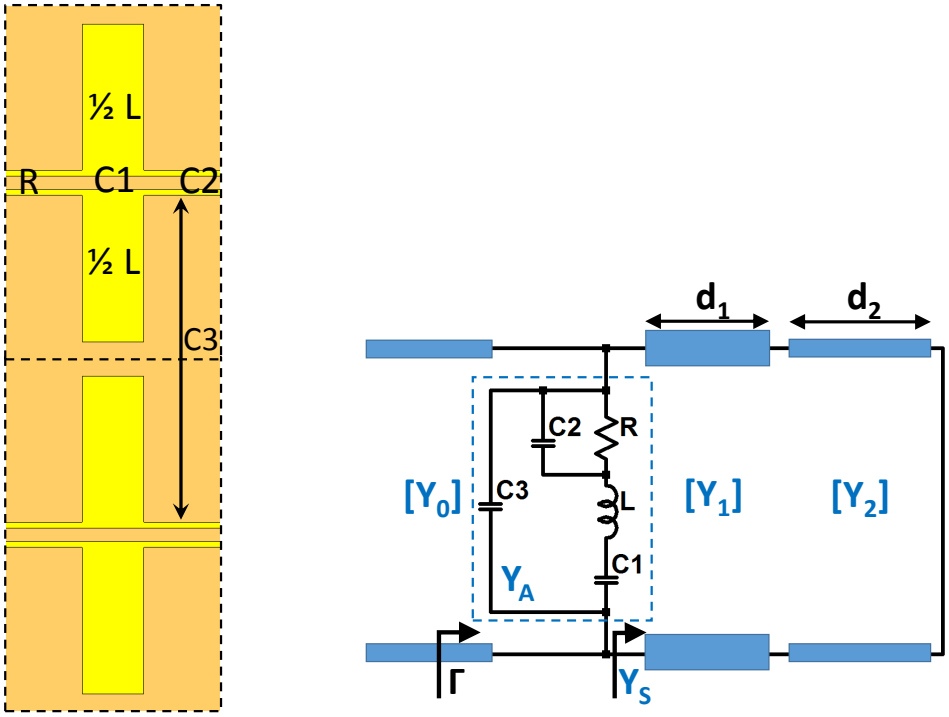

(a) (b)

Figure 3.3: (a) Description of the equivalent circuit model on unit cell geometry, (b) Schematic of the equivalent circuit with lumped element values of R=370 Ω, L=6.9 nH, C1=2.7 pF, C2=0.03 pF, C3=0.46 pF, Y_0=1/377 S, Y_1=1/200 S, Y_2=1/377 S, d_1=1.524 mm, d_2=5 mm.

unit cell geometry.

3.3 Full-wave Rectifier Design

A rectifier circuit can be constructed using a single-series mounted diode, a single-shunt mounted diode, or a diode bridge [26]. Amongst these, the single diode configurations serve as half-wave rectifiers, which is the most common implementation owing to its simple and

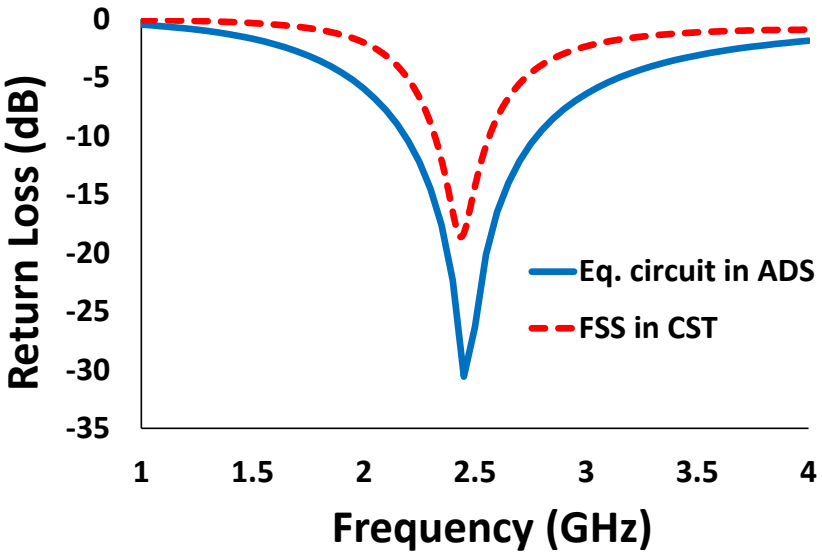

Figure 3.4: Return loss of the absorber FSS: full-wave EM simulation in CST compared with the equivalent circuit simulation in ADS.

low cost construction [19,21,23,24]. However, half-wave rectifiers are limited to using only one half cycle of the input AC signal. Diode bridge rectifier, on the other hand, realizes full-wave rectification by taking advantage of both half cycles of the input ac signal, which can lead to improved efficiencies [27, 30, 109]. Full-wave rectification has fewer examples compared to half-wave [28, 29]. This is mainly because it requires two diodes to be turned on for each half cycle, making it more suitable for higher power applications. Proposed FSS structure addresses the high input power limitation. Multiple unit cells in a row can be grouped together and feed the rectifier to obtain maximum efficiency. Therefore, a full-wave bridge rectifier is the chosen topology in this chapter.

A detailed analysis of a bridge rectifier for 2.45 GHz was provided in [30]. A similar approach was used here with a simplified matching circuit. Fig. 3.5 provides the ADS schematic of the full-wave rectifier circuit. HSMS-286P (by Broadcom, formerly Avago) was used as the quad bridge rectifier that consists of four Schottky diodes. C1 and C2 are dc blocking capacitors. C3, L1 and L2 are matching network components. R1 is

the output load resistor and C4 is the smoothening capacitor to minimize output ripples. Murata capacitors and inductors were preferred with the component families and values provided in Fig. 3.5.

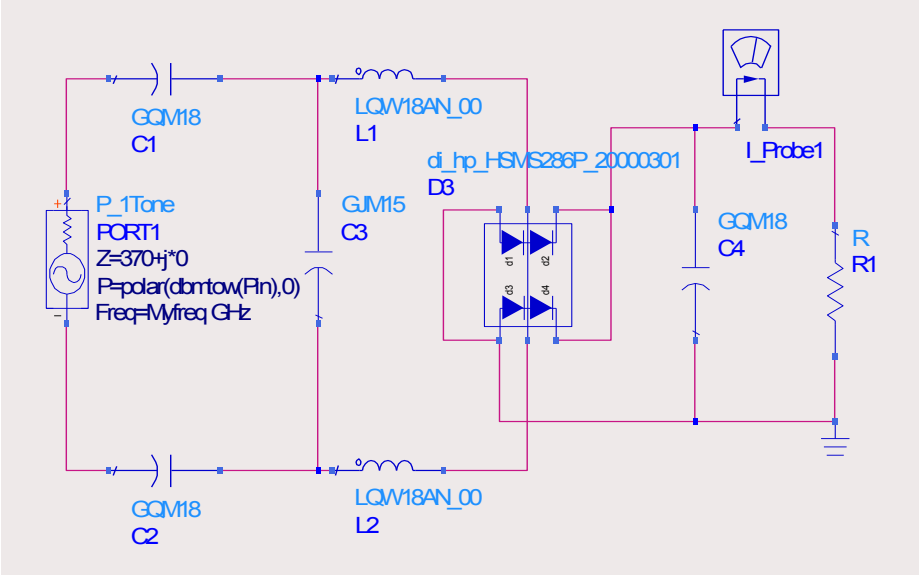

Figure 3.5: Full-wave rectifier schematic in ADS. C1=C2=C4=100 pF, C3=0.3 pF, L1=L2=12 nH, R1=1 kΩ.

Using Broadcom component library for HSMS-286P, the Large Signal S-Parameter (LSSP) solver of ADS was used to match the input impedance of the rectifier to 370 Ω. The matching components were particularly selected from commercially available discreet values. The entire schematic was then simulated using the manufacturers' component libraries. Fig. 3.6 shows the impedance matching of the rectifier. Excellent matching was obtained over a wide input power range.

Fig. 3.7 shows the rectification efficiency of the rectifier vs. frequency at various input power levels, and Fig. 3.8 provides the effect of the load R1 on the rectification efficiency. The results shown in Fig. 3.7 and Fig. 3.8 are consistent with the similarly designed full-wave rectifiers in literature [30, 109]. Here, the rectification efficiency is defined as:

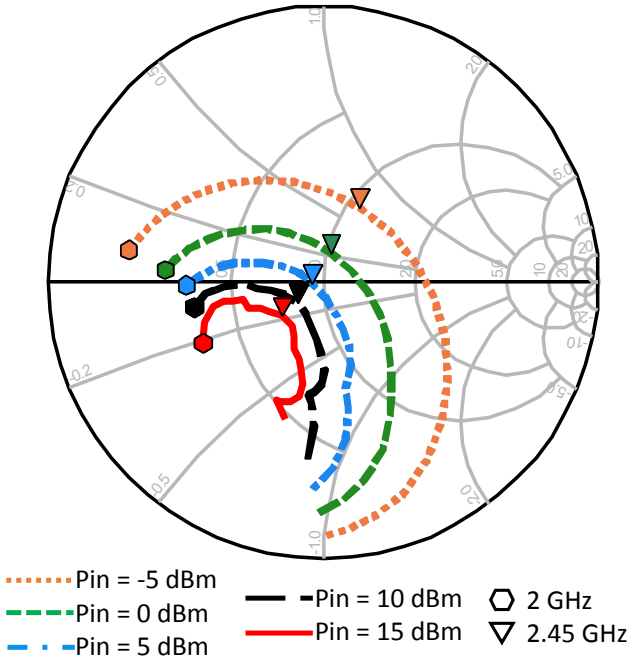

Figure 3.6: Input impedance of the full-wave rectifier (matched to 370 Ω) at various input power levels. Frequency range is 2 to 3 GHz.

$$\eta_{ac-dc} = \frac{P_{dc}}{P_{ac}}, \tag{3.2}$$

where P_{dc} is the power at the rectifier load resistor and P_{ac} is the input power at the rectifier input terminals. Although the efficiency in Fig. 3.7 is steadily increasing with higher input power, it is very important to note that this trend does not continue after 15 dBm where the rectifier reaches its peak efficiency. For input powers more than 15 dBm, the impedance match of the rectifier deteriorates and the efficiency becomes dramatically lower. Harmonic Balance solver of ADS was used to determine the input power dependence of the rectification efficiency, which is provided together with the measurement results in Section 3.4.

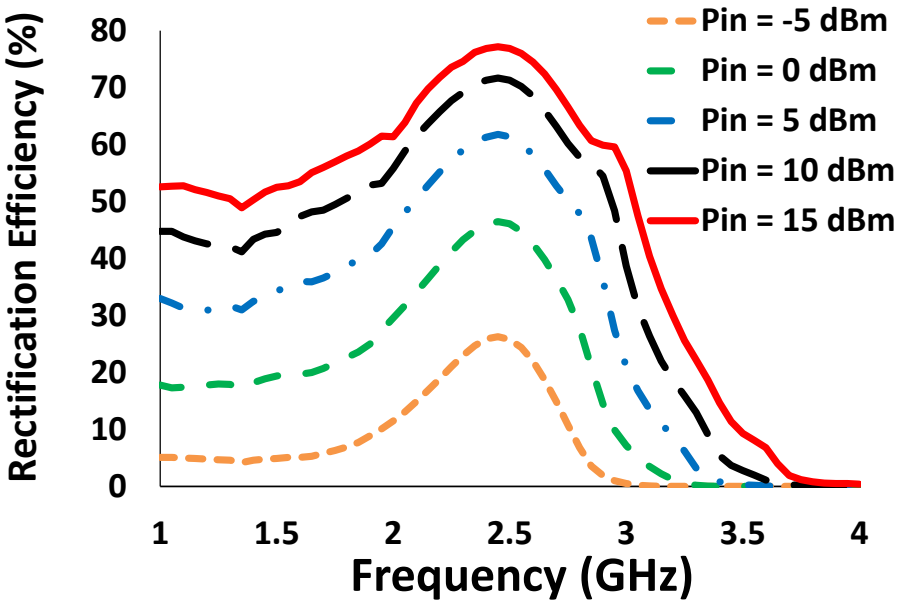

Figure 3.7: Rectification efficiency of the rectifier (η_{ac-dc}) vs. frequency at various input power levels.

3.4 Results and Discussion

The proposed FSS absorber was fabricated on a RO4003C substrate with 1.524 mm thickness and 35 μm copper cladding, as shown in Fig. 3.9. RO4003C board was 228.6 mm $\times$ 304.8 mm, which was enough area to print 5 x 6 = 30 unit cells. The full-wave rectifier layout was also printed at the end of each row, integrated to the continuous channelling traces. As discussed later in this section, this configuration combines the collected power from 6 unit cells and feeds into the rectifier. The center row was used for radiated measurements while others were terminated with 370 Ω resistors. Nylon spacers of 5 mm height (with negligible permittivity) were used to elevate the FSS substrate above a conducting plane of 228.6 mm $\times$ 304.8 mm. One of the main limitations of the previous FSS based energy harvesting systems was the need to implement individual rectifiers on each unit cell of the periodic structure. This resulted in lower efficiencies due to the small size of the EM

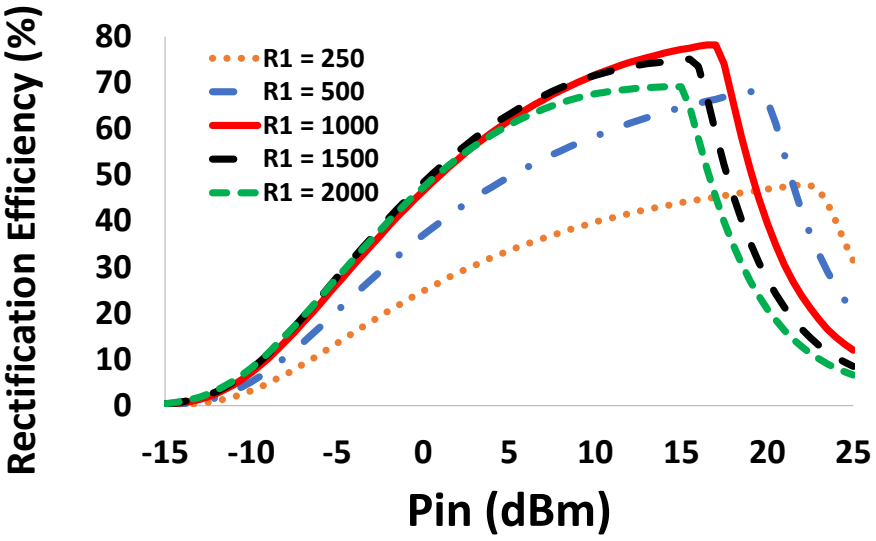

Figure 3.8: Rectification efficiency of the rectifier (η_{ac-dc}) vs. load resistor (R1) value.

collectors, (i.e., the unit cells). In this work, the channelling traces are utilized to combine the collected energy from multiple unit cells into a single rectifier. This approach makes it possible to increase the electrical size of the EM collector, hence the power collected per rectifier.

Overall performance of the rectenna was evaluated using the radiation-to-dc power conversion efficiency defined as:

$$\eta_{Rad-dc} = \frac{P_{dc}}{P_{Rad}} \tag{3.3}$$

where P_{dc} is the power at the load resistor and $P_{Rad.}$ is the total incident radiated power available at the physical area of the FSS row (enclosed by the dashed lines in Fig. 3.8) [27, 29]. η_{Rad-dc} can be written as the product of three efficiencies:

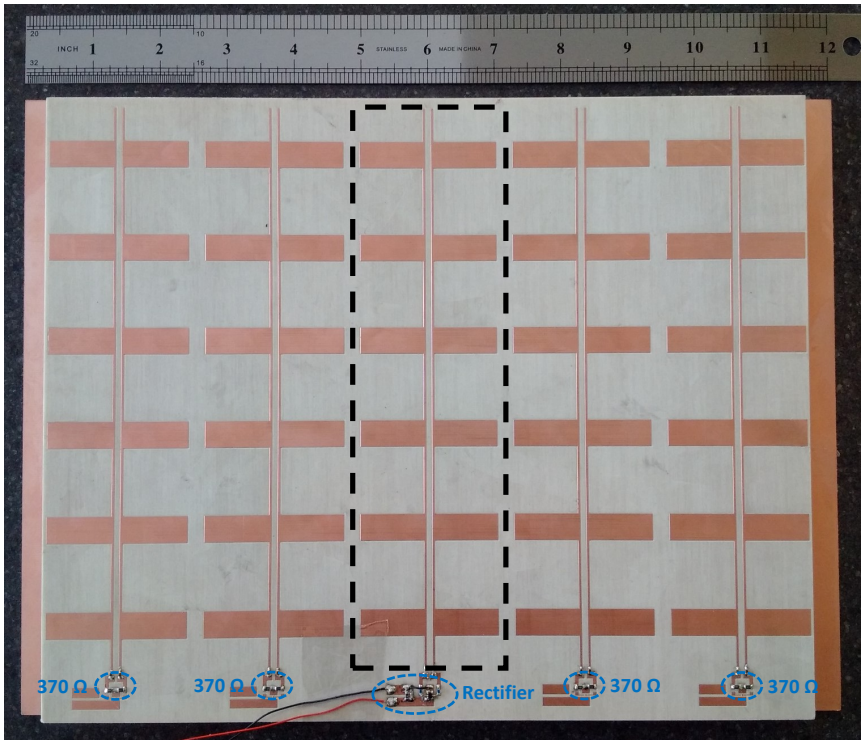

Figure 3.9: Fabricated FSS absorber integrated with full-wave rectifiers on RO4003C substrate mounted 5 mm above a copper plate. The marked rectangle indicates the physical area of the measured row.

$$\eta_{Rad-dc} = \eta_{Rad-ac} \times \eta_{Matching} \times \eta_{ac-dc} \tag{3.4}$$

η_{Rad-ac} represents the radiation-to-ac efficiency and it indicates the percentage of the available radiated power that is captured by the FSS at its resistive load. $\eta_{Matching}$ is the matching efficiency which indicates the percentage of the ac power that is actually delivered to the rectifier. η_{ac-dc} represents the ac-to-dc conversion efficiency and it indicates the percentage of the available input RF power of the rectifier that is converted to dc power at the load. The simulation results of η_{Rad-ac}, $\eta_{Matching}$, and η_{ac-dc} are given in Fig. 3.2 (b), Fig. 3.6, and Fig. 3.7, respectively. This section focuses on the integrated system

as a whole and evaluates the performance of the overall EM energy harvesting system. Radiation-to-dc conversion efficiency is a holistic metric for any rectenna system indicating the percentage of the available EM power (radiated) on a given surface area can be collected and converted into dc power at the system load.

A photograph of the measurement setup inside an anechoic chamber is shown in Fig. 3.10. A signal generator was used as the source. The output of the signal generator was amplified and fed into a standard gain horn antenna. The horn antenna was positioned such that the E-field of the incident wave on the FSS was parallel to the dipole arms. The FSS absorber was placed 1 m away from the horn antenna. Considering the design frequency of 2.45 GHz and the largest unit cell dimension of 57.5 mm, the measurement distance of 1 m satisfied the far field conditions. Measurements were carried out with varying incident power and frequency. The rectified dc voltage across the load was recorded using a digital multimeter and the collected dc power, P_{dc} was calculated for all test cases.

To obtain the efficiency in (3.3), the available incident power $P_{Rad.}$ was determined by applying the link budget calculations [27, 29]:

$$P_{Rad.} = S_{Rad.}\ A_p \tag{3.5}$$

$$S_{Rad.} = EIRP\ \frac{1}{4\pi d^2} \tag{3.6}$$

$$EIRP = P_s - L_c + G_a + G_h \tag{3.7}$$

where $EIRP$ is the effective isotropic radiated power of the transmitter, A_p is the physical area of the FSS unit cell, $L_{fs} = 1/4\pi d^2$ is the distance dependency, or the free space path loss of the EM energy expressed with inverse square law. The source power P_s was known from the signal generator. The losses of the coaxial cables were measured using Agilent E-5071C Vector Network Analyzer. The amplifier gain G_a was measured with a powermeter and the horn antenna gain G_h was obtained from its datasheet. Table 3.1 provides the

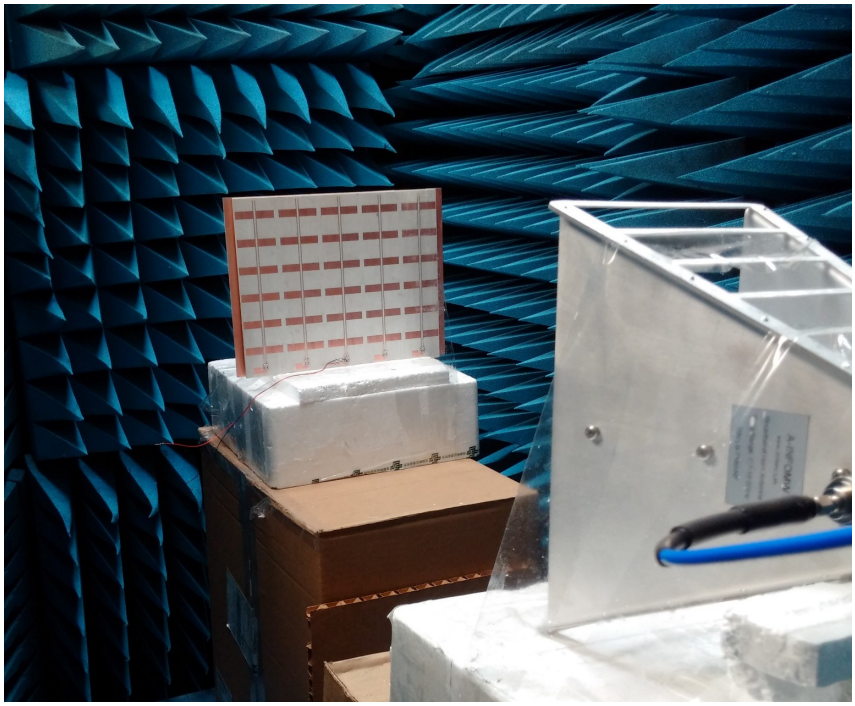

Figure 3.10: Measurement setup inside an anechoic chamber.

definitions of the link budget parameters and their values at 2.45 GHz. Available radiated power $P_{Rad.}$ was calculated to be 31.73 mW (15 dBm).

Fig. 3.11 (a) shows the measured radiation-to-dc conversion efficiency as a function of frequency. Peak efficiency was measured as 61% at 2.2 GHz. That is, the proposed rectenna was able to convert 61% of the available radiated power at its surface into practical dc power at its load. It is important to note that this efficiency should not be compared to the widely reported RF-to-dc conversion efficiencies in the literature. The RF-to-dc conversion efficiency is a measure of the rectifier circuit only where the RF power is fed

Table 3.1: Link budget parameters at 2.45 GHz

Transmitter Parameters	
Frequency (f)	2.45 GHz
Source output power (P_s)	2 dBm
Measured cable loss (L_c)	1.8 dB
Amplifier gain (G_a)	35.6 dB
Tx antenna (i.e. Horn) gain at 2.45 GHz (G_h)	9.4 dB
EIRP (P_s-L_c+G_a+G_h)	45.2 dBm
Propagation Parameters	
Distance (d)	1 m
Free space path loss (L_{fs})	11 dB
RF power density at panel surface ($S_{Rad.}$)	34.2 dBm/m^2
RF power density at panel surface ($S_{Rad.}$)	0.2635 mW/cm^2
Panel Parameters	
Physical area of the FSS unit cell (A_{uc})	20.07 cm^2
Physical area of the row with 6 unit cells (A_p)	120.41 cm^2

into the rectifier port (generally via an SMA connection), and the rectified dc power is measured at the load resistor. The recorded 61% efficiency in this work includes receiving the EM radiation, transferring the captured power to the rectifier, and converting it into dc power at the load. It should be noted that the incident radiated power used in the measurement setup was linearly polarized with properly aligned E-field vectors. True ambient power in real life can be composed of randomly polarized waves, which would degrade the overall rectenna efficiency.

Fig. 3.11 (a) also shows the expected efficiency curve over the same frequency range based on the simulation results of the different efficiencies involved. The "Simulated" trace is obtained by multiplying the simulation results of the sub-efficiencies from previous sections (as defined in (3.4)). Expected peak efficiency was 75% at 2.45 GHz. The lower measured efficiency and the frequency shift of 200 MHz can be mainly attributed to the

finite size of the FSS and its ground plane. Optimized unit cell characteristics are fairly accurate for the central cells, but not for the ones at the periphery of the FSS panel. Thus, the peripheral cells could cause mismatches and distorted absorption characteristics, which would lead to lower efficiency and shifted frequency. Nevertheless, the recorded 61% efficiency is much higher than the previously reported FSS based rectennas [63, 64].

Fig. 3.11 (b) shows the radiation-to-dc conversion efficiency as a function of the incident power. The load voltage was recorded as the source output was increased by 1 dB steps. The ac-to-dc conversion efficiency of the full-wave rectifier in Section 3.3 was simulated as a function of rectifier input power using Harmonic Balance solver of ADS. The obtained results are in agreement with those obtained using the state-of-the-art rectifier designs for similar input power levels [28–30]. In order to compare the measurements with simulation results, the RF power collected and delivered to the rectifier was calculated using the link budget equations (3.5) to (3.7). As shown in Fig. 3.11 (b), the measurements show very good agreement with the simulation results regarding the power dependency of the rectenna efficiency. Experimental results are slightly lower than those of the simulations mostly due to the finite size of the FSS panel.

The limitations in Fig. 3.11 (a) can be addressed with straightforward improvements. The frequency shift can be remedied by using a larger FSS panel to minimize the impact of peripheral unit cells. The bandwidth can be widened by optimizing the geometry for a lower resistor value for the FSS and matching the rectifier accordingly (albeit trading off absorption level). However, the power dependency in Fig. 3.11 (b) stems from the diode fundamentals and had been the main limitation of previously reported work [17, 18]. Rectifiers are non-linear circuits and their characteristics depend on the input power. Rectification efficiency peaks over a limited range of the input power and gradually degrades outside that range.

Measurement results in Fig. 3.11 show that the proposed design is an excellent integrated rectenna at 15 dBm input power to the rectifier. In the fabricated panel, 6 unit cells were connected to the rectifier and from Table 3.1 this meant that the peak efficiency was measured at a power density of 0.2635 mW/cm^2. However, the real life ambient RF

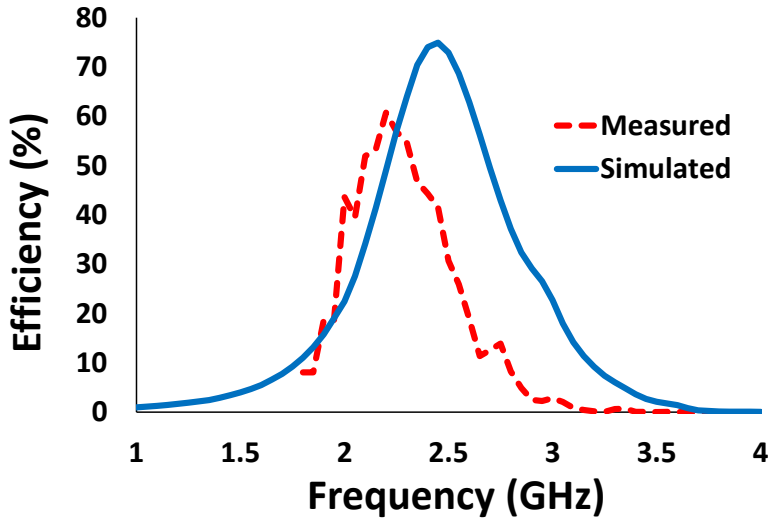

(a)

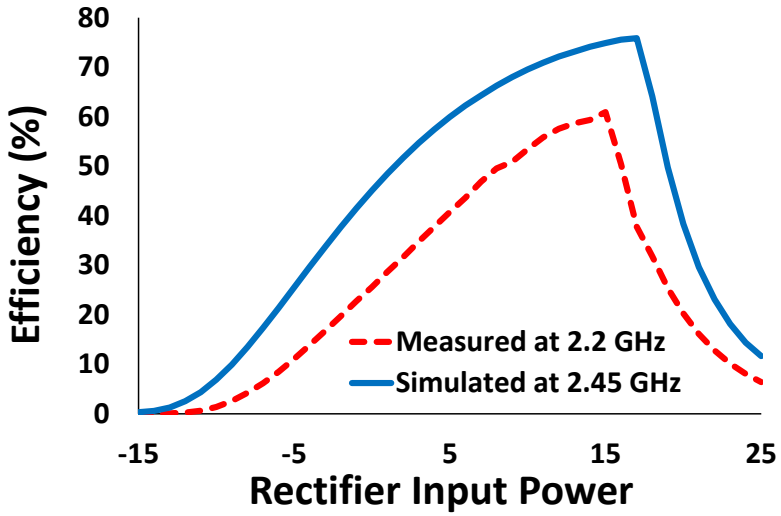

(b)

Figure 3.11: Measured radiation-to-dc conversion efficiency of the FSS based full-wave rectenna. (a) As a function of frequency. (b) As a function of rectifier input power.

power densities are lower than the experiment setup [14–16, 61]. One way to address this limitation is to employ a rectifier that is highly efficient at very low input power levels, and that can operate over a wide input power range. Unfortunately, the physical mechanisms of diodes make this solution almost impossible [62]. The alternative way to address the power dependency in Fig. 3.11 (b) is to utilize larger EM collectors per rectifier so that even at low power densities, the collected energy can still feed the rectifier at its peak conversion efficiency. This is one of the key features of the proposed FSS design in this chapter.

The scalable architecture of the proposed absorber is further demonstrated in Fig. 3.12 (a) which shows how multiple cells can be connected to a common resistive load. Since the physical area of the multi-cell structure expands with the number of cells (i.e. N), the total available radiated power incident on its surface also increases by a factor of N. This means the resistive load can absorb up to N times the power of a single cell. The concept was examined for N=1, 2, 4, 6, 8, 16, and 32 cells using CST. The power flow diagrams and the absorption efficiencies are provided in Fig. 3.12 (b) and (c), respectively. Simulation results are summarized in Table 3.2 for comparison. The results indicate that the proposed FSS unit cell is indeed scalable, but has some limitations. Absorption efficiency is highest for single unit cell at 97%, and it decreases as more cells are combined to the same load. However, even with lower efficiencies, the collected power at the load can increase significantly as the physical area gets larger. For example, the 16-cell configuration with 77% efficiency can collect more than 12 times the power of a single cell, clearly demonstrating the importance of a larger EM collector. The resistive load in these examples can be replaced with a matched rectifier, and the multi-cell rectenna can operate efficiently at much lower power densities than the levels required by a single unit cell rectenna. In terms of limitations, Table 3.2 shows that the absorbed power increases up to N=16 cells. After this point, even doubling the physical area does not provide any net benefit in terms of absorbed power. Therefore, the concept is only applicable up to a certain number of cells. It was also observed that the absorption bandwidth becomes narrower, and the optimum load resistance deviates from 370 Ω as N gets larger. However, it is important to note that the unit cell geometry in this chapter was optimized for maximum absorption in a single

cell implementation. This objective can be relaxed in favor of scalability, by designing for more consistent bandwidth and load behavior.

Table 3.2: Realized scalability

Multi-cell configuration	Physical area multiplier (1 unit cell = 20.07cm^2)	Max. absorption efficiency	Equivalent effective area multiplier	Ambient power density required to collect 15dBm at the load
N=1 cell	1	97%	0.97	1.6244 mW/cm^2
N=2 cells	2	80%	1.6	0.9848 mW/cm^2
N=4 cells	4	87%	3.48	0.4528 mW/cm^2
N=6 cells	6	79%	4.74	0.3324 mW/cm^2
N=8 cells	8	78%	6.24	0.2525 mW/cm^2
N=16 cells	16	77%	12.32	0.1279 mW/cm^2
N=32 cells	32	36%	11.52	0.1368 mW/cm^2

3.5 Conclusion

In this chapter, an FSS absorber design was presented that can be used for ambient RF energy harvesting or wireless power transfer. The FSS unit cell was constructed with built-in channelling features to combine the collected power from multiple unit cells. The excellent absorption characteristics of the periodic structure was demonstrated with 97% of the available energy being captured on its load. The FSS absorber was then integrated with a matched full-wave rectifier. The complete rectenna prototype was fabricated and tested through radiated measurements. 61% radiation-to-dc power conversion efficiency was measured which represents the combined efficiency of receiving the EM radiation, transferring the captured power to the rectifier, and converting it into dc power at the load. The scalability of the proposed FSS absorber was also discussed along with its limitations.

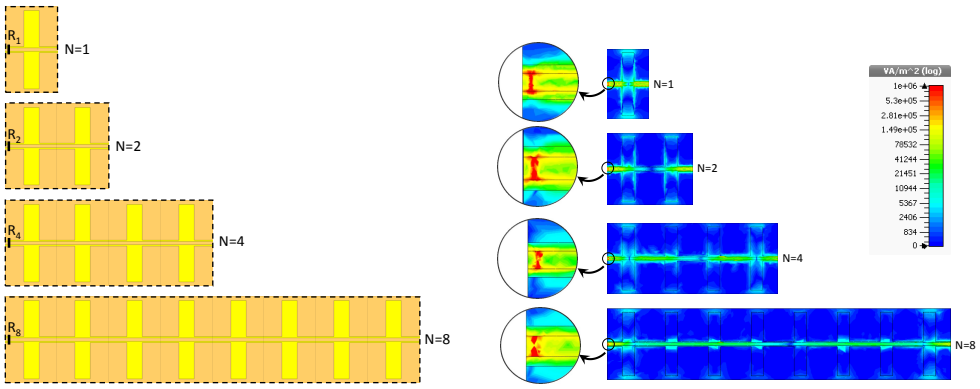

(a) (b)

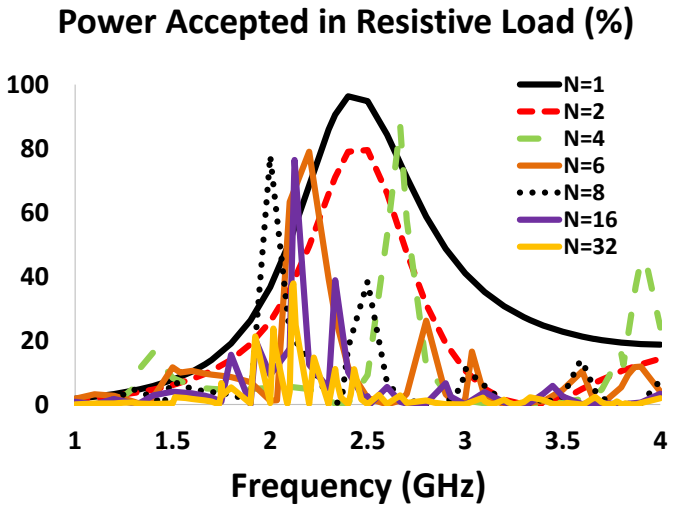

(c)

Figure 3.12: Scalable architecture of the proposed FSS based rectenna demonstrated. (a) Multiple cells in a row can be connected to a common resistive load; this is illustrated for N=1, 2, 4, and 8 unit cells. (b) Power flow diagrams showing the majority of the absorbed power being concentrated on the resistive load. (c) Power absorbed by the resistive load as a percentage of the available incident power.

Chapter 4

A Scalable, Dual-band Absorber Surface for Electromagnetic Energy Harvesting and Wireless Power Transfer

4.1 Introduction

Examples of FSS based rectennas had been reported in literature and the general approach has been to employ a rectification circuit in every unit cell. This resulted in excessive diode losses and low efficiencies due to low ambient power densities [63,64]. Recent studies have proposed solutions that involve applying corporate feed networks and innovative dc combining techniques [110–112]. However, corporate networks are still lossy and complex to manufacture. They are designed for a given structure and can not be scaled easily. Similarly, the dc combining techniques still employ large numbers of diodes and rely on lossy lumped elements to form a closed dc circuit. The novel energy harvesting surface presented in Chapter 3 demonstrated that it can address most of these limitations by using a periodic structure as its EM collector and by efficiently transferring the absorbed energy

into an integrated rectifier via built-in channelling traces [113]. This feature also enabled the rectenna to have a limited reconfigurable scalability depending on the available ambient power density [113].

In this chapter, a scalable EM energy harvesting surface is presented with dual-band capability. First, the design of the planar and low profile absorber surface is presented with built-in channelling traces. Then the details are provided for the full-wave rectifier that is matched to the absorber surface impedance for dual-band operation. The simulation results are validated experimentally by measuring three different integrated rectenna panels. The chapter is concluded by discussing the results and the limitations of the proposed concept.

4.2 Dual-band Absorber Surface

The proposed dual-band energy harvesting surface features two bow-tie shaped dipole structures in each unit cell, where bow-tie geometry was chosen for its inherent wide band properties. As shown in Fig. 4.1, two dipoles are connected through channelling traces that extend from one periodic boundary to the other, enabling continuous multi-cell configurations. Designing the absorber surface from CAA fundamentals was explained in Chapter 3 for a single-band absorber where the single element unit cell geometry made it possible to model the structure with an accurate transmission line equivalent circuit from previously established models [100, 101, 113, 114]. The dual-band absorber surface in this chapter utilizes the same fundamental principles with optimized dimensions for the desired dual-band frequencies. As shown with the 3D model in Fig. 4.1 (a), the absorber surface consists of a single layer printed circuit board backed by a conductive surface. The location of the lumped resistor was deliberately chosen between the channelling traces where it could be easily replaced with a rectifier. Rogers RO4003C was used as the PCB substrate with a dielectric constant of 3.55 and a thickness of 1.524 mm. All unit cell parameters were optimized for maximum absorption in the desired dual-band operation. The gap between the PCB substrate and the conductive surface was 5 mm as shown in Fig. 4.1 (a), and the other dimensions were as provided in Fig. 4.1 (b).

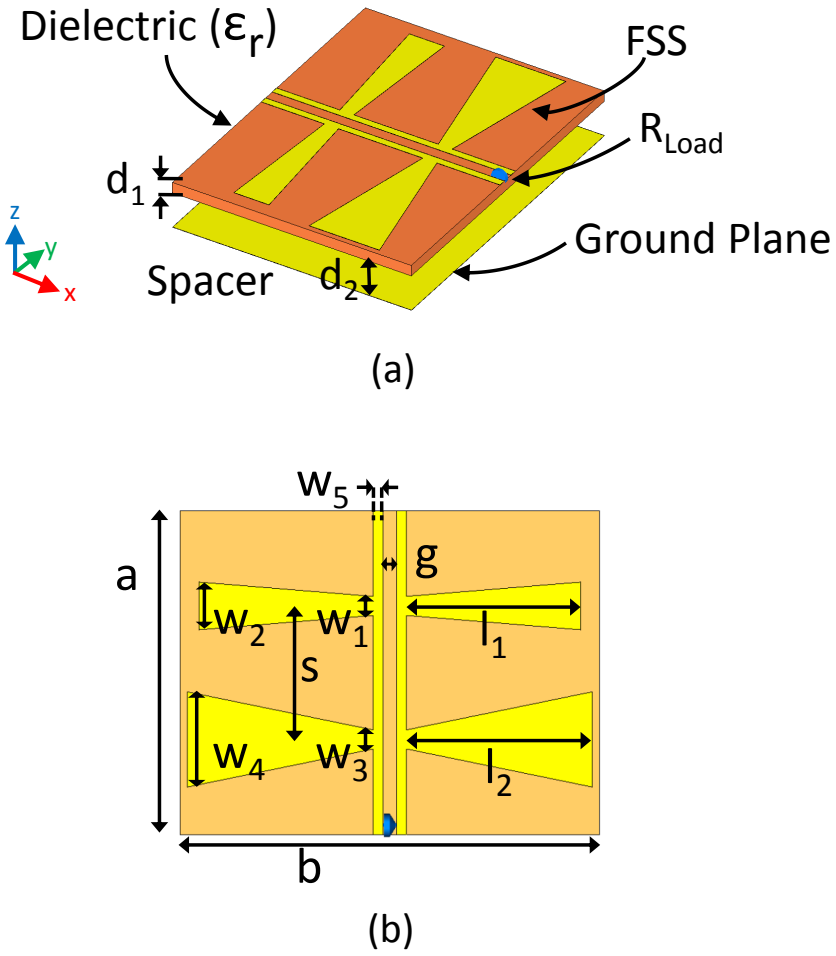

Figure 4.1: Unit cell of the dual-band energy harvesting surface. (a) 3D view; dielectric substrate: RO4003C with 35 μm copper cladding, ϵ_r=3.55, d_1=1.524 mm, d_2=5 mm, R_{Load}=360 Ω (b) Dimensions in mm; a=34, b=44, s=14, w_1=2, w_2=5, w_3=2, w_4=10, w_5=1, g=1.5, l_1=40, l_2=42.5.

Several recent studies have reported the actual measured ambient RF power densities in urban and semi-urban environments around the world [14–16]. Using these measured power levels as guidance, the design objectives of this work focused on the commonly

used GSM-1800 (centered at 1.85 GHz) and the Wi-Fi bands (centered at 2.45 GHz) due to their relatively high power densities. The proposed periodic absorber surface was simulated and optimized using periodic boundary conditions and Floquet ports in CST Microwave Studio [71]. The absorber surface was optimized for a linearly polarized plane wave incidence with E-field vectors aligned parallel with the bow-tie arms. Fig. 4.2 shows the Absorption Efficiency, which is defined as the percentage of the incident power that is accepted by the absorber surface. However, the accepted power here contains the power that appears across the resistive load as well as the dielectric and metallic losses that are dissipated. Therefore, the radiation-to-ac conversion efficiency can be further defined as:

$$\eta_{Rad-ac} = \frac{P_{ac}}{P_{Rad}}, \tag{4.1}$$

where P_{ac} is the power captured on the resistive load and P_{Rad} is the available incident power on the unit cell physical area. Fig. 4.2 shows the percentages of both the total accepted power as well as the power captured on the resistive load. The small difference between the two traces indicates the absorbed power that is dissipated as dielectric and metallic losses. At 1.85 GHz, 93% of the incident power is absorbed by the structure and 86% is collected on the resistive load. At 2.5 GHz, absorption by the surface and by the load is 85% and 83%, respectively.

The absorption efficiency in Fig. 4.2 clearly demonstrates a successful unit cell for a dual-band absorber surface. At this point, the traditional approach would be to replace the lumped resistor with a matched rectifier and replicate the unit cell to cover the desired surface area. Large numbers of such unit cells would be needed in order to harvest practical amounts of energy (due to low power densities [15, 16]). The rectifier would also need to operate at low input power levels which was demonstrated to be extremely difficult and inefficient [26]. Furthermore, additional mechanisms would be needed to combine the harvested energy from each unit cell into a single load (i.e. dc combiner), which was also shown to be inefficient in large structures [27, 45]. To address all these limitations, a scalable approach was proposed in Chapter 3 as a viable option to increase the physical area of the EM collector; hence, increasing the input power per rectifier [113]. The work in

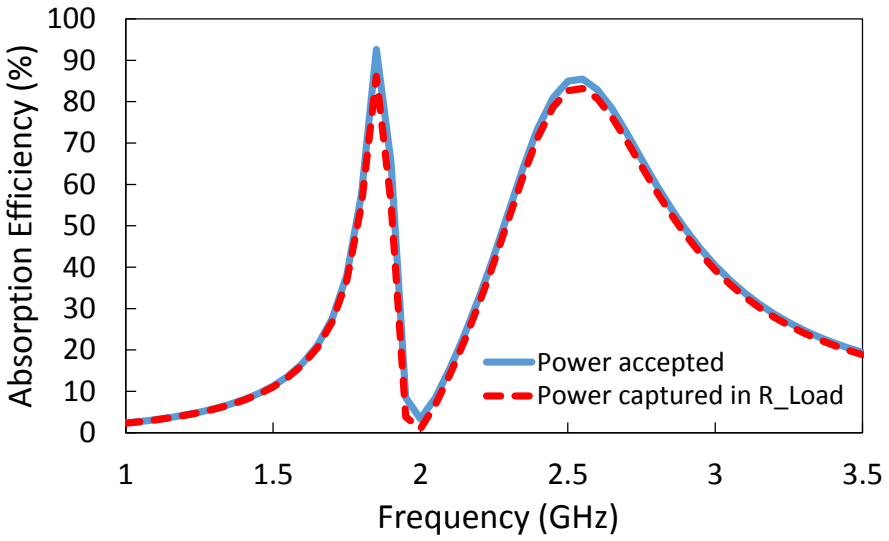

Figure 4.2: Absorption efficiency of the dual-band energy harvesting surface is demonstrated by the percentage of total available power accepted in the unit cell and the power concentrated on the resistive load. The difference is power lost in dielectric substrate and metallic losses.

this chapter builds on the previous concept to demonstrate the feasibility of a dual-band scalable absorber surface.

Fig. 4.3 (a) depicts a super cell of 4 unit cells all connected to a resistive load through continuous channelling traces and Fig. 4.3 (b) provides the simulated absorption efficiency of the super cell. Peak absorption occurs at 1.8 GHz and 2.3 GHz. Similarly, a super cell of 8 unit cells is shown in Fig. 4.4 (a) and its absorption efficiency is provided in Fig. 4.4 (b). Peak absorption occurs at 1.68 GHz and 2.12 GHz. It should be noted that the frequency shifts can be remedied by optimizing the design for specific applications. The goal in this chapter is to demonstrate the feasibility of the dual-band concept. Since the physical area of the super cells are 4 times or 8 times larger than the single unit cell area,

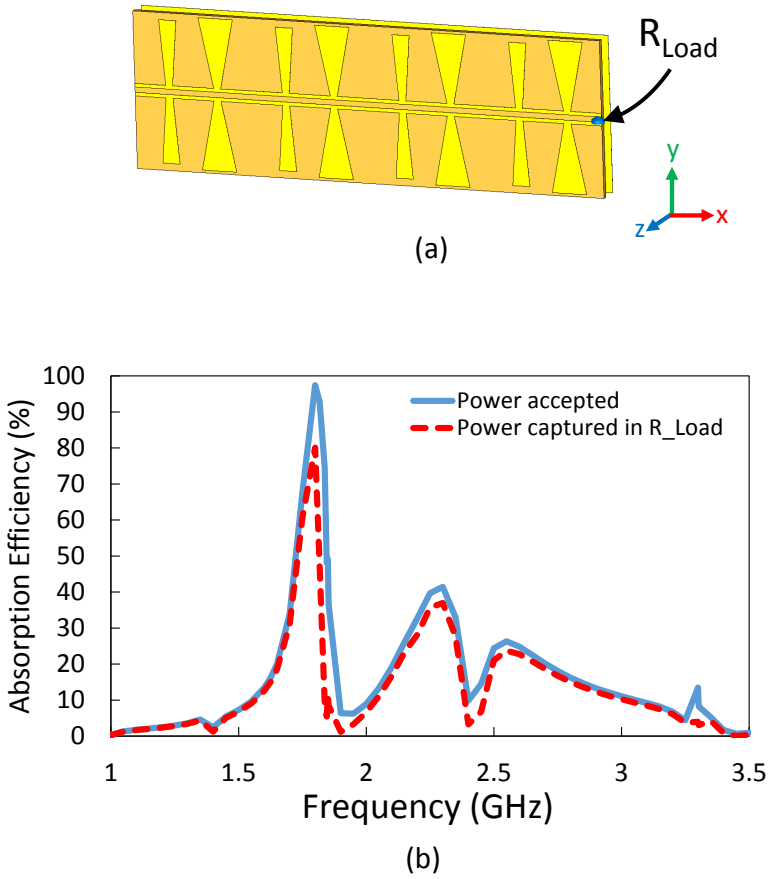

Figure 4.3: (a) Scalable architecture of the proposed dual-band energy harvesting surface is demonstrated in a super cell of 4 unit cells. Resistive load is shown at the end of the channelling traces (R_{Load}=360 Ω) (b) Absorption efficiency of the super cell configuration for N=4 is shown by the total accepted power in the super cell and the power concentrated on the resistive load as percentage of the available incident power. The difference between the two traces is the power lost in dielectric substrate and metallic losses.

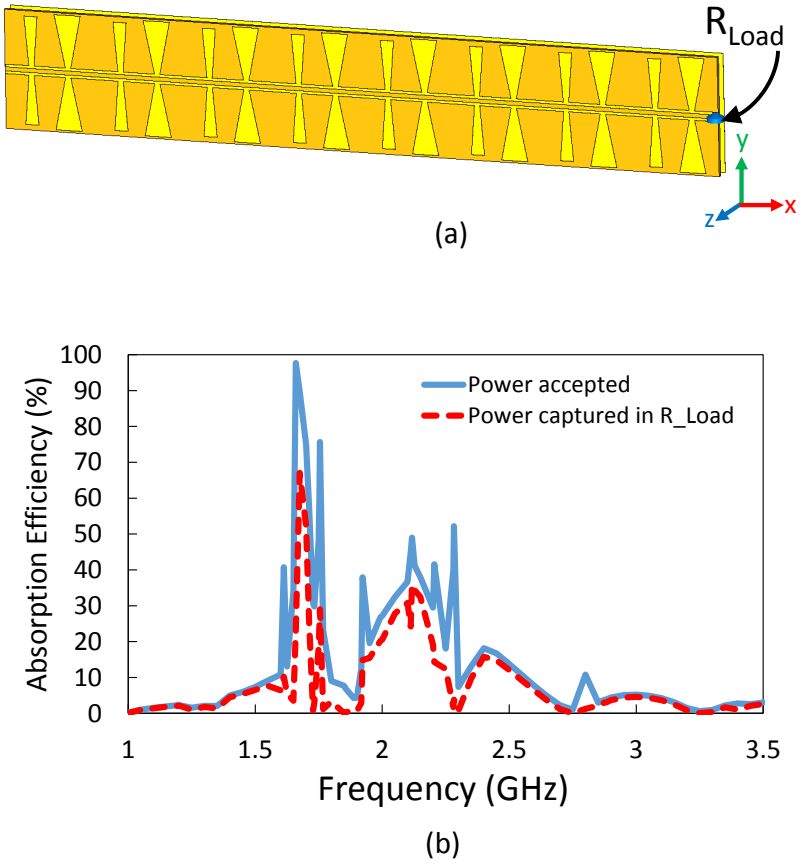

Figure 4.4: (a) Scalable architecture of the proposed dual-band energy harvesting surface is demonstrated in a super cell of 4 unit cells. Resistive load is shown at the end of the channelling traces (R_{Load}=360 Ω) (b) Absorption efficiency of the super cell configuration for N=8 is shown by the total accepted power in the super cell and the power concentrated on the resistive load as percentage of the available incident power. The difference between the two traces is the power lost in dielectric substrate and metallic losses.

total available energy is 4 times or 8 times larger. Therefore, even though the absorption efficiencies of the super cells seem lower than a single unit cell, because they utilize a larger physical area, total energy collected on the resistive load is larger. The importance of larger physical area is re-visited in Section 4.3 and 4.4 where the rectifier characteristics and measurement results are discussed.

4.3 Full-wave Rectifier

Advantages of full-wave rectifiers and their suitability for energy harvesting applications have been discussed earlier in Chapter 2 [113]. Detailed design steps of full-wave bridge rectifiers have also been provided in Chapter 2 and 3 [27, 30, 113]. In this section, similar design steps are followed to optimize a full-wave rectifier that is matched to 360 Ω. Fig. 4.5 provides the schematic in Keysight's Advanced Design System (ADS) for the circuit where HSMS-286P was used as the quad bridge rectifier [115]. C1 and C2 are dc blocking capacitors while C3, L1 and L2 are matching components. R1 is the output load resistor, and C4 is a shunt capacitor to reduce ripples. Murata low equivalent series resistance (ESR) capacitors and high-Q wire wound inductors were used with component families and values provided in Fig. 4.5.

The input impedance of the rectifier was matched to a 360 Ω load by simulating discrete, commercially available component values from the manufacturer's libraries in the large signal S-parameter solver of ADS. Built-in manufacturer models account for the component imperfections and parasitics, resulting in a more accurate representation of the prototype circuit. The optimized input impedance of the matched rectifier circuit is provided on a Smith Chart in Fig. 4.6 (a) and the input return loss with respect to a 360 Ω reference is provided in Fig. 4.6 (b). Primary objective here was to match the rectifier in both 1.85 GHz and 2.45 GHz bands for dual-band operation. Better than -10 dB return loss was achieved for both frequencies.

Fig. 4.7 provides the rectification efficiency of the rectifier versus frequency where the

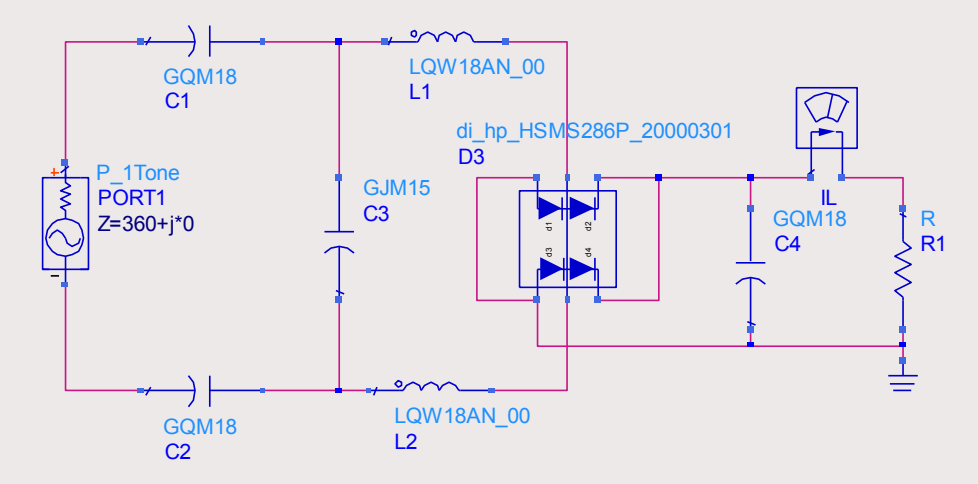

Figure 4.5: Full-wave rectifier schematic in ADS. C1=C2=C4=100 pF, C3=0.2 pF, L1=13 nH, L2=15 nH, R1=1 kΩ.

rectification efficiency is defined as:

$$\eta_{ac-dc} = \frac{P_{dc}}{P_{ac}}, \tag{4.2}$$

P_{dc} is the power at the rectifier load resistor and P_{ac} is the input power at the rectifier input terminals. For dual-band operation, the rectifier is optimized to cover 1.85 GHz and 2.45 GHz, which resulted in 75% conversion efficiency for both frequencies.

Fig. 4.8 provides the effects of the load resistor on the rectifier performance. Fig. 4.8 (a) shows how the rectification efficiency changes with the resistive load at 1.85 GHz, while Fig. 4.8 (b) gives the same information for 2.45 GHz. As expected, different load resistors are required to maximize the performance at different frequencies; 500 Ω gives 79% conversion efficiency at 1.85 GHz, while 1500 Ω gives 78% at 2.45 GHz. However, for dual-band operation with a common load, 1000 Ω was chosen to demonstrate the concept, which resulted in 75% and 76% efficiencies at 1.85 GHz and 2.45 GHz, respectively. It should be noted that the rectifier load value can be treated as an optimization parameter

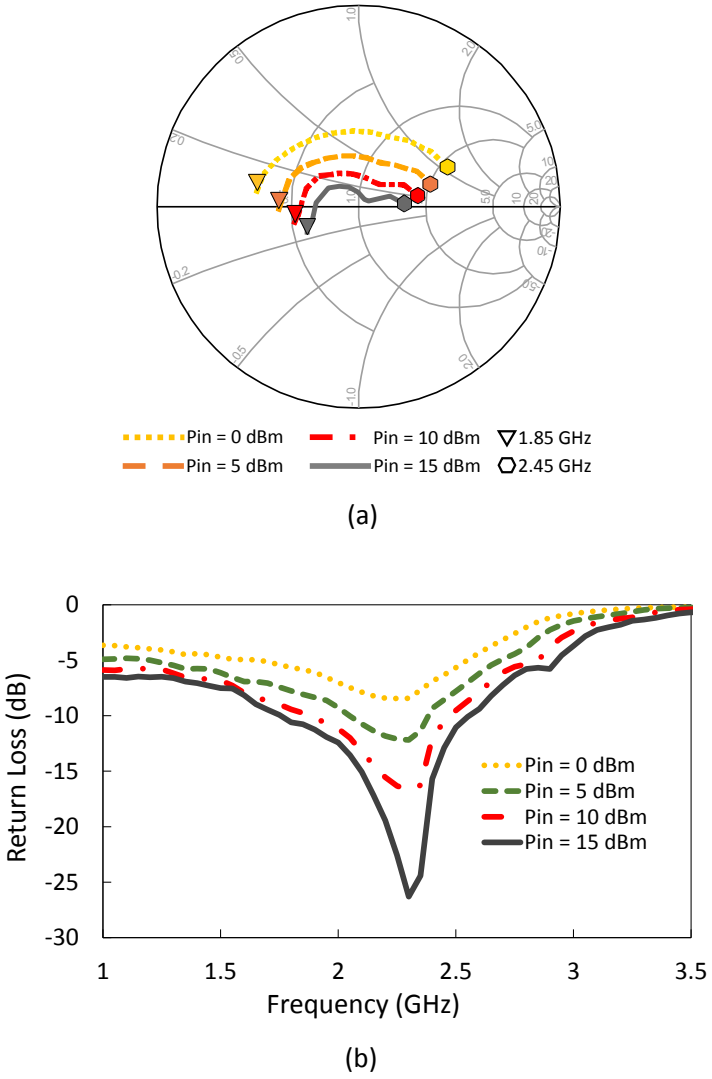

Figure 4.6: Input impedance of the full-wave rectifier is matched to 360 Ω; (a) complex input impedance is plotted on the Smith Chart at various power levels (b) magnitude of the input return loss is plotted against frequency at various power levels.

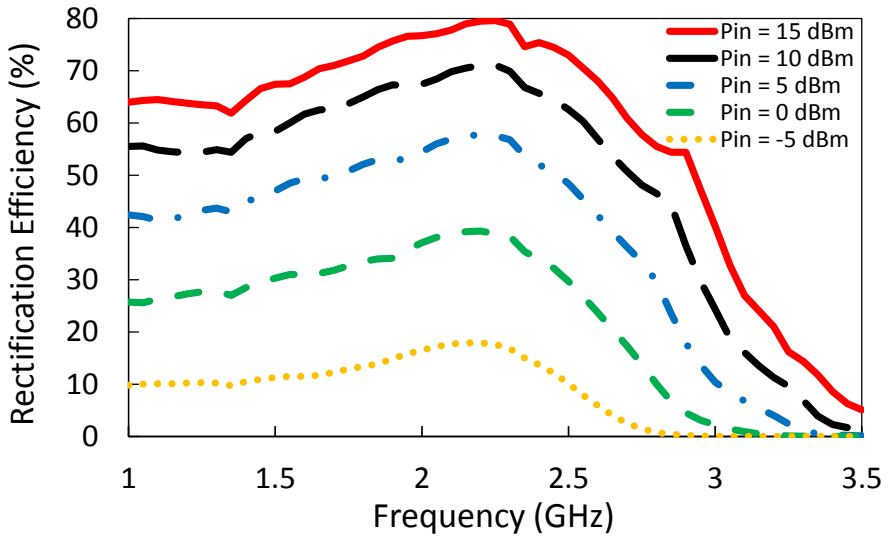

Figure 4.7: Rectification efficiency (η_{ac-dc}) vs. frequency at various input power levels.

depending on the application and the available power density. It can be instrumental in defining the balance or the trade-off between the two operational bands.

Another important observation from Fig. 4.8 is the rectifier's dependence on the input power. The rectification efficiency is very low at low input power levels and the peak efficiency is achieved near 15 dBm input, which is consistent with previously reported rectifiers [27, 30, 116]. However, given the low ambient RF energy densities, rectennas with typically small apertures would be extremely limited in terms of collecting enough power to operate such rectifiers efficiently [15, 16]. One way to address this limitation would be to improve the low power efficiency of rectifiers, which is outside the scope of this work but has been an active research area in the context of wireless power transfer and EM energy harvesting [62, 116]. This work proposes to address the same limitation by efficiently increasing the physical area of the rectenna to enhance the collected power at the rectifier input. Table 4.1 summarizes the simulation results of the three different configurations

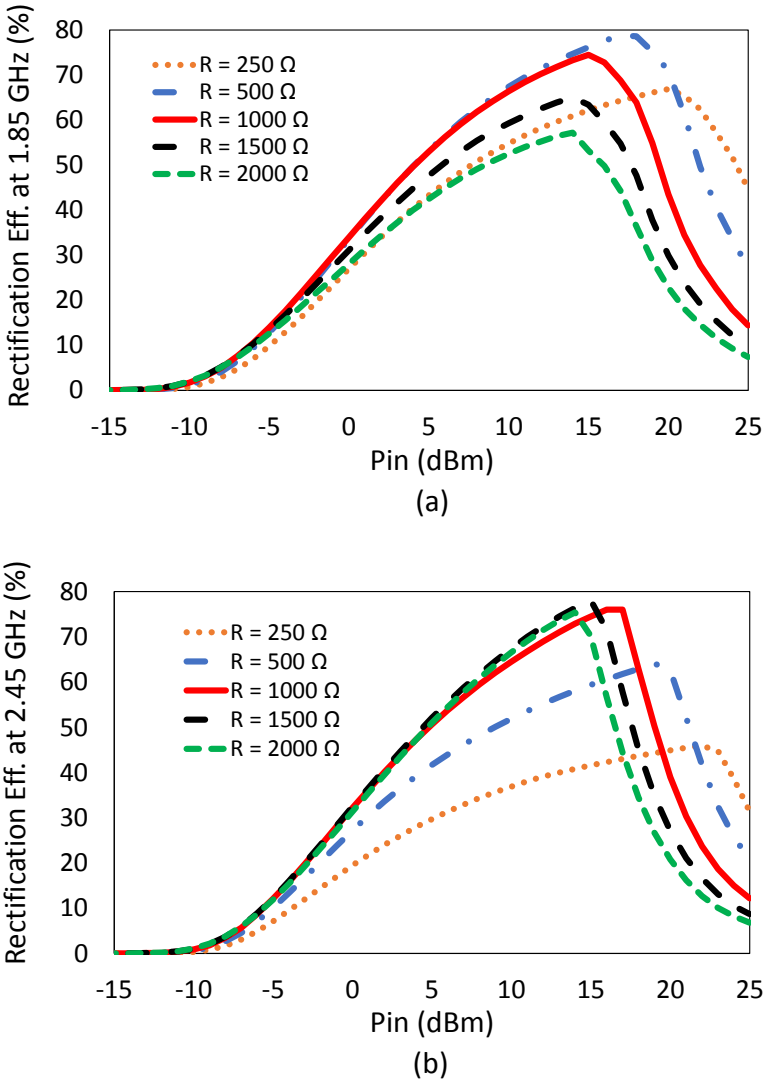

Figure 4.8: Rectification efficiency (η_{ac-dc}) vs. load resistance (a) at 1.85 GHz (b) at 2.45 GHz.

presented in Section 4.2. The resistive load in these examples can be replaced with a matched rectifier, and the multi-cell rectennas can operate efficiently at much lower power

densities than the levels required by a single unit cell rectenna.

Table 4.1: Realized benefit of increasing the rectenna area and efficiently channelling the absorbed energy

Rectenna configuration	LF: low freq. HF: high freq.	η_{Rad-ac}	Power density needed to collect 15dBm
N = 1 cell	LF	86%	2.46 mW/cm^2
Area= 14.96cm^2	HF	83%	2.55 mW/cm^2
N = 4 cells	LF	80%	0.66 mW/cm^2
Area=59.84cm^2	HF	37%	1.43 mW/cm^2
N = 8 cells	LF	67%	0.39 mW/cm^2
Area=119.68cm^2	HF	36%	0.73 mW/cm^2

4.4 Results and Discussion

The proposed absorber configurations were fabricated on Rogers RO4003C substrates with 1.524 mm thickness and 35 μm copper cladding. Fig. 4.9 (a) shows the first panel where the periodic structure is a single unit cell printed in a 4x5 configuration and Fig. 4.9 (b) shows the close up photo of the rectifier circuit. Fig. 4.9 (c) shows the second panel where the periodic structure is a super cell of 4 unit cells printed in a 2x5 configuration and Fig. 4.9 (d) shows the third panel where the periodic structure is a super cell of 8 unit cells printed in a 1x5 configuration.

It has been shown that the mutual coupling between the elements of a periodic structure can have a significant effect on the unit cell characteristics [27, 79, 113]. The full extent of these effects can only be measured in an infinite surface, but in practical terms, the majority of the coupling is caused by the adjacent cells. Therefore, even a finite size implementation

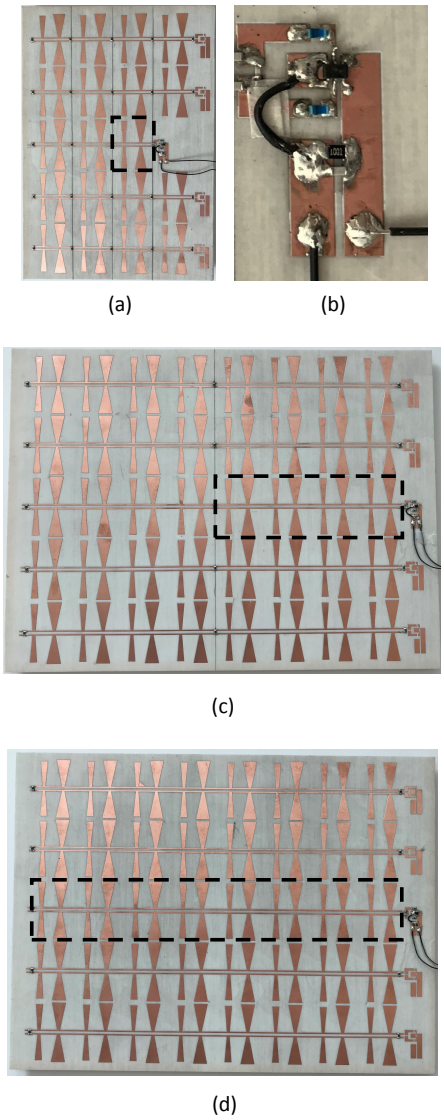

Figure 4.9: Fabricated rectenna panels on RO4003C substrate: (a) panel of rectennas with a single unit cell configuration (b) close-up photo of the full-wave rectifier (c) panel of rectennas with a super cell configuration of 4 unit cells (d) panel of rectennas with a super cell configuration of 8 unit cells.

can give a good approximation of the unit cell performance when the layout is carefully chosen [80, 81]. To prove the concept, all of the three panels were populated with as many unit cells as possible and the measurements were taken from the central elements as indicated by the dashed rectangles. In the case of Fig. 4.9 (a), all of the adjacent elements were populated except for one where the rectifier circuit was printed. In the case of Fig. 4.9 (c) and (d), the super cells were composed of multiple unit cells in a row which resulted in a longitudinal extension and there were multiple adjacent rows printed on the panels. Therefore, the measurements reflect the mutual coupling effects reasonably well, resulting in a good approximation for the unit cell performance when present in an infinite surface.

Overall rectenna performance was evaluated using the radiation-to-dc conversion efficiency defined as:

$$\eta_{Rad-dc} = \frac{P_{dc}}{P_{Rad}} \tag{4.3}$$

where P_{dc} is the power at the load resistor and P_{Rad} is the total incident power available at the physical area of the rectenna (enclosed by the dashed lines in Fig. 4.9) [27, 29]. η_{Rad-dc} can be further broken down as the product of three sub-efficiencies:

$$\eta_{Rad-dc} = \eta_{Rad-ac} \times \eta_{Matching} \times \eta_{ac-dc}, \tag{4.4}$$

where η_{Rad-ac} represents the radiation-to-ac efficiency, which was provided in Fig. 4.2, 4.3 and 4.4. $\eta_{Matching}$ is the measure of how well the rectifier was matched to 360 Ω surface impedance which was provided indirectly in Fig. 4.6. η_{ac-dc} represents the rectifier's conversion efficiency which was also provided through Fig. 4.7 and 4.8. Therefore, the expected overall rectenna performance can be obtained as the product of its simulated sub-efficiencies. To further verify the rectenna performance experimentally, the measurement setup depicted in Fig. 4.10 was used. Details of the efficiency calculations were provided in Chapter 3 [113]. The measurements in this chapter followed the same steps for dual-band frequencies and the efficiency calculations were performed with the new rectenna surface areas.

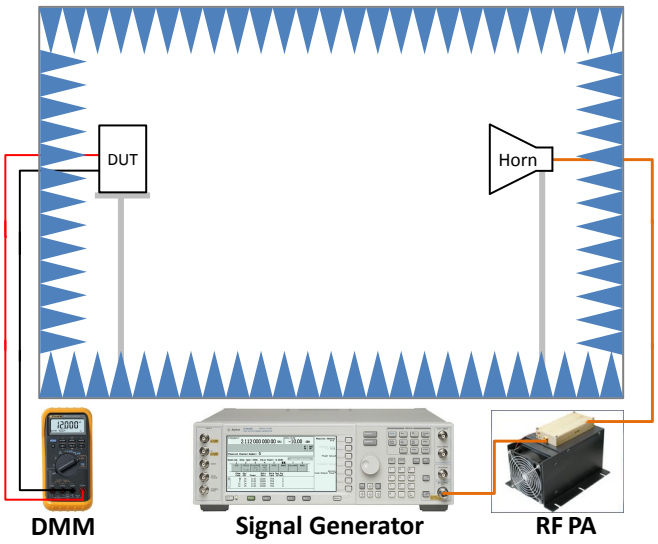

Figure 4.10: Schematic diagram for the measurement setup.

Fig. 4.11 shows the measurement results for all three panels. Radiation-to-dc conversion efficiency of the single unit cell rectenna is provided in Fig. 4.11 (a). Peak efficiency was measured as 52% and 53% at 1.85 GHz and 2.38 GHz, respectively. The efficiency reported here includes the absorption of the incident plane waves, transferring the captured energy to the rectifier and converting it into dc form at the resistive load. It should not be compared to the widely reported RF-to-dc conversion efficiency in literature - which is merely the rectifier conversion efficiency (equivalent to η_{ac-dc} sub-efficiency alone). Fig. 4.11 (a) also shows the simulated radiation-to-dc conversion efficiency over the same frequency range. Simulated trace is the product of the simulated sub-efficiencies as provided in previous sections and as defined in Equation (4.4). Fig. 4.11 (b) shows the simulated and measured radiation-to-dc conversion efficiency of the second panel which consists of a periodic structure with a super cell of 4 cells. Peak efficiency of the second panel was measured as 43% and 31% at 1.86 GHz and 2.37 GHz, respectively. Fig. 4.11 (c) provides the simulated and measured performance of the third panel which is a periodic structure with a super cell of 8 cells. Peak efficiency of the third panel was measured as 27% and

29% at 1.85 GHz and 2.37 GHz, respectively.

Fig. 4.11 (a) belongs to a single unit cell connected to one rectifier, while Fig. 4.11 (b) belongs to 4 unit cells all connected to one rectifier and Fig. 4.11 (c) belongs to 8 unit cells all connected to one rectifier. Therefore, even though the efficiency seems lower in super cell configurations, the larger physical area offsets the lower efficiency, resulting in a larger total absorbed and rectified power as the rectenna physical area increases. Table 4.2 compares the three rectennas and their measurement results. The rectified dc power at the resistive load is expressed as the percentage of the available incident power on one unit cell area of each configuration. For example, at the lower frequency band, a rectenna with a single unit cell can convert 52% of the available ambient power into dc, while a rectenna with a super cell of 4 unit cells can convert more than 3 times this ratio. This comparison clearly shows the benefit of using a larger rectenna area and how it can be used as a viable solution to obtain efficient rectenna operation in low power densities. The proposed dual-band energy harvesting surface in this chapter demonstrates a viable concept for increasing the rectenna physical area and efficiently channelling the absorbed energy to the rectifier.

Table 4.2: Comparison of the measurement results demonstrating the benefit of increased rectenna area

Rectenna configuration	LF: low freq. HF: high freq.	Overall Rad. to DC Conv. Eff.	Rectified DC power at the load as % of the available power on one unit cell area
N = 1 cell	LF	52%	52%
	HF	53%	53%
N = 4 cells	LF	43%	172%
	HF	31%	124%
N = 8 cells	LF	27%	216%
	HF	29%	232%

The measured results of all three panels are generally in good agreement with the simulations, demonstrating a successful dual-band operation. Slightly lower efficiency and frequency shifts in the measured performance can be attributed to the finite size of the

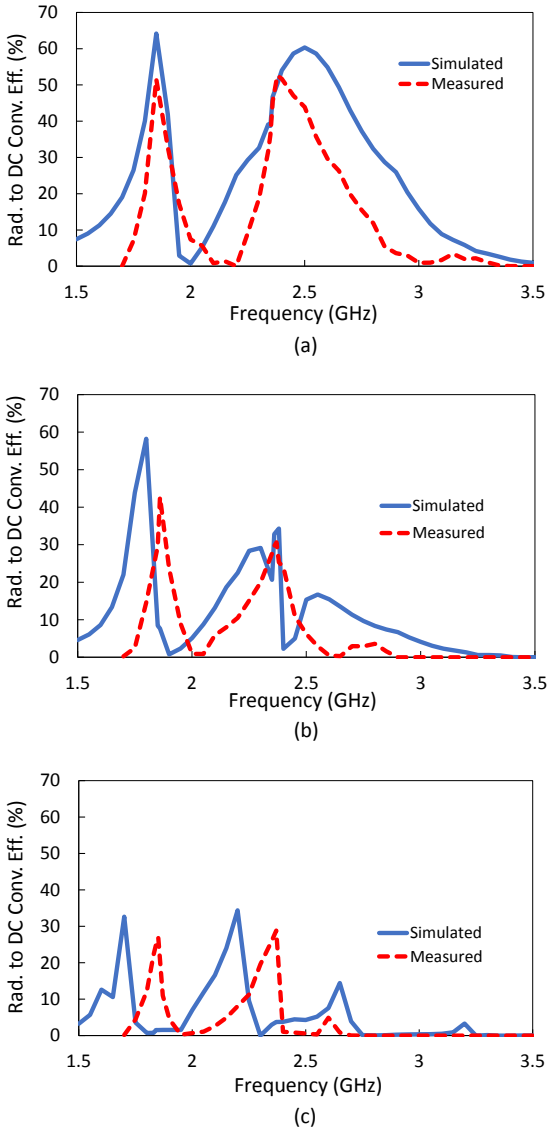

Figure 4.11: Measured Radiation-to-dc conversion efficiency of the dual-band energy harvesting surface (a) Rectifier connected to a single unit cell. (b) Rectifier connected to a super cell having 4 unit cells. (c) Rectifier connected to a super cell having 8 unit cells.

panels and the fabrication tolerances. During optimization, it was observed that the performance of the absorber surface is sensitive to trace widths and gaps especially around the channelling traces and the bow-tie terminals. Seemingly small fabrication tolerances can cause noticeable degradation in the absorption efficiency and impedance mismatch, resulting in frequency shifts and lower overall efficiencies.

4.5 Conclusion

A dual-band energy harvesting surface was presented with strong absorption characteristics and minimal dielectric losses, thus making it a good candidate for wireless power transfer and energy harvesting applications. Its scalability in terms of increasing the collected power per rectifier was also demonstrated by combining multiple unit cells via continuous channelling traces. The absorber surface was connected to a matched full-wave rectifier to form a fully integrated rectenna. Three different rectenna panels were fabricated and tested to demonstrate the feasibility of the concept. A single unit cell rectenna achieved 52% and 53% radiation-to-dc power conversion efficiencies at 1.85 GHz and 2.38 GHz, respectively. Larger super cells resulted in lower efficiencies but the overall collected and rectified power was demonstrated to be appreciably larger than the single unit cell implementation.

Chapter 5

A Scalable, Dual-polarized Absorber Surface for Electromagnetic Energy Harvesting and Wireless Power Transfer

5.1 Introduction

In this chapter, the concept of scalable energy harvesting surface is further extended with dual-polarization capability. First, the unit cell construction of the proposed dual-polarized absorber is explained and its absorption characteristics are analyzed when subjected to linearly polarized incident plane waves with E-field vectors perpendicular to each other. Then, a full-wave rectifier is presented with a matched impedance to the absorber surface for dual-polarized operation. The absorber surface and the rectifier are fabricated as an integrated rectenna prototype. Experimental validation is provided to demonstrate the efficient, scalable and dual-polarized energy harvesting system. The chapter is concluded by discussing the results and limitations of the proposed concept.

5.2 Dual-polarized Absorber

The unit cell of the proposed dual-polarized energy harvesting surface consists of a *cross* structure formed by two bow-tie dipoles placed concentric and 90 degrees apart. The frequency of operation was chosen to be 2.45 GHz because of its common usage and relatively high available ambient power densities [14–16]. Bow-tie geometry was chosen for its inherently wide band characteristics. As shown in Fig. 5.1, the unit cell is constructed with two Rogers RO4003C substrates backed by a ground plane. The dual-polarized structure is printed on the top surface of the 1st substrate as shown in Fig. 5.1 (a). The channelling traces for one polarization are printed on the bottom layer of the 1st substrate and for the other polarization on the bottom layer of the 2nd substrate as shown in Fig. 5.1 (b). Therefore, there are dielectric layers providing separation between the periodic surface and the two planes where the channelling traces are implemented. The bow-tie dipoles are connected to the channelling traces using the vias at the feed terminals. Fig. 5.1 (c) and Fig. 5.1 (d) demonstrate the overall compact structure with the detailed dimensions. Rogers RO4003C substrate thickness was 1.524 mm and the air gap was 5 mm, making the overall thickness of the absorber surface 8.05 mm.

The proposed design was simulated and optimized using the periodic boundary conditions and Floquet ports in CST Microwave Studio [71]. To optimize the dimensions for maximum efficiency, linearly polarized plane waves were used with E-field vectors aligned with the bow-tie dipoles. Fig. 5.2 shows the optimized absorption characteristics when the incident E-field is parallel to y-axis (E_y). Fig. 5.2 (a) depicts the orientation of the periodic structure with respect to the incident plane wave. Fig. 5.2 (b) shows the power flow diagram of the unit cell which clearly indicates the bow-tie dipole aligned in the y-axis is primarily responsible for the EM absorption in this polarization. Fig. 5.2 (c) shows the channelling traces looking from the back of the unit cell while the ground plane and dielectric substrates are hidden. The channelling traces along the x-axis are connected to the bow-tie dipole along the y-axis and Fig. 5.2 (c) clearly indicates the absorbed power is primarily channelled through these traces to the resistive load connected at the end of the traces. Fig. 5.2 (d) provides the simulated Absorption Efficiency, which is defined as the

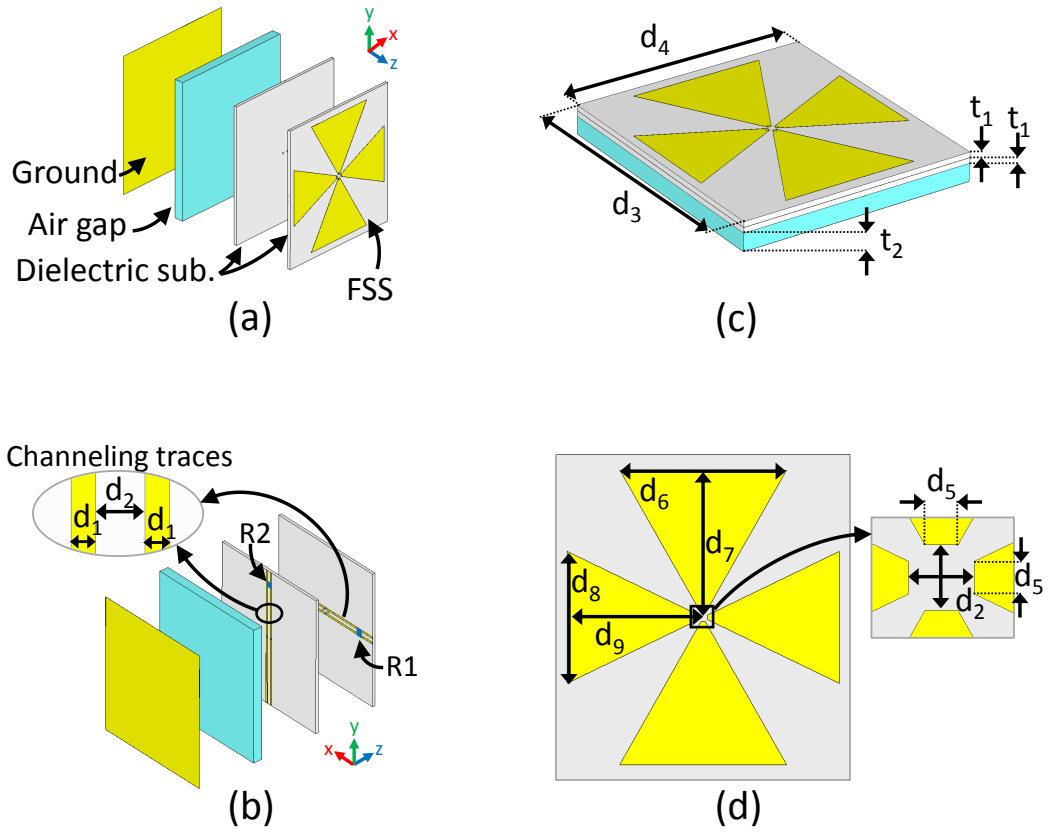

Figure 5.1: Unit cell geometry of the dual-polarized absorber (all dimensions in mm). (a) Front view of the layer-by-layer assembly; dielectric substrate: RO4003C with 1 oz copper cladding, ϵ_r=3.55. (b) Rear view of the layer-by-layer assembly; d_1=1 , d_2=2, R1=R2=Load resistor (c) Isometric view, d_3=67, d_4=74, t_1=1.524, t_2=5. (d) Top view, d_5=1, d_6=38, d_7=33.5, d_8=30, d_9=31.

percentage of the incident power that is accepted by the absorber surface. However, the accepted power here contains the power that appears across the resistive load as well as the dielectric and metallic losses that are dissipated. Therefore, the radiation-to-ac conversion efficiency is further defined as:

$$\eta_{Rad-ac} = \frac{P_{ac}}{P_{Rad}}, \tag{5.1}$$

where P_{ac} is the power captured on the resistive load and P_{Rad} is the available incident power on the unit cell physical area. At the design frequency of 2.45 GHz, 99.5% of the incident power is absorbed and 91% is exclusively collected on the resistive load (R1). The difference is dissipated in terms of dielectric and ohmic losses. Fig. 5.2 (d) also shows the cross polarization discrimination of the unit cell; while 91% of the incident power is collected on R1, only 0.1% appears on the R2.

Fig. 5.3 shows the absorption characteristics for the other polarization; when the incident E-field is parallel to the x-axis (E_x). Fig. 5.3 (a) depicts the orientation of the periodic structure with respect to the incident plane wave. Fig. 5.3 (b) and Fig. 5.3 (c) show the power flow diagrams of the unit cell looking from top view and bottom view, respectively. As expected, the bow-tie dipole along the x-axis is primarily absorbing the incident energy and the channelling traces connected to it (along the y-axis) are transferring the absorbed energy to the resistive load. Fig. 5.3 (d) provides the simulated absorption efficiency of the unit cell and the distribution of the accepted power. At 2.45 GHz, 96% of the incident power is absorbed and 86% is exclusively collected on the resistive load (R2). The difference is dissipated in terms of dielectric and ohmic losses. The absorption on R1 is less than 1% for this polarization.

It should be noted that the absorption efficiencies for both E_x and E_y polarizations are very high but they are not identical. This can be explained by the fact that the unit cell is a three dimensional structure and the channelling traces for different polarizations are routed at different layers. The via lengths are different and the optimized bow-tie dimensions are not identical.

Having established the unit cell performance, Fig. 5.4 and Fig. 5.5 demonstrate the scalable architecture of the absorber surface. Fig. 5.4 (a) illustrates a super cell configuration where multiple unit cells are grouped together along the x-axis and connected through the continuous channelling traces to a common resistive load. Fig. 5.4 (b) provides the simulated radiation-to-ac conversion efficiency of various super cell configurations

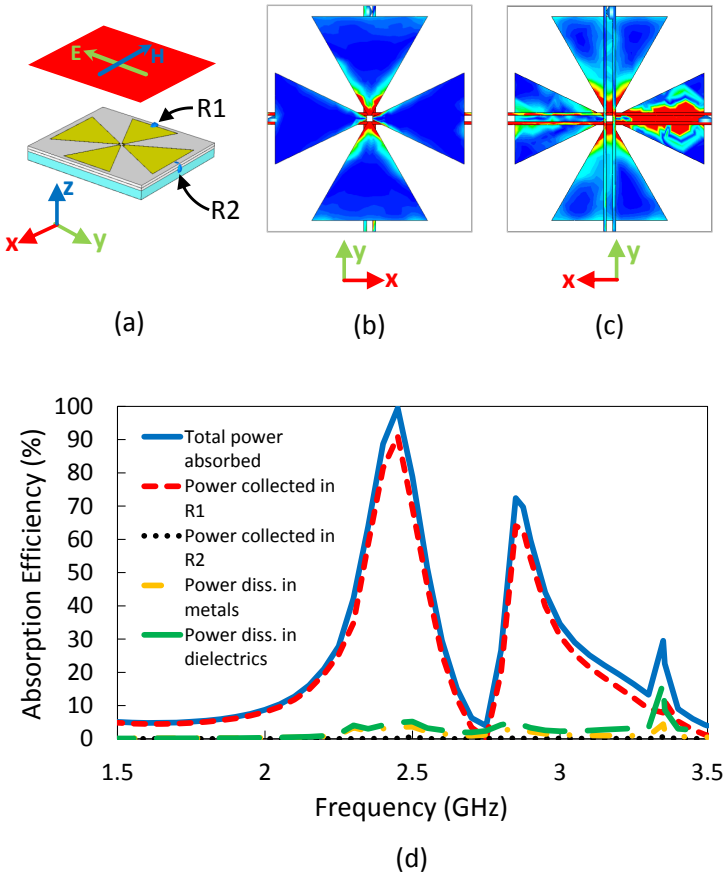

Figure 5.2: Power flow diagram and the absorption characteristics of the unit cell when illuminated with E-field parallel to y-axis. The highest red intensity corresponds to 11,000 VA/m2 and the highest blue intensity corresponds to 0 VA/m2. (a) Illustration of the incident plane waves. (b) Top view of the unit cell demonstrating how the bow-tie shape along y-axis is absorbing the EM energy. (c) Back view of the unit cell demonstrating how the channelling traces along the x-axis (which are connected to the feed points of the bow-tie along the y-axis) are transferring the captured EM energy to the resistive load. (d) Absorption efficiency of the structure demonstrated by the percentage of total available power accepted in the unit cell and the power concentrated on the resistive load.

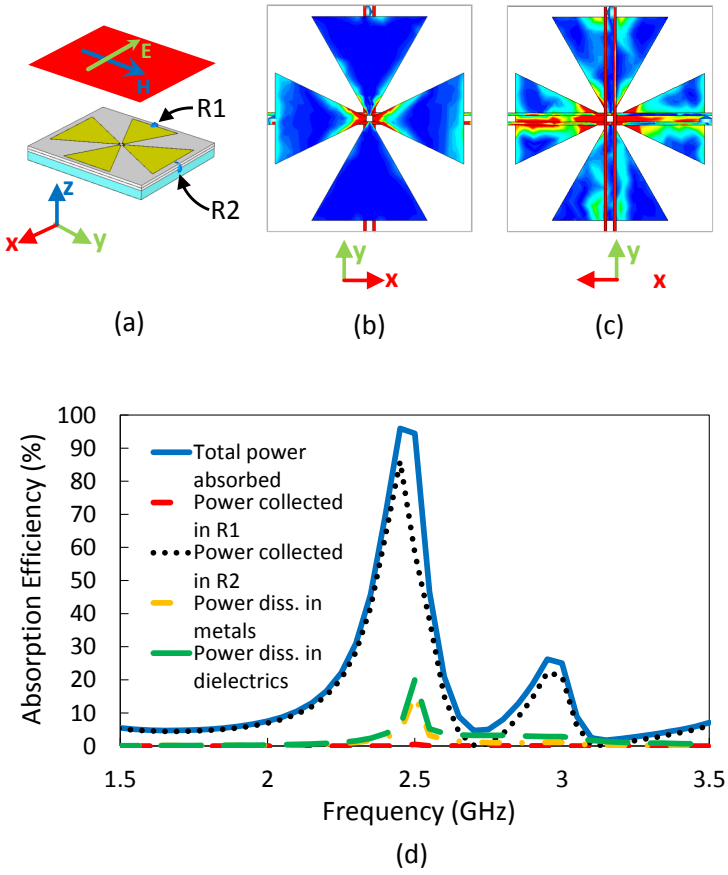

Figure 5.3: Power flow diagram and the absorption characteristics of the unit cell when illuminated with E-field parallel to x-axis. The highest red intensity corresponds to 11,000 VA/m2 and the highest blue intensity corresponds to 0 VA/m2. (a) Illustration of the incident plane waves. (b) Top view of the unit cell demonstrating how the bow-tie shape along x-axis is absorbing the EM energy. (c) Back view of the unit cell demonstrating how the channelling traces along the y-axis (which are connected to the feed points of the bow-tie along the x-axis) are transferring the captured EM energy to the resistive load. (d) Absorption efficiency of the structure demonstrated by the percentage of total available power accepted in the unit cell and the power concentrated on the resistive load.

when subjected to incident plane waves with E-field parallel to the y-axis (E_y). Fig. It should be emphasized that Fig. 5.4 (b) represents the collected power on the resistive load as percentage of the available incident power on the physical surface of the super cell (i.e. dielectric and ohmic losses are already subtracted from the total absorbed power). Radiation-to-ac conversion efficiency is the highest for the single unit cell at 91%, and it decreases as more cells are grouped together. Comparable radiation-to-ac conversion efficiency for super cells of N=4, 8 and 16 are 77%, 65% and 38%, respectively.

Fig. 5.5 (a) illustrates a super cell configuration along the y-axis where multiple cells are grouped together and connected through the channelling traces to a common resistive load. Fig. 5.5 (b) provides the simulated radiation-to-ac conversion efficiency of the super cell when it is subject to incident plane waves with E-field parallel to the x-axis (E_x). Similar to E_y polarization, efficiency is the highest for the single unit cell at 86%, and it decreases as more cells are grouped together. The radiation-to-ac conversion efficiency for super cells of N=4, 8 and 16 are 86%, 57% and 48%, respectively for this polarization.

For both polarizations, the radiation-to-ac conversion efficiency decreases as more cells are grouped together. However, when the increased physical area of the super cell is taken into account, the total collected power transferred to the resistive load increases significantly. The results of Fig. 5.4 (b) and Fig. 5.5 (b) are summarized in Table 5.1 where the realized benefit of using super cells and increasing the rectenna area is clearly illustrated. The increase in the physical area more than offsets the efficiency degradation, resulting in a net increase in total absorbed power. Considering a rectifier generally works most efficiently within a limited input power range, the larger super cell rectennas can operate at lower ambient power densities and still collect the required amount of power to operate the rectifier efficiently. This is illustrated in Table 5.1 by comparing different super cell configurations in order to collect 15 dBm on the resistive load. The resistive load in these configurations can be replaced with a matched rectifier and the larger super cells can operate as efficient rectennas at much lower power densities than the levels required by a single unit cell rectenna [113]. For E_x polarization, a single cell configuration would need 0.742 mW/cm^2 ambient power density in order to collect 15 dBm at its resistive load,

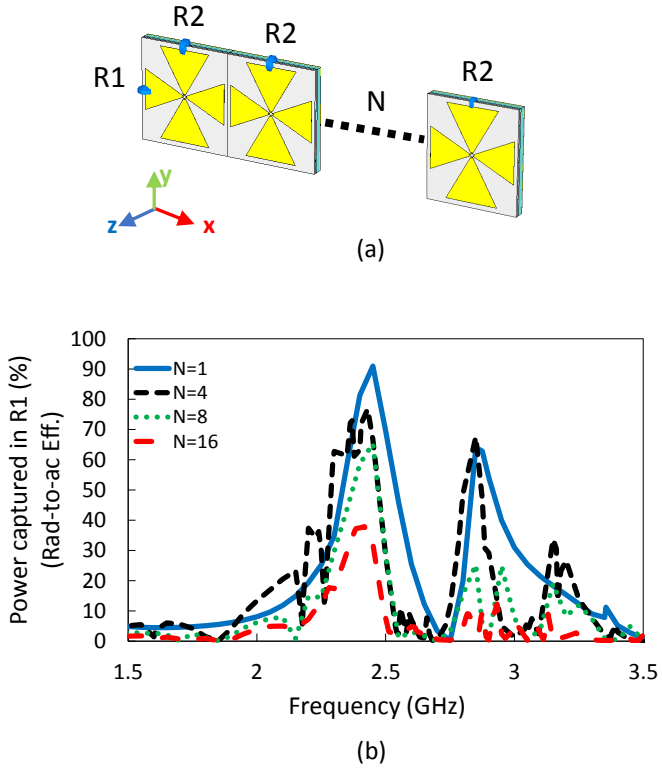

Figure 5.4: (a) Scalable architecture of the proposed dual-polarized energy harvesting surface is demonstrated in a super cell of N unit cells grouped along x-axis. Resistive loads are shown at the end of the channelling traces. (b) Radiation-to-ac conversion efficiency of the super cell configuration for N=1, 4, 8 and 16 is shown by the power concentrated on the resistive load (R1) as percentage of the available incident power. Super cell is illuminated with E-field parallel to y-axis.

while a super cell of N=16 would only need 0.083 mW/cm^2 to collect the same amount of power. In other words, the single cell implementation needs 8.9 times more ambient power density than that is needed by the super cell of N=16.

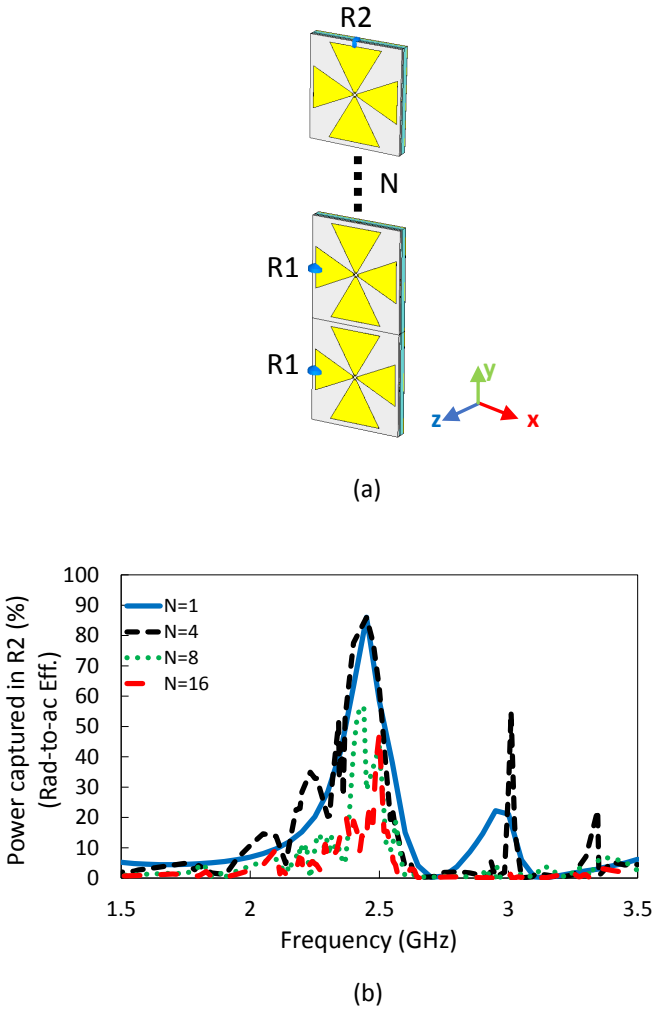

Figure 5.5: (a) Scalable architecture of the proposed dual-polarized energy harvesting surface is demonstrated in a super cell of N unit cells grouped along y-axis. Resistive loads are shown at the end of the channelling traces. (b) Radiation-to-ac conversion efficiency of the super cell configuration for N=1, 4, 8 and 16 is shown by the power concentrated on the resistive load (R2) as percentage of the available incident power. Super cell is illuminated with E-field parallel to x-axis.

Table 5.1: Realized benefit of increasing the rectenna area and efficiently channelling the absorbed energy

Super cell configuration	Incident E-field	Rad-to-ac Conv. Eff.	Power density needed to collect 15 dBm
N = 1 cell	E_x	86%	0.742 mW/cm^2
Area= 49.58cm^2	E_y	91%	0.701 mW/cm^2
N = 4 cells	E_x	86%	0.185 mW/cm^2
Area=198.32cm^2	E_y	77%	0.207 mW/cm^2
N = 8 cells	E_x	57%	0.140 mW/cm^2
Area=396.64cm^2	E_y	65%	0.123 mW/cm^2
N = 16 cells	E_x	48%	0.083 mW/cm^2
Area=793.28cm^2	E_y	38%	0.105 mW/cm^2

5.3 Full-wave Rectifier

Full-wave rectifiers have been demonstrated to be a viable solution for energy harvesting and wireless power transfer applications [27]. In Chapter 2, 3 and 4, it was shown that full-wave rectifiers are particularly suitable for the scalable periodic surfaces where they can be integrated into the super cells of the harvesting surface and benefit from the total collected power [113]. In this section, similar design steps are followed to develop a full-wave rectifier that is matched to 50 Ω, which is the impedance required by the super cells shown in Fig. 5.4 and 5.5.

Fig. 5.6 depicts the rectifier schematic in Keysight's Advanced Design System (ADS) where HSMS-286P was used as the quad bridge rectifier [115]. C1 and C2 are dc blocking capacitors while L1, L2, L3, L4 and C3 are matching components. RL is the output load resistor, and C4 is a shunt capacitor to reduce ripples. Murata low equivalent series resistance (ESR) capacitors and high-Q wire wound inductors were used with component families and values provided in Fig. 5.6.

The full-wave rectifier is matched to a 50 Ω source by simulating commercially available

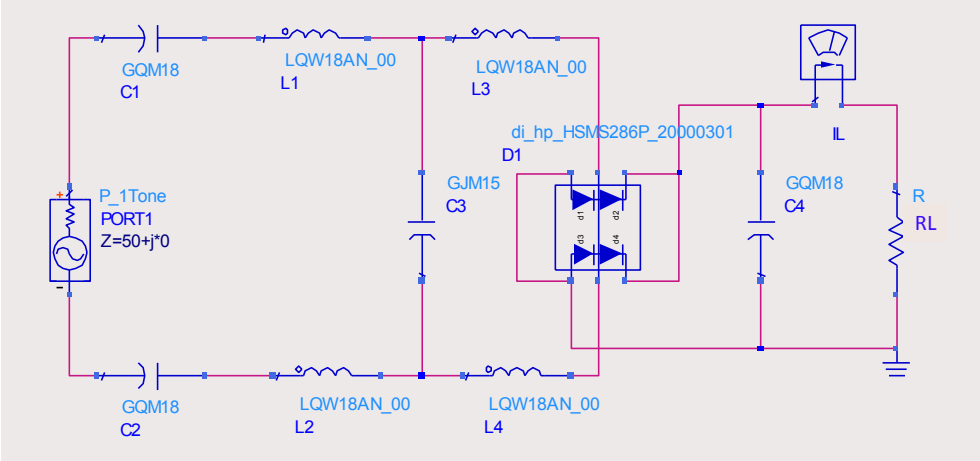

Figure 5.6: Full-wave rectifier schematic in ADS. C1=C2=C4=100 pF, L1=L2=2.4 nH, C3=0.3 pF, L3=L4=3.6 nH, RL=1 kΩ.

component values from the manufacturer's libraries in the large signal S-parameter solver of ADS. Input impedance of the optimized rectifier circuit is provided on the Smith Chart in Fig. 5.7 (a) and the input return loss is provided in Fig. 5.7 (b). Power dependence of the input impedance is also provided in Fig. 5.7 (a) and (b) with 5 dB steps. The rectifier has an excellent match to 50 Ω at the desired frequency of operation with -30 dB return loss at 15 dBm input power.

Fig. 5.8 provides additional simulation results on the rectifier characteristics. Fig. 5.8 (a) shows the rectifier's conversion efficiency for various input power levels with respect to frequency. Here, the rectifier conversion efficiency or the rectification efficiency is represented by:

$$\eta_{ac-dc} = \frac{P_{dc}}{P_{ac}}, \tag{5.2}$$

where P_{dc} is the power at the rectifier load resistor (RL) and P_{ac} is the input power at the rectifier input terminals. At 15 dBm, the rectification efficiency reaches 84%. Fig. 5.8

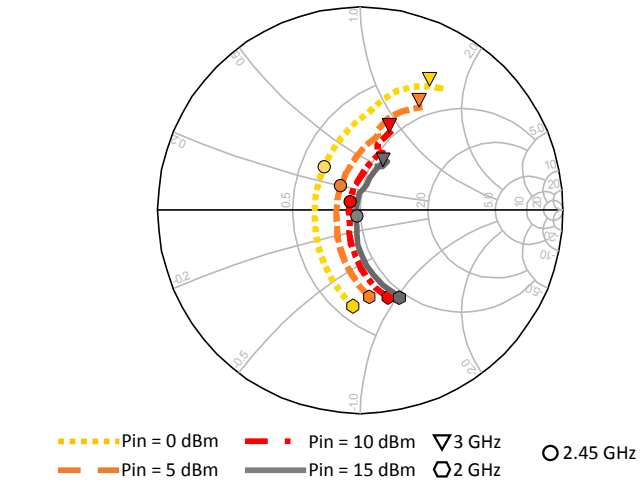

(a)

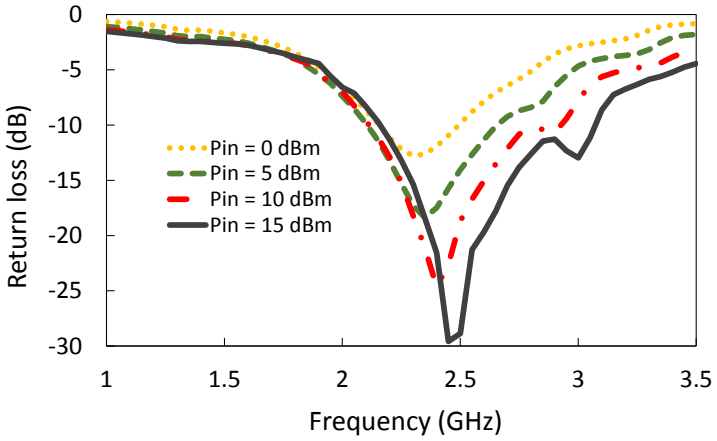

(b)

Figure 5.7: Input impedance of the full-wave rectifier is matched to 50 Ω; (a) complex input impedance is plotted on the Smith chart at various power levels (b) magnitude of the input return loss is plotted against frequency at various power levels.

(b) shows the rectifier's conversion efficiency against the input power with various resistive loads.

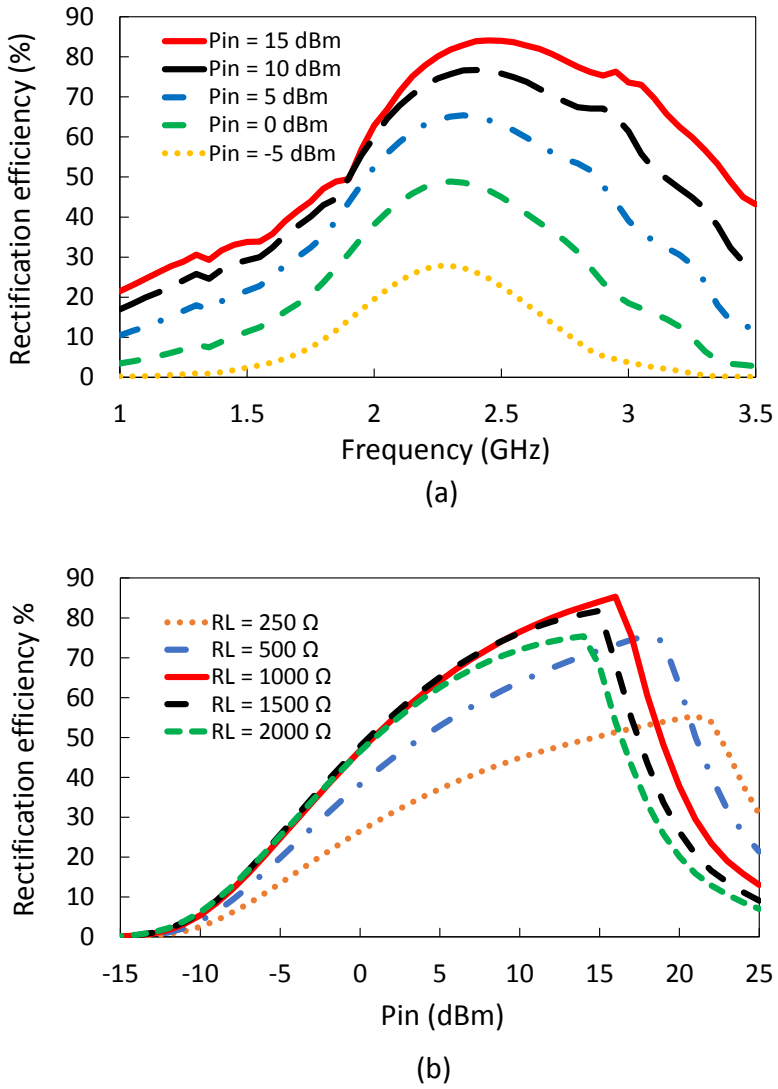

Figure 5.8: (a) Rectification efficiency vs. frequency at various input power levels. (b) Rectification efficiency vs. input power at various load resistance values.

Fig. 5.7 and Fig. 5.8 clearly demonstrate the rectifier is well matched at 2.45 GHz and optimized for 1 kΩ load. Efficiency of the rectifier is more than 50% for a wide input power range from 0 dBm to 17 dBm. The peak efficiency of 84% is achieved at the 15 dBm input.

5.4 Results and Discussion

The proposed dual-polarized energy harvesting surface was fabricated using Rogers RO4003C substrates as shown in Fig. 5.9. Each substrate had a thickness of 1.524 mm and the copper cladding was 35 μm. The size of the fabrication area was 228.6 mm x 304.8 mm (9 in x 12 in), which was enough to print 12 unit cells in a 3 x 4 layout. Fig. 5.9 (a) shows the top view of the fabricated prototype where black and red dashed lines indicate the super cells used for measurements. As shown in Fig. 5.9 (b), the overall structure consists of two substrates stacked on top of each other and a ground plane placed 5 mm away. The gap was maintained by nylon spacers with negligible permittivity. The channelling traces were printed at the back of each substrate and they were connected to the absorber surface using vias. The full-wave rectifier layout was printed at the end of the channelling traces as shown in the inset of Fig. 5.9 (b). As a result, a prototype panel was fabricated with a super cell of 4 unit cells for one polarization and a super cell of 3 unit cells for the other polarization, both integrated with their own rectifiers forming two complete rectenna systems dedicated to orthogonal polarizations. It should be noted that this proof of concept was built by using separate substrates and only double sided printing; however, the structure can be easily optimized for compact, multi-layer PCB fabrication.

Mutual coupling between the elements of a periodic structure can have a significant effect on the unit cell characteristics [27, 79, 113]. The full extent of these effects can only be measured in an infinite surface, but in practical terms, the majority of the coupling is caused by the adjacent cells. Therefore, even a finite size implementation can give a good approximation of the unit cell performance when the layout is carefully chosen [80, 81]. For this proof of concept, a standard Rogers board was populated with as many unit cells as possible and took the measurements from the central elements as indicated by the dashed

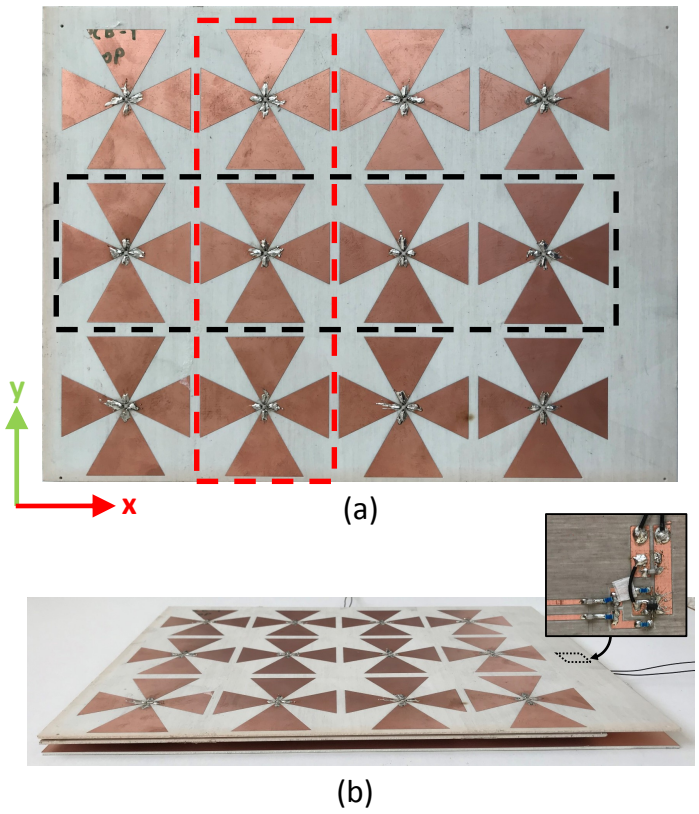

Figure 5.9: Fabricated rectenna panel on RO4003C substrates (a) top view where black and red dashed lines indicate the rows used for measurements (b) side view demonstrating the low profile of the stacked structure. Inset: Full-wave rectifier connected to the channelling traces.

rectangles. The super cells were composed of multiple unit cells in a longitudinal row configuration and the adjacent rows were printed on the board. Therefore, the measurements reflect the mutual coupling effects reasonably well, resulting in a good approximation for the unit cell performance when present in an infinite surface. Overall rectenna performance was evaluated using the radiation-to-dc conversion efficiency defined as:

$$\eta_{Rad-dc} = \frac{P_{dc}}{P_{Rad}} \tag{5.3}$$

where P_{dc} is the power at the load resistor and P_{Rad} is the total incident radiated power available at the physical area of the rectenna, which is enclosed by the dashed lines in Fig.5.9 (a) [27,113]. η_{Rad-dc} takes into account the absorption efficiency of the surface, the matching efficiency between the absorber and the rectifier, and the rectification efficiency of the rectifier (as provided in Section 5.3 and 5.2) [113]. The rectenna performance is further verified experimentally by using the measurement setup depicted in Fig. 5.10 (a). The fabricated energy harvesting surface was placed 1 m away from the horn antenna and illuminated by the linearly polarized plane waves generated by the horn antenna. Fig. 5.10 (b) shows the orientation of the energy harvesting surface with respect to the horn antenna, as well as its counterclockwise rotation direction in x-y plane to measure the rectenna performance under various polarization angles.

Efficiency measurements and calculations were provided in Chapter 3 and Chapter 4; same procedure was followed in this section [27,79,113]. Fig. 5.11 shows the measurement results of the dual-polarized energy harvesting surface. The radiation-to-dc conversion efficiency of the rectenna with 3 unit cells is provided in Fig. 5.11 (a). When the E-field vector is aligned with the x-axis (Θ=0°), the bow-tie structures along the x-axis absorbs the energy and the channelling traces connected to them along the y-axis transfers the absorbed energy to the rectifier at the end. When the available power density on the absorber surface was 0.313 mW/cm^2, the measured voltage at the 1k Ω rectifier load was 5.32 V; resulting in a radiation-to-dc conversion efficiency of 61% (the physical area of the super cell was 148.74 cm^2). At Θ=30°, 45° and 60°, the radiation-to-dc conversion efficiency was 44%, 32% and 18%, respectively. Similarly, Fig. 5.11 (b) shows the measured results for the super cell of four unit cells. When the E-field vector was aligned with the y-axis (Θ=90°), the radiation-to-dc conversion efficiency of the super cell was highest at 60%. At Θ=60°, 45° and 30°, the conversion efficiency decreased to 45%, 31% and 17%, respectively. The proposed energy harvesting surface is constructed with concentric bow-tie dipoles which are inherently linearly polarized structures. Hence, it is expected to have

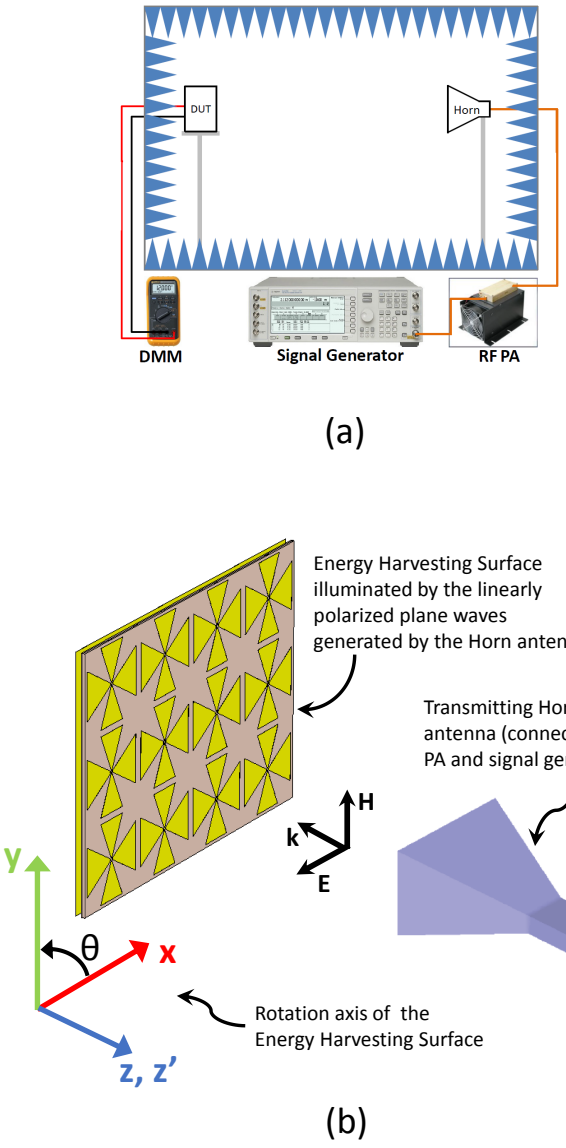

Figure 5.10: (a) Schematic diagram showing the measurement setup. (b) Illustration of the proposed energy harvesting surface illuminated by a linearly polarized horn antenna.

highest efficiencies when the E-field vector is parallel to the x or y axes. However, the measurement results further demonstrate that the proposed structure performs reasonably well when it is subject to plane waves of various polarization angles. The resistive loads of the super cells in the rows and columns can be further combined into a common load resulting in a polarization insensitive energy harvesting system.

5.5 Conclusion

A dual-polarized energy harvesting surface was presented with excellent absorption characteristics and built-in channelling traces to efficiently transfer the collected energy from multiple unit cells into a matched full-wave rectifier. Simulation results are provided for the absorber surface as well as the full-wave rectifier. The unit cell of the periodic surface consists of a *cross* structure formed by two concentric bow-tie dipoles that are 90° apart. A proof of concept rectenna panel was fabricated and tested for experimental verification of the simulations; the proposed energy harvesting surface achieves 61% and 60% radiation-to-dc conversion efficiencies when the normally incident plane wave has an E-field vector that aligns with the bow-tie directions. The performance of the structure is further evaluated in various polarization angles and the results indicate that the absorption from the rows and the columns of the periodic surface can be combined to create a scalable and polarization insensitive energy harvesting system.

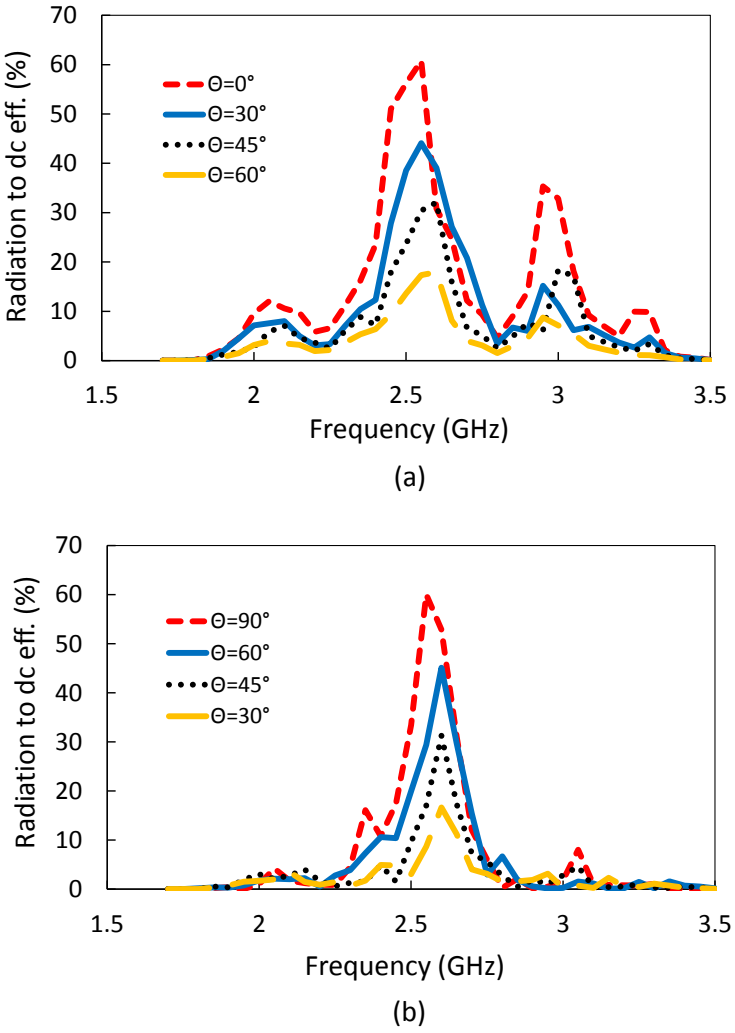

Figure 5.11: Measured radiation-to-dc conversion efficiency of the dual-polarized energy harvesting surface (a) efficiency measured on the row of 3 unit cells when the incident E-field is applied at various angles (Θ=0° implies E-field is parallel to x-axis) (b) efficiency measured on the row of 4 unit cells when incident E-field is applied at various angles (Θ=90° implies E-field is parallel to y-axis).

Chapter 6

Conclusions, Contributions and Future Work

6.1 Conclusions

This thesis presented several new concepts to improve rectenna efficiency in low power density environments. First, a balanced full-wave rectifier topology was introduced where the rectifier was differentially fed by two separate antennas. This configuration allowed the received power to be rectified and transferred into a load between two antennas. A proof of concept rectenna array was demonstrated at 2.45 GHz by using T-matched dipole antennas. Measurements showed that the proposed full-wave rectenna array achieved 74% radiation-to-dc conversion efficiency which was higher than the traditional half-wave rectennas implemented in the same physical footprint. In addition to its high efficiency, the proposed concept also allowed the rectified dc current to flow from one antenna to another through a resistive load. This feature was utilized to channel the rectified dc power to a single load. Second, an FSS absorber was developed as a special EM collector for low power density environments. This absorber was demonstrated to accept 98.5% of the available power on its surface and collect 97% of it exclusively on its resistive load (only 1.5% was dissipated as dielectric and metallic losses). A proof of concept prototype was fabricated

with a matched full-wave rectifier and the measurement results showed that the overall radiation-to-dc conversion efficiency of the complete rectenna system was 61%, which was considerably higher than the previously reported FSS based rectennas.

The energy harvesting surface was further expanded by adding dual-band and dual-polarization capabilities. Design details and simulation results were provided together with measurement results of the fabricated prototypes. Measurements demonstrated the feasibility of dual-band and polarization insensitive energy harvesting systems at low power density environments.

A key contribution of this thesis was the introduction of the scalability concept. The periodic absorber surfaces presented in this thesis had built-in channelling features to combine the collected power from multiple unit cells. It was shown, through prototype measurements, that it is feasible to utilize larger EM collectors per rectifier by effortlessly scaling the surface area while efficiently channelling the collected power. As a result, the number of diodes and diode losses were minimized in the system, leading to higher overall rectenna efficiencies. The work in this thesis showed that larger EM collectors can significantly mitigate the limitations posed by low ambient power densities. When integrated with a multi-cell configuration, an ordinary rectifier made with Schottky diodes was efficiently used at a power density that is less than $1/12^{th}$ of that would be required if it were to be used with a traditional single unit cell approach.

6.2 Contributions

6.2.1 Peer-reviewed Journal Publications

1. **F. Erkmen**, T. S. Almoneef and O. M. Ramahi, "Scalable Electromagnetic Energy Harvesting Using Frequency-Selective Surfaces," in IEEE Transactions on Microwave Theory and Techniques, vol. 66, no. 5, pp. 2433–2441, May 2018 **(Featured in IEEE Microwave Newsletter, 21 March 2018 [only five papers were featured in the newsletter])**.

2. **F. Erkmen**, T. S. Almoneef and O. M. Ramahi, "Electromagnetic Energy Harvesting Using Full-Wave Rectification," in IEEE Transactions on Microwave Theory and Techniques, vol. 65, no. 5, pp. 1843–1851, May 2017 **(Invited paper)**.

3. T. S. Almoneef, **F. Erkmen**, M. A. Alotaibi and O. M. Ramahi, "A New Approach to Microwave Rectennas Using Tightly Coupled Antennas," in IEEE Transactions on Antennas and Propagation, vol. 66, no. 4, pp. 1714–1724, April 2018.

4. T. S. Almoneef, **F. Erkmen** and O. M. Ramahi, "Harvesting the Energy of Multi-polarized Electromagnetic Waves." in Scientific Reports, vol. 7, no. 1, pp. 14656, November 2017.

5. **F. Erkmen** and O. M. Ramahi, "A Scalable, Dual-band Absorber Surface for Electromagnetic Energy Harvesting and Wireless Power Transfer," in IEEE Transactions on Microwave Theory and Techniques, May 2019 (Under review).

6. **F. Erkmen** and O. M. Ramahi, "A Scalable, Dual-polarized Absorber Surface for Electromagnetic Energy Harvesting and Wireless Power Transfer," in IEEE Transactions on Microwave Theory and Techniques, September 2019 (Under review).

Publications Produced During M.Sc. Thesis

7. **F. Erkmen**, C. Chen and J. L. Volakis, "Impedance Matched Ferrite Layers as Ground Plane Treatments to Improve Antenna Wide-Band Performance," in IEEE Transactions on Antennas and Propagation, vol. 57, no. 1, pp. 263–266, January 2009.

8. **F. Erkmen**, C. Chen and J. L. Volakis, "UWB magneto-dielectric ground plane for low-profile antenna applications," in IEEE Antennas and Propagation Magazine, vol. 50, no. 4, pp. 211–216, August 2008.

6.2.2 Peer-reviewed Conference Publications

1. **F. Erkmen** and O. M. Ramahi, "A Dual-band Electromagnetic Energy Harvesting Surface," 2019 IEEE International Symposium on Antennas and Propagation & USNC/URSI National Radio Science Meeting, Atlanta, GA, July 7–12, 2019.

2. **F. Erkmen**, T. S. Almoneef and O. M. Ramahi, "Electromagnetic Energy Harvesting Using Frequency Selective Surfaces," 2018 IEEE International Symposium on Antennas and Propagation & USNC/URSI National Radio Science Meeting, Boston, MA, July 8–13, 2018 (Accepted).

3. **F. Erkmen**, T. S. Almoneef and O. M. Ramahi, "Balanced full-wave rectenna for electromagnetic energy harvesting," 2017 IEEE International Symposium on Antennas and Propagation & USNC/URSI National Radio Science Meeting, San Diego, CA, July 9–14, 2017, pp. 1081–1082.

4. T. S. Almoneef, **F. Erkmen**, M. A. A. Dhaeebi and O. M. Ramahi, "Dual polarized metasurface for microwave energy harvesting and wireless power transfer," 12th European Conference on Antennas and Propagation (EuCAP 2018), London, April 9–13, 2018, pp. 1–3.

5. T. S. Almoneef, **F. Erkmen** and O. M. Ramahi, "Tightly coupled antennas for low cost and highly efficient energy harvesters," 2017 IEEE International Symposium on Antennas and Propagation & USNC/URSI National Radio Science Meeting, San Diego, CA, July 9–14, 2017, pp. 2029-2030.

6. **F. Erkmen** and O. M. Ramahi, "A Dual-band Electromagnetic Energy Harvesting Surface," 2nd Indian Conference on Antennas & Propagation (InCAP2019), Ahmedabad, India, December 19–22, 2019 (Under review).

Publications / Presentations Produced During M.Sc. Thesis

7. **F. Erkmen**, Chi-Chih Chen and J. L. Volakis, "UWB low profile antennas using ferrite loaded GP," 2008 IEEE Antennas and Propagation Society International Symposium, San Diego, CA, July 5–11 2008, pp. 1–4.

8. **F. Erkmen**, Chi-Chih Chen and J. L. Volakis, "Low Profile Magneto-Dielectric Ground Plane for UWB Antennas," Applied Computational Electromagnetics Society, Niagara Falls, Canada, March 30 - April 4 2008.

9. **F. Erkmen**, Chi-Chih Chen and J. L. Volakis, "UWB Magneto-Dielectric Ground Plane for Low-Profile Antenna Applications," Antenna Measurement Techniques Association (AMTA), St. Lois, MO, November 4–9, 2008 **(Best paper award)**.

10. **F. Erkmen**, Chi-Chih Chen and J. L. Volakis, "Wide-band Conformal Antenna Design Using Ferrite Loaded Ground Planes," North American Radio Science Meeting (URSI), Ottawa, Canada, July 22–26, 2007.

6.2.3 Non Peer-reviewed Publications

1. O. M. Ramahi and **F. Erkmen** "Producing Energy Out of Thin Air: Harvesting Electromagnetic Energy," Waterloo Institute for Sustainable Energy (WISE), April 2018 **(Featured in Research Spotlight, Waterloo Institute for Sustainable Energy (WISE))**.

6.3 Future Work

The natural extension of this thesis can be grouped into two categories: commercializing the developed energy harvesting surface for microwave applications and extending the concept to THz frequencies in order to harvest the infrared radiation.

6.3.1 Commercialization for Microwave Applications

The following activities are planned and some of them are in progress:

1. Develop a lower profile energy harvesting surface implemented on a printed circuit board (PCB) by using state of the art substrates that have higher dielectric constants and lower losses. Eliminate the air gap by using multi-layer PCBs. Fabricate a large prototype panel (at least 1 m x 1 m) and test under real life scenarios such as harvesting indoor Wi-Fi signals.

2. Extend the operational range by incorporating rectifiers that are efficient at lower input power levels.

3. Investigate the feasibility of using a flexible substrates for body-worn applications.

4. Investigate the feasibility of using optically transparent substrates (such as glass) for indoor / outdoor applications.

6.3.2 Extension to Infrared Applications

The following activities are planned and some of them are in progress:

1. There is abundant Infrared energy due to Earth's thermal emissions into outer space. Earth's surface temperature is around 300°K which results in a Blackbody radiation that has a dominant wavelength of 10μm. To harvest this energy, an absorber structure designed to operate at 30 THz would be needed. We can start by a simple frequency scaling of the unit cell dimensions and further optimize the model to account for the optical material properties in THz frequencies.

2. Considering the rectification mechanism relies on Metal-Insulator-Metal (MIM) tunnelling effects, the concept of large EM collector per rectifier is also very important for THz applications. Optimize the design to maintain superior channelling features in order to achieve high field intensity where the rectification occurs.

3. Fabricate infrared prototypes and experimentally verify the simulation results by monitoring the radiation-to-ac conversion efficiency (i.e. absorption efficiency).

4. Extend the infrared absorber surface to incorporate the rectification mechanism by implementing MIM tunnelling effects and measure the integrated rectenna for overall radiation-to-dc conversion efficiency.

Bibliography

[1] M. Cheney, *Tesla: man out of time*. Simon and Schuster, 2011.

[2] N. Tesla, "Apparatus for transmitting electrical energy." December 1914, U.S. Patent No: 1,119,732.

[3] H. Yagi and S. Uda, "On the feasibility of power transmission by electric waves," in *Proc. 3rd Pan-Pacific Sci. Congr*, Tokyo, Japan, October 30 – November 11 1926, pp. 1305–1313.

[4] "Electric light without current," *The Literary Digest*, vol. 112, no. 3, pp. 30–31, January 1932.

[5] W. C. Brown, "The history of power transmission by radio waves," *IEEE Transactions on Microwave Theory and Techniques*, vol. 32, no. 9, pp. 1230–1242, September 1984.

[6] B. Strassner and K. Chang, *Encyclopedia of RF and Microwave Engineering*. Wiley Online Library, 2005.

[7] R. B. Erb, "Power from space – The tough questions: The 1995 Peter E. Glaser Lecture," *Acta Astronautica*, vol. 38, no. 4, pp. 539–550, February 1996.

[8] W. C. Brown, "Electronic and mechanical improvement of the receiving terminal of a free-space microwave power transmission system," *NASA Technical Reports Server (NTRS)*, August 1977.

[9] W. C. Brown and J. F. Triner, "Experimental thin-film, etched-circuit rectenna," in *1982 IEEE MTT-S International Microwave Symposium Digest*, Dallas, TX, USA, June 15–17 1982, pp. 185–187.

[10] P. Koert, J. Cha, and M. Machina, "35 and 94 GHz rectifying antenna systems," in *SPS 91 - Power from Space*, Gif-sur-Yvette, France, August 27–30 1991, pp. 541–547.

[11] J. O. McSpadden, *Rectifying and oscillating integrated antennas*, 1999.

[12] S. S. Bharj, R. Camisa, S. Grober, F. Wozniak, and E. Pendleton, "High efficiency C-band 1000 element rectenna array for microwave powered applications," in *1992 IEEE MTT-S Microwave Symposium Digest*, June 1–5 1992, pp. 301–303 vol.1.

[13] W. C. Brown, "The amplitron, a super power microwave generator," *Electron Progress*, vol. 5, no. 1, pp. 1–5, July 1960.

[14] R. Vyas, H. Nishimoto, M. Tentzeris, Y. Kawahara, and T. Asami, "A battery-less, energy harvesting device for long range scavenging of wireless power from terrestrial TV broadcasts," in *2012 IEEE/MTT-S International Microwave Symposium Digest*, Montreal, QC, Canada, June 17–22 2012, pp. 1–3.

[15] M. Piuela, P. D. Mitcheson, and S. Lucyszyn, "Ambient RF energy harvesting in urban and semi-urban environments," *IEEE Transactions on Microwave Theory and Techniques*, vol. 61, no. 7, pp. 2715–2726, July 2013.

[16] M. Pinuela, D. C. Yates, P. D. Mitcheson, and S. Lucyszyn, "London RF survey for radiative ambient RF energy harvesters and efficient DC-load inductive power transfer," in *2013 7th European Conference on Antennas and Propagation (EuCAP)*, Gothenburg, Sweden, April 8–12 2013, pp. 2839–2843.

[17] S. Shang, S. Yang, J. Liu, M. Shan, and H. Cao, "Metamaterial electromagnetic energy harvester with high selective harvesting for left and right-handed circularly polarized waves," *Journal of Applied Physics*, vol. 120, no. 4, p. 045106, 2016.

[18] T. S. Almoneef and O. M. Ramahi, "Metamaterial electromagnetic energy harvester with near unity efficiency," *Applied Physics Letters*, vol. 106, no. 15, p. 153902, 2015.

[19] H. Takhedmit, L. Cirio, F. Costa, and O. Picon, "Transparent rectenna and rectenna array for RF energy harvesting at 2.45 GHz," in *The 8th European Conference on Antennas and Propagation (EuCAP 2014)*, Hague, Netherlands, April 6–11 2014, pp. 2970–2972.

[20] T. Oka, T. Ogata, K. Saito, and S. Tanaka, "Triple-band single-diode microwave rectifier using CRLH transmission line," in *2014 Asia-Pacific Microwave Conference*, Sendai, Japan, November 4–7 2014, pp. 1013–1015.

[21] S. D. Assimonis and A. Bletsas, "Energy harvesting with a low-cost and high efficiency rectenna for low-power input," in *2014 IEEE Radio and Wireless Symposium (RWS)*, Newport Beach, CA, USA, January 19–23 2014, pp. 229–231.

[22] U. Olgun, C. Chen, and J. L. Volakis, "Wireless power harvesting with planar rectennas for 2.45 GHz RFIDs," in *2010 URSI International Symposium on Electromagnetic Theory*, Berlin, Germany, August 16–19 2010, pp. 329–331.

[23] J. Heikkinen and M. Kivikoski, "Low-profile circularly polarized rectifying antenna for wireless power transmission at 5.8 GHz," *IEEE Microwave and Wireless Components Letters*, vol. 14, no. 4, pp. 162–164, April 2004.

[24] J. Heikkinen and M.Kivikoski, "A novel dual-frequency circularly polarized rectenna," *IEEE Antennas and Wireless Propagation Letters*, vol. 2, no. 1, pp. 330–333, October 2003.

[25] J. S. Sun, R. H. Chen, S. K. Liu, and C. F. Yang, "Wireless power transmission with circularly polarized rectenna," *Microwave Journal*, vol. 2, pp. 1–15, January 2011.

[26] V. Marian, B. Allard, C. Vollaire, and J. Verdier, "Strategy for microwave energy harvesting from ambient field or a feeding source," *IEEE Transactions on Power Electronics*, vol. 27, no. 11, pp. 4481–4491, November 2012.

[27] F. Erkmen, T. S. Almoneef, and O. M. Ramahi, "Electromagnetic energy harvesting using full-wave rectification," *IEEE Transactions on Microwave Theory and Techniques*, vol. 65, no. 5, pp. 1843–1851, May 2017.

[28] B. Merabet, F. Costa, H. Takhedmit, C. Vollaire, B. Allard, L. Cirio, and O. Picon, "A 2.45-ghz localized elements rectenna," in *2009 3rd IEEE International Symposium on Microwave, Antenna, Propagation and EMC Technologies for Wireless Communications*, Beijing, China, October 27–29 2009, pp. 419–422.

[29] M. K. Hosain, A. Z. Kouzani, M. F. Samad, and S. J. Tye, "A miniature energy harvesting rectenna for operating a head-mountable deep brain stimulation device," *IEEE Access*, vol. 3, pp. 223–234, April 2015.

[30] M. Ito, K. Hosodani, K. Itoh, S. i. Betsudan, S. Makino, T. Hirota, K. Noguchi, and E. Taniguchi, "High efficient bridge rectifiers in 100MHz and 2.4GHz bands," in *Wireless Power Transfer Conference (WPTC), 2014 IEEE*, Jeju City, Korea (South), May 8–9 2014, pp. 64–67.

[31] K. Itoh, "RF bridge rectifier and its good possibility for wireless power transmission systems," in *2015 IEEE International Symposium on Radio-Frequency Integration Technology (RFIT)*, Sendai, Japan, August 26–28 2015, pp. 226–228.

[32] Y.-J. Ren and K. Chang, "5.8-GHz circularly polarized dual-diode rectenna and rectenna array for microwave power transmission," *IEEE Transactions on Microwave Theory and Techniques*, vol. 54, no. 4, pp. 1495–1502, June 2006.

[33] T. Sakamoto, Y. Ushijima, E. Nishiyama, M. Aikawa, and I. Toyoda, "5.8-GHz series/parallel connected rectenna array using expandable differential rectenna units," *IEEE Transactions on Antennas and Propagation*, vol. 61, no. 9, pp. 4872–4875, September 2013.

[34] A. Mavaddat, S. H. M. Armaki, and A. R. Erfanian, "Millimeter-wave energy harvesting using 4x4 microstrip patch antenna array," *IEEE Antennas and Wireless Propagation Letters*, vol. 14, pp. 515–518, February 2015.

[35] Y. J. Ren and K. Chang, "Bow-tie retrodirective rectenna," *Electronics Letters*, vol. 42, no. 4, pp. 191–192, February 2006.

[36] J. A. Hagerty, F. B. Helmbrecht, W. H. McCalpin, R. Zane, and Z. B. Popovic, "Recycling ambient microwave energy with broad-band rectenna arrays," *IEEE Transactions on Microwave Theory and Techniques*, vol. 52, no. 3, pp. 1014–1024, March 2004.

[37] T. S. Almoneef and O. M. Ramahi, "Can split-ring resonators be viable for electromagnetic energy harvesting?" in *2014 IEEE Antennas and Propagation Society International Symposium (APSURSI)*, Memphis, TN, USA, July 6–11 2014, pp. 424–425.

[38] J. O. McSpadden, L. Fan, and K. Chang, "Design and experiments of a high-conversion-efficiency 5.8-GHz rectenna," *IEEE Transactions on Microwave Theory and Techniques*, vol. 46, no. 12, pp. 2053–2060, December 1998.

[39] T. C. Yo, C. M. Lee, C. M. Hsu, and C. H. Luo, "Compact circularly polarized rectenna with unbalanced circular slots," *IEEE Transactions on Antennas and Propagation*, vol. 56, no. 3, pp. 882–886, March 2008.

[40] Z. Liu, Z. Zhong, and Y. X. Guo, "Enhanced dual-band ambient RF energy harvesting with ultra-wide power range," *IEEE Microwave and Wireless Components Letters*, vol. 25, no. 9, pp. 630–632, September 2015.

[41] M. Mrnka, Z. Raida, and J. Grosinger, "Wide-band dielectric resonator antennas for RF energy harvesting," in *2015 Conference on Microwave Techniques (COMITE)*, Pardubice, Czech Republic, April 22–23 2015, pp. 1–4.

[42] R. Maher, E. Tammam, A. I. Galal, and H. F. Hamed, "Design of a broadband planar antenna for RF energy harvesting," in *2016 International Conference on Electrical, Electronics, and Optimization Techniques (ICEEOT)*, Chennai, India, March 3–5 2016, pp. 1808–1810.

[43] T. Matsunaga, E. Nishiyama, and I. Toyoda, "5.8-GHz stacked differential rectenna suitable for large-scale rectenna arrays with DC connection," *IEEE Transactions on Antennas and Propagation*, vol. 63, no. 12, pp. 5944–5949, December 2015.

[44] J. Ye, C. Yang, and Y. Zhang, "Design and experiment of a rectenna array base on GaAs transistor for microwave power transmission," in *2016 IEEE International Conference on Microwave and Millimeter Wave Technology (ICMMT)*, vol. 1, Beijing, China, June 5–8 2016, pp. 323–326.

[45] U. Olgun, C. C. Chen, and J. L. Volakis, "Investigation of rectenna array configurations for enhanced RF power harvesting," *IEEE Antennas and Wireless Propagation Letters*, vol. 10, pp. 262–265, April 2011.

[46] D. R. Smith, W. J. Padilla, D. Vier, S. C. Nemat-Nasser, and S. Schultz, "Composite medium with simultaneously negative permeability and permittivity," *Physical Review Letters*, vol. 84, no. 18, p. 4184, 2000.

[47] N. I. Landy, S. Sajuyigbe, J. J. Mock, D. R. Smith, and W. J. Padilla, "Perfect metamaterial absorber," *Physical Review Letters*, vol. 100, no. 20, p. 207402, 2008.

[48] O. M. Ramahi, T. S. Almoneef, M. AlShareef, and M. S. Boybay, "Metamaterial particles for electromagnetic energy harvesting," *Applied Physics Letters*, vol. 101, no. 17, p. 173903, 2012.

[49] X. Shen, T. J. Cui, J. Zhao, H. F. Ma, W. X. Jiang, and H. Li, "Polarization-independent wide-angle triple-band metamaterial absorber," *Optics express*, vol. 19, no. 10, pp. 9401–9407, 2011.

[50] K. Aydin, V. E. Ferry, R. M. Briggs, and H. A. Atwater, "Broadband polarization-independent resonant light absorption using ultrathin plasmonic super absorbers," *Nature Communications*, vol. 2, p. 517, 2011.

[51] J. Hao, É. Lheurette, L. Burgnies, É. Okada, and D. Lippens, "Bandwidth enhancement in disordered metamaterial absorbers," *Applied Physics Letters*, vol. 105, no. 8, p. 081102, 2014.

[52] F. Ding, Y. Cui, X. Ge, Y. Jin, and S. He, "Ultra-broadband microwave metamaterial absorber," *Applied Physics Letters*, vol. 100, no. 10, p. 103506, 2012.

[53] S. Bhattacharyya and K. Vaibhav Srivastava, "Triple band polarization-independent ultra-thin metamaterial absorber using electric field-driven LC resonator," *Journal of Applied Physics*, vol. 115, no. 6, p. 064508, 2014.

[54] S. Zhong and S. He, "Ultrathin and lightweight microwave absorbers made of mu-near-zero metamaterials," *Scientific Reports*, vol. 3, p. 2083, 2013.

[55] W. Xu and S. Sonkusale, "Microwave diode switchable metamaterial reflector/absorber," *Applied Physics Letters*, vol. 103, no. 3, p. 031902, 2013.

[56] S. Ghosh, S. Bhattacharyya, and K. V. Srivastava, "Design, characterisation and fabrication of a broadband polarisation-insensitive multi-layer circuit analogue absorber," *IET Microwaves, Antennas & Propagation*, vol. 10, no. 8, pp. 850–855, 2016.

[57] Y. Han, W. Che, C. Christopoulos, Y. Xiong, and Y. Chang, "A fast and efficient design method for circuit analog absorbers consisting of resistive square-loop arrays," *IEEE Transactions on Electromagnetic Compatibility*, vol. 58, no. 3, pp. 747–757, June 2016.

[58] D. Kundu, A. Mohan, and A. Chakrabarty, "Single-layer wideband microwave absorber using array of crossed dipoles," *IEEE Antennas and Wireless Propagation Letters*, vol. 15, pp. 1589–1592, 2016.

[59] Y. Zhi Cheng, Y. Wang, Y. Nie, R. Zhou Gong, X. Xiong, and X. Wang, "Design, fabrication and measurement of a broadband polarization-insensitive metamaterial absorber based on lumped elements," *Journal of Applied Physics*, vol. 111, no. 4, p. 044902, 2012.

[60] S. Li, J. Gao, X. Cao, W. Li, Z. Zhang, and D. Zhang, "Wideband, thin, and polarization-insensitive perfect absorber based the double octagonal rings metamaterials and lumped resistances," *Journal of Applied Physics*, vol. 116, no. 4, p. 043710, 2014.

[61] Z. Popovi, S. Korhummel, S. Dunbar, R. Scheeler, A. Dolgov, R. Zane, E. Falkenstein, and J. Hagerty, "Scalable RF energy harvesting," *IEEE Transactions on Microwave Theory and Techniques*, vol. 62, no. 4, pp. 1046–1056, April 2014.

[62] C. H. P. Lorenz, S. Hemour, and K. Wu, "Physical mechanism and theoretical foundation of ambient RF power harvesting using zero-bias diodes," *IEEE Transactions on Microwave Theory and Techniques*, vol. 64, no. 7, pp. 2146–2158, July 2016.

[63] S. Keyrouz, G. Perotto, and H. J. Visser, "Frequency selective surface for radio frequency energy harvesting applications," *IET Microwaves, Antennas Propagation*, vol. 8, no. 7, pp. 523–531, May 2014.

[64] D. Ferreira, L. Sismeiro, A. Ferreira, R. F. S. Caldeirinha, T. R. Fernandes, and I. Cuias, "Hybrid FSS and rectenna design for wireless power harvesting," *IEEE Transactions on Antennas and Propagation*, vol. 64, no. 5, pp. 2038–2042, May 2016.

[65] AvagoTech., "Avago HSMS-286x Datasheet," *http://www.avagotech.com*.

[66] Murata, "Murata LQW18AN72NG00D Datasheet," *http://www.murata.com*.

[67] T. S. Almoneef, H. Sun, and O. M. Ramahi, "A 3-D folded dipole antenna array for far-field electromagnetic energy transfer," *IEEE Antennas and Wireless Propagation Letters*, vol. 15, pp. 1406–1409, April 2016.

[68] J. Choo, J. Ryoo, J. Hong, H. Jeon, C. Choi, and M. M. Tentzeris, "T-matching networks for the efficient matching of practical RFID tags," in *2009 European Microwave Conference (EuMC)*, Rome, Italy, September 29 – October 01 2009, pp. 5–8.

[69] K. R. Demarest and D. D. Deavours, "Limitations of the Uda model for T-match antennas," *Progress In Electromagnetics Research*, vol. 113, pp. 1–15, January 2011.

[70] T. S. Northup, "Designing a planar T-match antenna to have a 2^{nd} order Chebyshev band-pass filter frequency response for the purpose of UHF RFID," Ph.D. dissertation, University of Kansas, September 8 2011.

[71] www.cst.com, "CST Studio Suite," *CST Computer Simulation Technology AG*.

[72] T. Koskinen, H. Rajagopalan, and Y. Rahmat-Samii, "Impedance measurements of various types of balanced antennas with the differential probe method," in *2009 IEEE International Workshop on Antenna Technology*, Santa Monica, CA, USA, March 2–4 2009, pp. 1–4.

[73] R. Meys and F. Janssens, "Measuring the impedance of balanced antennas by an S-parameter method," *IEEE Antennas and Propagation Magazine*, vol. 40, no. 6, pp. 62–65, December 1998.

[74] C. A. Balanis, *Antenna theory: analysis and design*. John Wiley & Sons, 2012.

[75] K. D. Palmer and M. W. van Rooyen, "Simple broadband measurements of balanced loads using a network analyzer," *IEEE Transactions on Instrumentation and Measurement*, vol. 55, no. 1, pp. 266–272, February 2006.

[76] J. Grosinger, C. Mecklenbrauker, and A. L. Scholtz, "UHF RFID transponder chip and antenna impedance measurements," in *Proc. Third Inter. EURASIP Workshop RFID Technol*, Cartagena, Spain, September 6–7 2010, pp. 43–46.

[77] J. Grosinger, L. W. Mayer, C. F. Mecklenbrauker, and A. L. Scholtz, "Input impedance measurement of a dipole antenna mounted on a car tire," in *Proc. International Symposium on Antennas and Propagation*, Bangkok, Thailand, October 20–23 2009, pp. 1175–1178.

[78] "Hirose w.fl datasheet," *https://www.hirose.co.jp*.

[79] O. M. Ramahi, T. S. Almoneef, M. Alshareef, and M. S. Boybay, "Metamaterial particles for electromagnetic energy harvesting," *Applied Physics Letters*, vol. 101, no. 17, pp. 173 903–173 903, October 2012.

[80] H. Kamoda, M. Hanazawa, S. Kitazawa, H. Ban, N. Kukutsu, and K. Kobayashi, "Design of rectenna array panel taking into account mutual coupling for RF energy

harvesting," in *2014 IEEE Radio and Wireless Symposium (RWS)*, Newport Beach, CA, USA, January 19–23 2014, pp. 61–63.

[81] H. Kamoda, M. Hanazawa, S. Kitazawa, H. Ban, and K. Kobayashi, "Mutual coupling effect on rectenna array for RF energy harvesting," in *2013 European Microwave Conference*, Nuremberg, Germany, October 6–10 2013, pp. 503–506.

[82] Y. Q. Wang and X. X. Yang, "Design of a high-efficiency circularly polarized rectenna for 35 GHz microwave power transmission system," in *2012 Asia-Pacific Power and Energy Engineering Conference*, Shanghai, China, March 27–29 2012, pp. 1–4.

[83] H. Sun and W. Geyi, "A new rectenna with all-polarization-receiving capability for wireless power transmission," *IEEE Antennas and Wireless Propagation Letters*, vol. 15, pp. 814–817, 2016.

[84] M. E. Badawe and O. M. Ramahi, "Metasurface for near-unity electromagnetic energy harvesting and wireless power transfer," in *2016 IEEE International Symposium on Antennas and Propagation (APSURSI)*, Fajardo, Puerto Rico, June 26 – July 1 2016, pp. 609–610.

[85] T. Matsunaga, E. Nishiyama, and I. Toyoda, "5.8-GHz stacked differential rectenna suitable for large-scale rectenna arrays with dc connection," *IEEE Transactions on Antennas and Propagation*, vol. 63, no. 12, pp. 5944–5949, December 2015.

[86] D. Kundu, A. Mohan, and A. Chakrabarty, "Thickness reduction of single layer circuit analog absorber," in *2015 IEEE Applied Electromagnetics Conference (AEMC)*, Guwahati, India, December 18–21 2015, pp. 1–2.

[87] S. Ghosh, S. Bhattacharyya, D. Chaurasiya, and K. V. Srivastava, "A broadband polarization-insensitive circuit analog absorber using lumped resistors," in *2015 IEEE Applied Electromagnetics Conference (AEMC)*, Guwahati, India, December 18–21 2015, pp. 1–2.

[88] W. Salisbury, "Absorbent body for electromagnetic waves," June 1952, U.S. Patent No: 2,599,944.

[89] B. A. Munk, *Frequency selective surfaces: theory and design*. John Wiley & Sons, 2005.

[90] F. Erkmen, C. Chen, and J. L. Volakis, "Impedance matched ferrite layers as ground plane treatments to improve antenna wide-band performance," *IEEE Transactions on Antennas and Propagation*, vol. 57, no. 1, pp. 263–266, January 2009.

[91] F. Erkmen, C.Chen, and J. L. Volakis, "UWB magneto-dielectric ground plane for low-profile antenna applications," *IEEE Antennas and Propagation Magazine*, vol. 50, no. 4, pp. 211–216, August 2008.

[92] F. Erkmen, Chi-Chih Chen, and J. L. Volakis, "UWB low profile antennas using ferrite loaded gp," in *2008 IEEE Antennas and Propagation Society International Symposium*, San Diego, CA, USA, July 5–11 2008, pp. 1–4.

[93] Myung-Jun Park and Sung-Soo Kim, "Wide bandwidth pyramidal absorbers of granular ferrite and carbonyl iron powders," in *2000 IEEE International Magnetics Conference (INTERMAG)*, Toronto, ON, Canada, April 9–13 2000, pp. 457–457.

[94] I. Baek, S. Choi, H. Lee, W. Cho, V. Petrov, A. Agnesi, V. Pasiskevicius, D.-I. Yeom, K. Kim, B. Hong *et al.*, "Passive mode-locking of a ti: Sapphire laser using low-dimensional carbon nanostructures," in *Conference on Lasers and Electro-Optics/Pacific Rim*. Sydney, Australia: Optical Society of America, August 28 – September 1 2011, pp. 1154–1155.

[95] W. Choi, J. Shin, T. Song, J. Kim, C. Cho, W. Lee, and C. Kim, "Design of circuit-analog (CA) absorber and application to the leading edge of a wing-shaped structure," *IEEE Transactions on Electromagnetic Compatibility*, vol. 56, no. 3, pp. 599–607, June 2014.

[96] Q. Zhang and Z. Shen, "A dual-polarized switchable microwave absorber," in *Proceedings of the 2012 IEEE International Symposium on Antennas and Propagation*, Chicago, IL, USA, July 8–14 2012, pp. 1–2.

[97] W. Che, H. Ye, Y. Xiong, Y. Chang, and C. Christopoulos, "A fast and efficient method for design of circuit analog absorbers consisting of resistive square loop arrays," in *2015 IEEE International Conference on Computational Electromagnetics*, Hong Kong, Hong Kong SAR, February 2–5 2015, pp. 35–37.

[98] Y. Shang, S. Xiao, and Z. Shen, "A thin wideband circuit analog absorber using square-loop arrays," in *2013 IEEE Antennas and Propagation Society International Symposium (APSURSI)*, Lake Buena Vista, Florida, USA, July 7–12 2013, pp. 472–473.

[99] B. A. Munk, P. Munk, and J. Pryor, "On designing Jaumann and Circuit Analog Absorbers (CA Absorbers) for oblique angle of incidence," *IEEE Transactions on Antennas and Propagation*, vol. 55, no. 1, pp. 186–193, January 2007.

[100] N. Marcuvitz, *Waveguide Handbook*. IET, 1951.

[101] A. K. Rashid, Z. Shen, and R. Mittra, "On the optimum design of a single-layer thin wideband radar absorber," in *2011 IEEE International Symposium on Antennas and Propagation (APSURSI)*, Spokane, Washington, USA, July 3–8 2011, pp. 2916–2919.

[102] Y. Zhi Cheng, Y. Wang, Y. Nie, R. Zhou Gong, X. Xiong, and X. Wang, "Design, fabrication and measurement of a broadband polarization-insensitive metamaterial absorber based on lumped elements," *Journal of Applied Physics*, vol. 111, no. 4, p. 044902, 2012.

[103] S. Li, J. Gao, X. Cao, W. Li, Z. Zhang, and D. Zhang, "Wideband, thin, and polarization-insensitive perfect absorber based the double octagonal rings metamaterials and lumped resistances," *Journal of Applied Physics*, vol. 116, no. 4, p. 043710, 2014.

[104] M. Ettorre, W. A. Alomar, and A. Grbic, "Long slot van atta array for far-field wireless power transfer," in *2017 IEEE International Symposium on Antennas and Propagation USNC/URSI National Radio Science Meeting*, San Diego, California, USA, July 9–14 2017, pp. 1291–1293.

[105] P. D. H. Re, S. K. Podilchak, S. Rotenberg, G. Goussetis, and J. Lee, "Retrodirective antenna array for circularly polarized wireless power transmission," in *2017 11th European Conference on Antennas and Propagation (EUCAP)*, Paris, France, March 19–24 2017, pp. 891–895.

[106] M. Koohestani, M. Zhadobov, and M. Ettorre, "Design methodology of a printed WPT system for HF-band mid-range applications considering human safety regulations," *IEEE Transactions on Microwave Theory and Techniques*, vol. 65, no. 1, pp. 270–279, January 2017.

[107] A. P. Sohrab and Z. Atlasbaf, "A circuit analog absorber with optimum thickness and response in X-band," *IEEE Antennas and Wireless Propagation Letters*, vol. 12, pp. 276–279, 2013.

[108] Y.-q. Pang, Y.-j. Zhou, and J. Wang, "Equivalent circuit method analysis of the influence of frequency selective surface resistance on the frequency response of metamaterial absorbers," *Journal of Applied Physics*, vol. 110, no. 2, p. 023704, 2011.

[109] S. A. Rotenberg, P. D. H. Re, S. K. Podilchak, G. Goussetis, and J. Lee, "An efficient rectifier for an RDA wireless power transmission system operating at 2.4 GHz," in *2017 XXXIInd General Assembly and Scientific Symposium of the International Union of Radio Science (URSI GASS)*, Montreal, Canada, August 19–26 2017, pp. 1–3.

[110] M. El Badawe, T. S. Almoneef, and O. M. Ramahi, "A metasurface for conversion of electromagnetic radiation to DC," *AIP Adv.*, vol. 7, no. 3, p. 035112, 2017.

[111] A. Z. Ashoor and O. M. Ramahi, "Polarization-independent cross-dipole energy harvesting surface," *IEEE Transactions on Microwave Theory and Techniques*, vol. 67, no. 3, pp. 1130–1137, March 2019.

[112] A. Z. Ashoor, T. S. Almoneef, and O. M. Ramahi, "A planar dipole array surface for electromagnetic energy harvesting and wireless power transfer," *IEEE Transactions on Microwave Theory and Techniques*, vol. 66, no. 3, pp. 1553–1560, March 2018.

[113] F. Erkmen, T. S. Almoneef, and O. M. Ramahi, "Scalable electromagnetic energy harvesting using frequency-selective surfaces," *IEEE Transactions on Microwave Theory and Techniques*, vol. 66, no. 5, pp. 2433–2441, May 2018.

[114] F. Costa, A. Monorchio, and G. Manara, "Analysis and design of ultra thin electromagnetic absorbers comprising resistively loaded high impedance surfaces," *IEEE Transactions on Antennas and Propagation*, vol. 58, no. 5, pp. 1551–1558, May 2010.

[115] www.keysight.com, "Advanced Design System (ADS)," *Keysight Technologies*.

[116] C. R. Valenta and G. D. Durgin, "Harvesting wireless power: Survey of energy-harvester conversion efficiency in far-field, wireless power transfer systems," *IEEE Microwave Magazine*, vol. 15, no. 4, pp. 108–120, June 2014.